

University of Southampton Research Repository

Copyright © and Moral Rights for this thesis and, where applicable, any accompanying data are retained by the author and/or other copyright owners. A copy can be downloaded for personal non-commercial research or study, without prior permission or charge. This thesis and the accompanying data cannot be reproduced or quoted extensively from without first obtaining permission in writing from the copyright holder/s. The content of the thesis and accompanying research data (where applicable) must not be changed in any way or sold commercially in any format or medium without the formal permission of the copyright holder/s.

When referring to this thesis and any accompanying data, full bibliographic details must be given, e.g.

Thesis: Author (Year of Submission) "Full thesis title", University of Southampton, name of the University Faculty or School or Department, PhD Thesis, pagination.

Data: Author (Year) Title. URI [dataset]

UNIVERSITY OF SOUTHAMPTON

FACULTY OF ENGINEERING AND THE ENVIRONMENT

Engineering Sciences

**AN INVESTIGATION OF THE FACTORS ASSOCIATED WITH THE
X-RAY TUBE AND THEIR INFLUENCE ON DIMENSIONAL
MEASUREMENT IN MICRO-FOCUS CONE-BEAM INDUSTRIAL
X-RAY COMPUTED TOMOGRAPHY SYSTEMS**

by

Nadia Flay

Thesis for the degree of Doctor of Philosophy

July 2016

UNIVERSITY OF SOUTHAMPTON

ABSTRACT

FACULTY OF ENGINEERING AND THE ENVIRONMENT

Engineering Sciences

Thesis for the degree of Doctor of Philosophy

AN INVESTIGATION OF THE FACTORS ASSOCIATED WITH THE X-RAY TUBE AND THEIR INFLUENCE ON DIMENSIONAL MEASUREMENT IN MICRO-FOCUS CONE-BEAM INDUSTRIAL X-RAY COMPUTED TOMOGRAPHY SYSTEMS

Nadia Flay

In recent years, X-ray computed tomography (XCT) has successfully entered the field of dimensional metrology. XCT offers advantages over traditional tactile and optical coordinate measuring machines because of its ability to detect both the outer and inner geometries of an object. Due to the complex nature of XCT, there are a large number of factors which can influence dimensional measurement; many of these factors are still poorly understood.

The novel study of a number of influence factors associated with the X-ray tube and their influence on dimensional measurement in micro-focus cone-beam XCT systems is presented in this thesis. The influence factors investigated in this study are the positional stability of the focal spot, the off-focal radiation, the focal spot size and the focal spot shape. The necessary background information to X-ray physics, XCT technology and dimensional metrology is discussed. The analysis of these influence factors was conducted at the National Physical Laboratory using experimental and computer simulation techniques. The experimental part of this research was carried out on Nikon Metrology XT H 225 M, with simulations performed using bespoke computer codes.

The results of the study show that the positional stability of the focal spot, the off-focal radiation, the focal spot size and shape can all affect dimensional measurement. It is, therefore, proposed to include these parameters as part of the future standardised X-ray tube qualification and performance verification procedures of XCT systems. The evaluation techniques developed during the study can be employed as part of these standardised procedures. In addition, based on the findings of the study a number of future areas of research are proposed.

Table of Contents

| | |
|---|-------------|
| Table of Contents | i |
| List of Tables | v |
| List of Figures | vii |
| List of Publications | xi |
| Papers in Preparation | xi |
| DECLARATION OF AUTHORSHIP | xiii |
| Acknowledgements..... | xv |
| Chapter 1: Introduction..... | 1 |
| 1.1 Motivation and aim..... | 1 |
| 1.2 Thesis objectives..... | 3 |
| 1.3 Approach and thesis structure | 5 |
| Chapter 2: Context and review | 7 |
| 2.1 Introduction to context and review | 7 |
| 2.2 Background to metrology | 9 |
| 2.2.1 Dimensional metrology..... | 9 |
| 2.2.2 Measurement uncertainty | 9 |
| 2.2.3 Evaluation of measurement uncertainty..... | 10 |
| 2.2.4 Introduction to CMM..... | 17 |
| 2.2.5 Verification and calibration of CMM measurements | 18 |
| 2.2.6 Metrological application of XCT | 21 |
| 2.3 Background to X-ray physics | 29 |
| 2.3.1 Electromagnetic radiation | 29 |
| 2.3.2 Atomic structure model | 30 |
| 2.3.3 The electron beam | 31 |
| 2.3.4 Interactions of the electron beam with target material | 37 |
| 2.3.5 Interaction of X-rays with matter | 46 |
| 2.3.6 Attenuation of X-rays | 49 |
| 2.4 Background to X-ray computed tomography | 53 |

| | | |
|-------|--|----|
| 2.4.1 | Basic principles of XCT | 53 |
| 2.4.2 | Scanning configurations..... | 54 |
| 2.4.3 | X-ray tube | 54 |
| 2.4.4 | Detector types..... | 59 |
| 2.4.5 | Mechanical system..... | 60 |
| 2.4.6 | Reconstruction | 61 |
| 2.4.7 | Surface determination and dimensional measurement..... | 70 |
| 2.4.8 | Artefacts | 71 |
| 2.4.9 | Summary of the overview | 74 |

Chapter 3: An investigation of the positional stability of the focal spot and its influence on dimensional measurement in cone-beam micro-focus XCT systems..... 75

| | | |
|-------|---|----|
| 3.1 | Background to the experiments | 75 |
| 3.2 | Methodology | 79 |
| 3.2.1 | XCT system..... | 79 |
| 3.2.2 | Materials and experimental setup | 79 |
| 3.2.3 | Simulation of the focal spot drift | 83 |
| 3.2.4 | A short comparison study | 87 |
| 3.3 | Results and discussion..... | 89 |
| 3.3.1 | Analysis of cold scans | 89 |
| 3.3.2 | Analysis of hot scans | 91 |
| 3.3.3 | Long-term stability | 93 |
| 3.3.4 | Analysis of the cold scan acquired on the XCT system at the University of Padova, Italy..... | 95 |
| 3.3.5 | Analysis of the effects of the focal spot drift on size and shape of the reconstructed 3D volume of the sphere using computer simulated data..... | 96 |
| 3.4 | Conclusions and future work | 99 |

Chapter 4: An investigation of the effects of off-focal radiation on dimensional measurement in cone-beam micro-focus XCT systems103

| | | |
|-----|-------------------------------|-----|
| 4.1 | Background to the study | 103 |
|-----|-------------------------------|-----|

| | | |
|---------------------------------|--|------------|
| 4.2 | Methodology..... | 105 |
| 4.2.1 | XCT system and environmental conditions..... | 105 |
| 4.2.2 | Experimental setup and computer simulations..... | 105 |
| 4.3 | Results and discussion..... | 109 |
| 4.3.1 | Initial analysis of 2D scanned images..... | 109 |
| 4.3.2 | Magnification geometry in X-ray imaging | 112 |
| 4.3.3 | Initial evaluation of the secondary source properties..... | 115 |
| 4.3.4 | Analysis of 2D simulated images | 117 |
| 4.3.5 | Analysis of 3D volumes | 119 |
| 4.3.6 | Possible correction methods | 126 |
| 4.3.7 | Secondary source evaluation procedure..... | 129 |
| 4.4 | Conclusions and future work..... | 131 |
| Chapter 5: | An initial computer simulation study investigating the effects of the focal spot size and shape on dimensional measurement in cone-beam micro-focus XCT systems | 133 |
| 5.1 | Background to the study..... | 133 |
| 5.2 | Methodology..... | 135 |
| 5.2.1 | Computer simulations of different focal spot sizes | 135 |
| 5.2.2 | Computer simulations of different focal spot shapes | 136 |
| 5.3 | Results and discussion..... | 139 |
| 5.3.1 | Computer simulations of different focal spot sizes | 139 |
| 5.3.2 | Computer simulations of different focal spot shapes | 141 |
| 5.4 | Conclusions and future work..... | 145 |
| Chapter 6: | Thesis conclusions and future research..... | 147 |
| Appendix A..... | | 151 |
| List of References | | 155 |

List of Tables

| | |
|--|-----|
| Table 2.1 The dependence of Compton scattered X-ray photons energy on their initial energy and different scattering angles | 48 |
| Table 2.2 Attenuation coefficients dependencies | 51 |
| Table 3.1 XT H 225 M system manufacturer's specification..... | 79 |
| Table 3.2 Comparison of 3D models of the simulated steel sphere..... | 97 |
| Table 3.3 Temperature data summary | 99 |
| Table 4.1 XT H 225 M system manufacturer's specification..... | 105 |
| Table 4.2 Summary of the XCT system properties..... | 117 |
| Table 4.3 Summary of the experimentally measured and theoretically calculated image sizes of the steel gauge and the silicon window..... | 117 |
| Table 4.4 The summary of the diameter values of images due to the primary and secondary sources | 119 |
| Table 4.5 A comparison of 3D volumes of two-sphere objects. | 123 |
| Table 4.6 A comparison of 3D volumes of iron and aluminium spheres | 125 |
| Table 5.1 The results of the diameter and the form error measurements of 3D sphere models simulated using different focal spot sizes with magnification set to 80..... | 140 |
| Table 5.2 The results of the diameter and the form error measurements of 3D sphere models simulated using different focal spot sizes with magnification set to 40..... | 140 |
| Table 5.3 The results of the diameter measurements of 3D sphere models simulated using circular, elliptical and rectangular focal spots with magnification set to 80 | 142 |
| Table 5.4 The results of the form error measurements of 3D sphere models simulated using circular, elliptical and rectangular focal spots with magnification set to 80 | 142 |

List of Figures

| | |
|---|----|
| Figure 2.1 Schematic representation of the propagation of distributions | 12 |
| Figure 2.2 Reference objects for verifying metrological performance of XCT systems..... | 26 |
| Figure 2.3 Diagram of approximate binding energies of electron shells in tungsten..... | 30 |
| Figure 2.4 Schematic representation of an X-ray tube manufactured by Nikon Metrology ... | 31 |
| Figure 2.5. Schematic representation of beam path through an X-ray tube | 31 |
| Figure 2.6 Tungsten filament and the focusing cup (Wehnelt cylinder) | 32 |
| Figure 2.7 Schematic representation of space-charge limited region..... | 33 |
| Figure 2.8 Schematic representation of a typical magnetic lens | 36 |
| Figure 2.9 Schematic representation of the shape of the interaction volume..... | 38 |
| Figure 2.10 Schematic representation of the depth profile for different scattering events within tungsten target. | 38 |
| Figure 2.11 Schematic representation of the electron beam striking the target material at different tilt angles | 40 |
| Figure 2.12 Backscattering coefficient at different electron beam energies for tungsten target. | 41 |
| Figure 2.13 Backscattering coefficient for tungsten target at different angles of incidence of the electron beam. | 41 |
| Figure 2.14 Relative probabilities of X-ray and Auger effects. | 42 |
| Figure 2.15 Schematic representation of unfiltered and filtered bremsstrahlung spectra as a function of photon energy | 43 |
| Figure 2.16 Schematic representation of the production of a number of characteristic X-rays in tungsten | 45 |
| Figure 2.17 Mass attenuation coefficient for tungsten and iron as a function of X-ray photon energy | 47 |
| Figure 2.18 Schematic representation of Compton scattering..... | 48 |
| Figure 2.19 Distribution of different types of attenuation effects for lead as a function incident X-ray photon energy | 52 |
| Figure 2.20 Schematic representation of the XCT process in an industrial cone-beam XCT system..... | 53 |
| Figure 2.21 A computer simulation of the spectra for tungsten anode using different filter thickness | 56 |
| Figure 2.22 Schematic representation of the line focus principle..... | 57 |

| | |
|--|----|
| Figure 2.23 Schematic representation of the heel effect..... | 58 |
| Figure 2.24 Schematic representation of direct-conversion and indirect-conversion digital flat panel detectors | 59 |
| Figure 2.25 Schematic representation of a typical mechanical system in industrial XCT system..... | 61 |
| Figure 2.26 Schematic representation of the object and a line integral | 62 |
| Figure 2.27 Schematic representation of parallel projections taken at angles different angles..... | 63 |
| Figure 2.28 Schematic representation of the Fourier slice theorem..... | 64 |
| Figure 2.29 Sampling pattern in Fourier space based on the Fourier slice theorem | 66 |
| Figure 2.30 Illustration of the FBP | 67 |
| Figure 2.31 Schematic representation of a) fan-beam and b) cone-beam circular scan geometries..... | 69 |
| Figure 2.32 Surface determination procedure | 71 |
| Figure 2.33 Examples of XCT artefacts | 73 |
| Figure 3.1 Schematic representation of the focal spot positional shift due to the elongation of the X-ray tube | 75 |
| Figure 3.2 Schematic representation of the shift in the position of the focal spot due to thermal expansion of the target..... | 76 |
| Figure 3.3 Positions of three thermal sensors on the X-ray tube..... | 80 |
| Figure 3.4 The reference object fitted into the filter holder | 81 |
| Figure 3.5 Image processing | 82 |
| Figure 3.6 Schematic representation of the relationship between the shift of the (x,y) centre coordinates and the drift of the focal spot | 82 |
| Figure 3.7 Schematic representation of the coordinate system for simulating 2D images of the sphere | 83 |
| Figure 3.8 Schematic representation of X-ray paths through the sphere | 84 |
| Figure 3.9 The profiles of the first and the last images in the image stacks | 86 |
| Figure 3.10 The analysis of the 3D volume of the sphere using VG Studio software..... | 87 |
| Figure 3.11 Positions of three thermal sensors on the X-ray tube in comparison study | 87 |
| Figure 3.12 Temperature log of the three sensors in scan A..... | 90 |
| Figure 3.13 Drift of the (x,y) centre coordinates in the image plane in scan A. | 90 |

| | |
|--|-----|
| Figure 3.14 Correlation of the temperature log and the magnitude of the drift of the (x,y) centre coordinates in scan A. | 91 |
| Figure 3.15 Temperature log of the three sensors in scan B. | 92 |
| Figure 3.16 The drift in the (x,y) centre coordinates in the image plane in scan B. | 92 |
| Figure 3.17 The drift of the (x,y) centre coordinates in the image plane in scan C. | 93 |
| Figure 3.18 The drift of the (x,y) centre coordinates in the image plane in scan D. | 94 |
| Figure 3.19 The log of the temperature change in cold scan in the comparison study | 95 |
| Figure 3.20 The magnitude of the rolling average of the drift of the (x,y) centre coordinates in the image plane in the comparison study. | 95 |
| Figure 4.1 Images of a ruby sphere, tungsten wire and a metal part with their shadows due to the secondary focal spot effect. | 104 |
| Figure 4.2 A selection of images from the initial experimental stage of the study | 109 |
| Figure 4.3 An image of a steel edge of 0.9 mm thickness | 110 |
| Figure 4.4 Profile comparison | 111 |
| Figure 4.5 An image of a steel sphere of 6.36 mm in diameter. | 112 |
| Figure 4.6 Geometry of a magnified image produced by a point source | 113 |
| Figure 4.7 Geometry of a magnified image produced by an extended source | 113 |
| Figure 4.8 Schematic representation of image formation with the extended source | 114 |
| Figure 4.9 An approximate schematic representation of the micro-focus X-ray target assembly | 116 |
| Figure 4.10 Images of a steel gauge and a silicon disk | 116 |
| Figure 4.11 A simulated image of a steel sphere of 6.36 mm in diameter at magnification set to 9 | 118 |
| Figure 4.12 An image of a steel sphere of 6.36 mm in diameter produced with the X-ray tube settings of 75 kV, 100 μ A and magnification set to 9. | 118 |
| Figure 4.13 An image of a steel sphere of 5 mm in diameter, produced with X-ray tube settings of 100 kV, 100 μ A and magnification set to 10. | 120 |
| Figure 4.14 A 3D volume of a steel sphere of 5 mm in diameter | 120 |
| Figure 4.15 A simulation of two iron spheres of 4 mm in diameter each | 122 |
| Figure 4.16 The profiles taken through the centre of the 2D slices of 3D volumes from image stacks. | 126 |
| Figure 4.17 An image of the object made with four crossed metal wires. | 127 |

| | |
|---|-----|
| Figure 4.18 An image of the wheel scanned at X-ray tube settings of 120 kV and 80 μ A, at magnification set to 4..... | 130 |
| Figure 5.1 Schematic representation of the penumbra effect due to an extended focal spot..... | 133 |
| Figure 5.2 A representation of a circular focal spot | 135 |
| Figure 5.3 A representation of a rectangular focal spot..... | 136 |
| Figure 5.4 A representation of an elliptical focal spot..... | 137 |
| Figure 5.5 Profiles through a 2D image of a sphere simulated using different focal spot sizes and the 3D volume of the sphere | 139 |
| Figure 5.6 A relationship between the size of the focal spot and the diameter measurements of 3D sphere models | 141 |
| Figure 5.7 A relationship between focal spot shapes and diameter measurements of 3D sphere models | 143 |
| Figure A.1 Schematic representation of numerical values of pixel [x,y] with its neighbouring pixels in an image | 153 |

List of Publications

N. Flay, R. K. Leach, 2012, Application of the optical transfer function in X-ray computed tomography – a review, *NPL Report* **ENG 41**

N. Flay, W. Sun, S. Brown, R. Leach and T. Blumensath 2015, Investigation of the focal spot drift in cone-beam industrial X-ray computed tomography, *International symposium of Digital Industrial Radiology and Computed Tomography, NDT.net* **20/8**

W. Sun, S. Brown, N. Flay, M. McCarthy and J. McBride 2016, A reference sample for investigating the stability of the imaging system of x-ray computed tomography, *Meas. Sci. Technol.*, Accepted for publication 23 May 2016

N. Flay, S. Brown, W. Sun and T. Blumensath 2016, The effects of off-focal radiation in cone-beam X ray computed tomography, *Dimensional X-ray Computed Tomography Conference NPL*, Abstract

Papers in Preparation

N. Flay, S. Brown, W. Sun and T. Blumensath 2016, Investigation of the effects of off-focal radiation on dimensional measurement in micro-focus cone-beam X-ray computed tomography, *in the process of being submitted to Meas. Sci. Technol.*

DECLARATION OF AUTHORSHIP

I, Nadia Flay, declare that this thesis and the work presented in it are my own and has been generated by me as the result of my own original research.

“The investigation of the factors associated with the X-ray tube and their influence on dimensional measurement in micro-focus cone-beam industrial X-ray computed tomography systems”.

I confirm that:

1. This work was done wholly or mainly while in candidature for a research degree at this University;
2. Where any part of this thesis has previously been submitted for a degree or any other qualification at this University or any other institution, this has been clearly stated;
3. Where I have consulted the published work of others, this is always clearly attributed;
4. Where I have quoted from the work of others, the source is always given. With the exception of such quotations, this thesis is entirely my own work;
5. I have acknowledged all main sources of help;
6. Where the thesis is based on work done by myself jointly with others, I have made clear exactly what was done by others and what I have contributed myself;
7. Parts of this work have been published as:

N. Flay, W. Sun, S. Brown, R. Leach and T. Blumensath 2015, Investigation of the focal spot drift in cone-beam industrial X-ray computed tomography, *International symposium of Digital Industrial Radiology and Computed Tomography, NDT.net* **20/8**

Signed: Nadia Flay

Date: 18th July 2016

Acknowledgements

This work was supported by the National Physical Laboratory and the University of Southampton. I would like to thank Dr Thomas Blumensath (University of Southampton, UK), Dr Wenjuan Sun and Mr Stephen Brown (National Physical Laboratory, UK) and Prof Richard Leach (University of Nottingham, UK) for their continual support. I would also like to thank Dr Andrew Henning, Dr James Claverley, Massimiliano Ferrucci and Dr Michael McCarthy (National Physical Laboratory, UK), Dr Rong Su (University of Nottingham, UK), Prof John McBride, Prof Ian Sinclair and Dr Kevin Cross (University of Southampton, UK) and Prof Simone Carmignato and Filippo Zanini (University of Padova, Italy) for their contributions.

Chapter 1: Introduction

1.1 Motivation and aim

X-ray computed tomography (XCT) is a non-destructive X-ray imaging technique which allows the visualisation of external and internal structures of a solid object, as well as the acquisition of qualitative and quantitative information about an object's properties and 3-D geometries. Since its invention in the early 1970s, XCT has been extensively used in medical imaging [1], [2]. A decade later, in the 1980s, XCT was applied to material analysis and non-destructive testing. More recently, due to increasing technical sophistication, XCT has entered the field of industrial dimensional metrology [3]. In modern manufacturing, some of the most widely used systems for performing dimensional measurement are tactile and optical coordinate measuring machines (CMMs). XCT can offer advantages over traditional tactile and optical CMMs because of its ability to detect both the outer and inner geometries of an object. However, measurements obtained using XCT are often less reliable than those obtained using traditional CMMs, since they lack traceability due to difficulties in evaluating measurement uncertainty and in determining metrological performance of XCT systems [4]. This difficulty is twofold: firstly, XCT systems are complex instruments comprising many parts, which must interact correctly to produce good quality, stable and reproducible results. At present, many influence factors affecting dimensional measurement in XCT are still poorly understood. Secondly, unlike with tactile and optical CMMs, there are currently no internationally accepted standards for performance verification and calibration of XCT [5].

Current research in the area of metrological application of XCT systems is focused on developing reference objects, which can be used for the purposes of verifying metrological performance of XCT systems. Given the complexity of XCT systems, it is essential to develop reference objects, techniques and procedures which allow the qualification of individual components of XCT systems, such as the X-ray tube, mechanical system, detector, etc. To achieve this, the exact parameters of individual components which can influence the dimensional measurement need to be well understood. For example, a number of methods developed to measure certain errors associated with geometrical aspects of the detector and the rotation stage are reviewed in [6]. The aim of this thesis is two-fold:

“to identify and evaluate the parameters associated with the X-ray tube, which influence the dimensional measurement in micro-focus cone-beam XCT systems; and to propose techniques which can contribute to the development of standardised procedures for X-ray tube qualification”.

Chapter 1

This is a first of a kind study where the influence of a number of X-ray tube parameters on dimensional measurement is directly assessed and discussed.

1.2 Thesis objectives

There are a number of specific thesis objectives associated with the thesis aim:

- Thesis objective 1 – to examine the fundamentals of dimensional metrology and their implications for XCT technology.
- Thesis objective 2 – to identify the parameters associated with the X-ray tubes described in current XCT standards and literature which can influence dimensional measurement.
- Thesis objective 3 – to verify experimentally and through computer simulations how the identified parameters associated with the X-ray tube affect XCT dimensional measurements.
- Thesis objective 4 – based on experimental evidence and computer simulation results to recommend novel techniques, which can contribute to the development of standardised procedures for X-ray tube qualification.

These objectives are further refined in the following chapters.

1.3 Approach and thesis structure

Chapter 1 described the main motivation for this work, including a definition of the overall aim of the thesis and thesis objectives.

In Chapter 2, background information necessary to give context to this work is introduced. As part of this background information, a number of concepts associated with dimensional metrology and metrological application of XCT are discussed, the relevant X-ray physics and background to XCT technology are presented. Current performance verification trends and procedures for industrial XCT systems are reviewed. The parameters of the X-ray tube in micro-focus cone-beam XCT systems, which can affect the metrological performance of XCT systems, are identified. This chapter directly addresses objectives 1 and 2 of the thesis.

In Chapter 3, the experimental work investigating the positional stability of the focal spot in micro-focus cone-beam XCT system using novel test objects and strategies is presented. The results from computer simulations associated with the positional stability of the focal spot are discussed. The techniques for evaluating the positional stability of the focal spot as part of X-ray tube qualification procedure are proposed. This chapter addresses objectives 2, 3 and 4 of the thesis.

In Chapter 4, the results from the experimental investigations and computer simulation of the effects of off-focal radiation are discussed. The development of a novel test procedure for the identification and qualification of the effects of off-focal radiation, including the use of a novel test object, is presented. This chapter addresses objectives 2, 3 and 4 of the thesis.

In Chapter 5, the simulation study of the effects of the focal spot size and shape is presented and discussed. The techniques for evaluating the effects of the focal spot size and shape as part of X-ray tube qualification procedure are proposed. This chapter addresses objectives 2, 3 and 4 of the thesis.

The work is concluded in Chapter 6. The successful attainment of the thesis objectives and the overall aim of the thesis are discussed. Future work proposed in this chapter contributes to the requirements of the thesis aim and beyond.

Chapter 2: Context and review

2.1 Introduction to context and review

An introduction to the relevant background information is given in this chapter. This information relates to the areas of dimensional metrology, X-ray physics and XCT technology and will provide context for the rest of the thesis. In addition to the theoretical background, current trends in metrological application of XCT are reviewed. Based on the review, a number of factors associated with the X-ray tube in micro-focus cone-beam XCT systems, which can influence dimensional measurement, will be identified and studied. The experimental and computer simulation study of these influence factors will be discussed in the subsequent chapters of this thesis.

2.2 Background to metrology

2.2.1 Dimensional metrology

Metrology is the science (and some would say the art) of measurement [6]. A measurement tells us about a property of something and assigns a number to that property [7]. The quantity intended to be measured is referred to as measurand [8]. Engineering metrology relates to the measurement and standardisation requirements for manufacturing. It encompasses dimensional metrology, as well as mass and related quantity metrology [9]. Dimensional metrology is the field of engineering metrology which is concerned with the science and technology of measurement of the geometric features of an object, such as size, distance, angle, form or coordinate of a feature on an object, etc. [6].

Throughout human history measurement techniques and standards have changed dramatically. The foundation of the now internationally accepted metric measurement system was introduced in France in 1799, and is known as the *Système International d'Unités* (SI). Over the years, due to advances in science and technology, the SI system continued to expand to include additional units. In 1960, the 11th *Conférence Générale des Poids et Mesures* (CGPM) launched a modernised metric system [10], which now comprises seven base units, derived units and accepted units. For example, the unit of length is called a metre, and is defined as the distance travelled by light in a vacuum, in a time of $1/299\,792\,458$ of a second [11]. At the National Physical Laboratory the metre is currently realised through the wavelength of 633 nm radiation from an iodine-stabilised He-Ne laser, with an uncertainty of about 3 parts in 10^{11} [6].

The importance of precision measurement initially became apparent with the onset of the industrial revolution in the late 18th century. Throughout the years, with the development of global manufacturing, where different parts of a system can be manufactured in different countries, the importance of dimensional metrology is even more evident [6].

2.2.2 Measurement uncertainty

There are a number of concepts and terms used in metrology, formal definitions of which are outlined in the *International Vocabulary of Metrology* (VIM) [8]. One such term is the notion of a 'true value'. The true value of a measurement is the hypothetical result that would be returned by an ideal measuring instrument if there were no errors in the

measurement [9]. Since there is no such thing as a perfect measurement, each measurement needs to be accompanied by measurement uncertainty.

Measurement uncertainty is defined as a non-negative parameter characterising the dispersion of the values being attributed to a measurand [8]. In other words, the uncertainty of measurement is the doubt that exists about the result of any measurement [7]. The uncertainty should not be confused with measurement error, which is the difference between a measured value and the corresponding presumed true value (measurement error is not precisely quantifiable since the true value is unknown within the range of uncertainty) [12]. Measurement errors can be of two types: systematic and random. Systematic error is the component of the measurement error that in replicate measurements remains constant or varies in a predictable manner. Random error is the component of measurement error that in replicate measurements varies in an unpredictable manner [8]. Whenever errors and their sources are known and understood, they usually can be corrected for. The error values that are not known become a source of uncertainty [7].

Estimation of measurement uncertainty is an important process in engineering metrology as a) it allows comparison of measurement results with reference values given by appropriate specifications and standards, and b) it allows a meaningful comparison of measurement results obtained by different laboratories or manufacturing establishments [12]. Additionally, in accordance with ISO 17025 there is a general requirement for the estimation and reporting of uncertainty of measurement by all accredited laboratories [13].

2.2.3 Evaluation of measurement uncertainty

The primary international document, which establishes general rules for evaluating and expressing uncertainty in measurement, both in industry and research, is known as the Guide to the Expression of Uncertainty in Measurement (GUM) [14]. There are three main stages of uncertainty evaluation: formulation, propagation and summarising. The formulation or metrological stage consists of two steps: a) development of the measurement model which relates the input quantities to the output quantities and b) characterization of the input quantities by probability distributions¹, such as rectangular, Gaussian, t-distribution, etc., defined in terms of parameters of the probability density functions

¹ Probability distribution is a function giving the probability that the random variable takes any given value or belongs to a given set of values [14].

(PDFs)² [15]. In order for a measurement model to be a valid model, it has to encompass all possible input quantities with their probability distributions that can affect the measurement result; therefore the formulation stage is often the most challenging part of the uncertainty evaluation process.

In a measurement model all input quantities X_i are random variables³ with possible values ξ_i . The output quantity Y is also a random variable with possible values η . Instances x_i of the X_i are estimates of the input quantities, and the value $f(x_1, x_2, \dots, x_N)$ provides an estimate y for the output quantity Y . Information about the input quantities can come from a series of experimental indications, calibration certificates, expert priori knowledge, etc. A measurement model, which relates inputs to the outputs, can be a mathematical formula, a step-by-step calculation method, computer procedure or other instruction which generates a unique value of y . Multi-stage measurement models where the output quantities from previous stages serve as input quantities for subsequent stages are common in metrological applications, especially in calibration [15].

Once the measurement model is identified, the propagation and summarising stages, which involve the derivation of the estimate of the output quantity and its associated uncertainty given the information provided by the formulation stage, can be carried out. The propagation stage of uncertainty evaluation is based on the concept of the propagation of probability distributions. Given the measurement function $Y = f(X_1, \dots, X_N)$ with mutually independent input quantities X_i , for $i = 1, \dots, N$, and their associated PDFs $g_{x_i}(\xi_i)$, the PDF $g_y(\eta)$ for the output quantity Y can be determined, where ξ_i and η are possible values of X_i and Y . When the input quantities are mutually dependent, instead of N individual PDFs $g_{x_i}(\xi_i)$, there is a joint PDF $g_X(\xi)$, where $\xi = (\xi_1, \dots, \xi_N)$. Figure 2.1 shows a schematic representation of the concept of the propagation of probability distributions.

² Probability density function is the derivative of the probability distribution, providing the random variable is continuous [14].

³ Random variable is defined as a variable that can take any of the values of a specified set of possible values each with an associated probability [14].

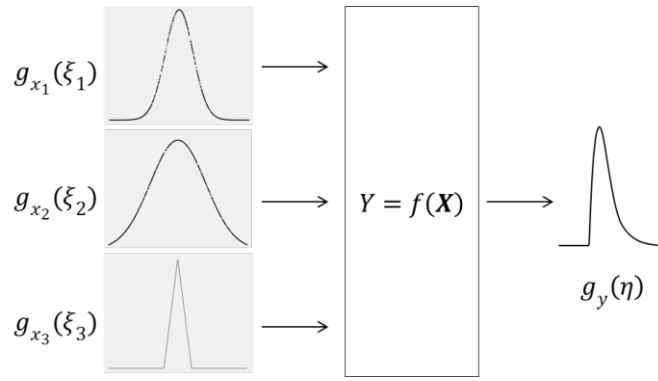


Figure 2.1 Schematic representation of the propagation of distributions. The measurement function has three input quantities X_1 , X_2 and X_3 . X_1 and X_2 are characterized by two different Gaussian PDFs $g_{x_1}(\xi_1)$ and $g_{x_2}(\xi_2)$, respectively, and X_3 is characterized by a triangular PDF $g_{x_3}(\xi_3)$. The result is a single output quantity Y , characterized by an asymmetric PDF $g_y(\eta)$ (adapted from [15]).

Three approaches can be used for the evaluation of measurement uncertainty during the propagation or computations stage: a) analytical, b) the GUM uncertainty framework and c) numerical methods. Although analytical methods for obtaining the PDF of the output quantity Y are preferable, as they do not introduce any approximations, they can only be used in very simple cases. For example, suppose there is a measurement function

$$Y = X_1 + X_2 , \quad (1)$$

where X_1 and X_2 are input quantities with expectations μ_1 and μ_2 and standard deviations $a/\sqrt{3}$ each (both are characterised by rectangular probability distributions with semi-width a). Then Y has expectation $\mu = \mu_1 + \mu_2$, standard deviation $a\sqrt{2/3}$, and is described by a symmetric triangular PDF with semi-width $2a$ [15]. For more complicated cases of the evaluation of measurement uncertainty, where the number of input variables is large and their associated PDFs are not simply all Gaussian or all rectangular, the GUM uncertainty framework or numerical methods are used.

The GUM uncertainty framework

According to the GUM uncertainty framework, uncertainty components are grouped into two categories: Type A and Type B based on the evaluation method. Type A evaluation of uncertainty refers to the statistical analysis of measured values, it is used to determine the repeatability or randomness of a measurement process. In Type A evaluation, the information about input quantity X_i is taken from N repeated independent indications

$x_{i,k}$, where $k = 1, \dots, N$. An estimate x_i of X_i is given by the arithmetic mean of the indications, calculated from

$$x_i = \bar{x} = \frac{1}{N} \sum_{k=1}^N x_{i,k}. \quad (2)$$

Their associated standard uncertainties $u(x_i)$ are given by

$$u(x_i) = \sqrt{\frac{1}{N(N-1)} \sum_{k=1}^N (x_{i,k} - x_i)^2}, \quad (3)$$

with degrees of freedom $\nu_i = N - 1$ [9].

The uncertainties associated with input estimates x_i that have not been obtained from repeated observations $x_{i,k}$ must be evaluated by scientific judgement, using all possible sources of information and the metrologist's experience [6]; this is Type B uncertainty evaluation. It is important to recognise that the Type A and Type B classifications are introduced purely to indicate the difference in the uncertainty evaluation procedures. There is no difference in the nature of the uncertainty components, as both types of evaluation are based on probability distributions. When combining standard uncertainties no distinction is made between the methods that are used to evaluate them [14].

The GUM uncertainty framework is based on the concept of the propagation of standard deviations, termed as the law of propagation of uncertainty, and the central limit theorem. Given a measurement model

$$Y = f(X_1, X_2, \dots, X_N), \quad (4)$$

where X_i are the input quantities and Y is the output quantity. The estimate y of Y , is determined from N input estimates (x_1, x_2, \dots, x_N) of (X_1, X_2, \dots, X_N) and is given by

$$y = f(x_1, x_2, \dots, x_N). \quad (5)$$

The combined standard uncertainty $u(y)$ associated with y is determined by propagating the standard uncertainties $u(x_i)$ associated with x_i and is calculated as the positive square root of the combined variance $u^2(y)$ through a linearized measurement model using

$$u^2(y) = \sum_{i=1}^N c_i^2 u^2(x_i), \quad c_i = \left. \frac{\partial f}{\partial x_i} \right|_{X_i = x_i}, \quad (6)$$

where f is the measurement function; c_i is the first order partial derivative of f with respect to X_i evaluated at x_i , and is often referred to as sensitivity coefficient, representing the ‘weight’ of each uncertainty contribution. Standard uncertainties $u(x_i)$ are determined either using Type A or Type B evaluations. The above formula is based on a first-order Taylor series approximation of $Y = f(X_1, X_2, \dots, X_N)$ and is known as the law of propagation of uncertainty. This formula assumes uncorrelated input quantities, when the input quantities are correlated the appropriate expression for the combined variance $u^2(y)$ is

$$u^2(y) = \sum_{i=1}^N \sum_{j=1}^N \frac{\partial f}{\partial x_i} \frac{\partial f}{\partial x_j} u(x_i, x_j) = \sum_{i=1}^N \left(\frac{\partial f}{\partial x_i} \right)^2 u^2(x_i) + 2 \sum_{i=1}^{N-1} \sum_{j=i+1}^N \frac{\partial f}{\partial x_i} \frac{\partial f}{\partial x_j} u(x_i, x_j), \quad (7)$$

where x_i and x_j are estimates of correlated input quantities X_i and X_j , and $u(x_i, x_j) = u(x_j, x_i)$ is the estimated covariance⁴ associated with x_i and x_j . The degree of correlation between x_i and x_j is characterized by the estimated correlation coefficient

$$r(x_i, x_j) = \frac{u(x_i, x_j)}{u(x_i)u(x_j)}, \quad (8)$$

where $r(x_i, x_j) = r(x_j, x_i)$ and $-1 \leq r(x_i, x_j) \leq 1$. Since correlation coefficients are more readily interpreted than covariances, the covariance term of equation (7) can be written as

$$2 \sum_{i=1}^{N-1} \sum_{j=i+1}^N \frac{\partial f}{\partial x_i} \frac{\partial f}{\partial x_j} u(x_i)u(x_j) r(x_i, x_j), \quad (9)$$

And equation (7) becomes

$$u^2(y) = \sum_{i=1}^N c_i^2 u^2(x_i) + 2 \sum_{i=1}^{N-1} \sum_{j=i+1}^N c_i c_j u(x_i)u(x_j) r(x_i, x_j). \quad (10)$$

As expected, if the estimated input quantities are completely independent then $r(x_i, x_j) = 0$ and equation (6) should be used in the uncertainty evaluation [14].

⁴ Covariance is a measure of mutual dependence of two variables [14].

Once the combined standard uncertainty $u(y)$ is estimated, the next step is to calculate the degrees of freedom v_{eff} attached to $u(y)$, from individual degrees of freedom v_i attached to $u(x_i)$ using the Welch-Satterthwaite formula [14]

$$v_{eff} = \frac{u^4(y)}{\sum_{i=1}^N u_i^4(y)/v_i}. \quad (11)$$

The summarizing stage of the evaluation of uncertainty involves the computation of the expanded uncertainty U_p , and hence a coverage interval for the output quantity Y . Using the estimate y of Y and the standard uncertainty $u(y)$, the expanded uncertainty is calculated as $U_p = k_p u(y)$, where k_p is a coverage factor. This value U_p defines a coverage interval $[y - U_p, y + U_p]$ associated with a particular coverage probability p , i.e. an interval that is expected to contain a certain percentage, say 95 %, of the values that can be reasonably attributed to the output quantity. Often this interval is expressed as $Y = y \pm U_p$. It is important to recognise that the provision of the coverage interval (and the coverage factor) is dependent on the knowledge of the PDF of the output quantity. The expectation value and the standard deviation in themselves do not convey information about the manner in which the values are distributed [15]. This is why the GUM uncertainty framework utilises the central limit theorem⁵ which allows the characterization of the random variable $(Y - y)/u(y)$ by the standard Gaussian distribution for $v_{eff} = \infty$ or the t-distribution for $v_{eff} < \infty$ [14].

To summarise, the correct implementation of the GUM uncertainty framework requires several assumptions: a) a linear measurement model, b) a suitability of the central limit theorem, i.e. a PDF of the output quantity can be described by either a Gaussian or a t-distribution and c) the adequacy of the Welch-Satterthwaite formula for estimating the degrees of freedom. When a measurement model identified during a formulation stage cannot meet these requirements, a different approach for the uncertainty evaluation is needed.

⁵Central limit theorem states, that given a random sample X_1, X_2, \dots, X_N of size N from any distribution with mean μ and variance σ^2 , the sample mean $\bar{X} = \frac{1}{N} \sum_{i=1}^N X_i$, will have an approximate normal distribution with mean μ and variance $\frac{\sigma^2}{N}$. The larger the sample size, the better the normal approximation [149].

A Monte Carlo method

Another method for uncertainty evaluation is known as a Monte Carlo method. It is described as a practical alternative to the GUM uncertainty framework and is undertaken numerically rather than analytically [16]. A Monte Carlo method provides much richer information in the uncertainty evaluation since it allows the propagation through a measurement model of the PDFs associated with each input quantity X_i in order to estimate the PDF of the quantity Y , rather than just the estimates of the input quantities and their standard uncertainties as in the GUM uncertainty framework. Unlike the GUM uncertainty framework a Monte Carlo method imposes no restrictions on the types of PDFs for input or output quantities.

A Monte Carlo method has a small number of steps that are repeated many times; hence the computer implementation is essential. First, the number of trials M is chosen. In order to achieve 95 % coverage interval, such that the interval length is correct to one or two decimal digits often approximately 10^6 trials are needed [15]. With the use of the random number generator, input values $x_{1,r}, x_{2,r}, \dots, x_{N,r}$ for X_1, X_2, \dots, X_N are generated by making random draws from their PDFs (where $r = 1, \dots, M$). The next step is to obtain the values y_r for Y by applying a measurement model

$$y_r = f(x_{1,r}, x_{2,r}, \dots, x_{N,r}). \quad (12)$$

The average \bar{y} of the values y_r of the output quantity is taken as the estimate y of Y ,

$$\bar{y} = \frac{1}{M} \sum_{r=1}^M y_r. \quad (13)$$

The standard deviation $u(\bar{y})$ of the values is taken as the standard uncertainty $u(y)$ associated with y calculated from

$$u^2(\bar{y}) = \frac{1}{M-1} \sum_{r=1}^M (y_r - \bar{y})^2. \quad (14)$$

The values y_r are then sorted into an increasing order $y_{(r)}$, $r = 1, \dots, M$, to give a discrete representation of the distribution function for Y , given by $\mathbf{G} = \{y_{(1)}, \dots, y_{(M)}\}$. This discrete representation is used to obtain an approximation of the distribution function of the output quantity, as well as the basis for calculating the coverage interval for the output quantity [15].

A Monte Carlo method has a number of beneficial attributes that often make it a preferred method for uncertainty evaluation. Some of these benefits are:

- a Monte Carlo method can be used for a wide variety of measurement models irrespective of whether they are linear or non-linear;
- no assumption is made regarding the type of the PDF of the output quantity Y . This is especially important for a multi-stage measurement model, where the output quantity from a previous stage can serve as the input quantity for subsequent stages;
- the method avoids the use of the concept of effective degrees of freedom;
- the calculation of the sensitivity coefficients is not required (although it can be useful for identifying the main contributions to the uncertainty associated with the estimate);
- the method is valuable for validating the results acquired through using the GUM uncertainty framework. For a fuller list of the properties of a Monte Carlo method and its benefits see [15].

2.2.4 Introduction to CMM

In order to better understand the steps that need to be implemented for XCT systems to become reliable metrological instruments, a brief introduction to traditional measurement instruments such as CMMs and their performance verification procedures is given in this section.

Throughout the years dimensional measurements were carried out by skilled personnel with the help of specially designed metrological instruments. In the mid twentieth century the first CMMs were introduced. A CMM is a measuring system with the means to move a probing system and capability to determine spatial coordinates on the surface of the part being measured [17]. The use of CMM became widely accepted in manufacturing as it offered advantages over manual measurement. The advantages include a) the automation of measurement, thus increasing the speed of measurement and decreasing the reliance on operator's skill, b) the ability to perform multiple measurements on multiple parts and c) the ability to incorporate many metrological instruments into one machine [18].

CMM can have three types of probing systems:

- an analogue or scanning probe,
- a touch trigger probe,
- an optical probe.

An analogue probe either collects points from a number of surface contacts or by continuously scanning the surface of an object. The touch-trigger probe records the machine coordinates when the stylus tip contacts the surface of an object. Optical probes use a variety of working principles. Optical CMM acquires data much faster than the tactile CMM, although its measurements tend to be less accurate [9].

2.2.5 Verification and calibration of CMM measurements

To ensure that goods worldwide are specified and measured in a common way using defined techniques, the International Organization for Standardization (ISO) publishes standards for worldwide use [6]. A standard is a document that provides requirements, specifications, guidelines or characteristics that can be used consistently to ensure that materials, products, processes and services are fit for their purpose [19]. A number of standards and guidelines have been developed in order to harmonise the performance specifications of CMM, to enable a user to make performance comparisons when acquiring a CMM and to provide a well-defined framework in which the manufacturer's specification for the system can be verified [20]. Verification is defined as a task or a series of tasks carried out at periodic intervals to ensure the CMM meets manufacturer's specification [20]. It returns a pass/fail result.

A concept that is closely related to verification is calibration. Calibration is an operation which establishes a relation between quantity values with measurement uncertainties provided by measurement standards and corresponding indications with associated measurement uncertainties. The act of calibration then uses this information to establish a relation for obtaining a measurement result from an indication [8]. Calibration procedures are specific to an instrument, range in complexity and can often vary from manufacturer to manufacturer. At the end of each calibration procedure, the uncertainty of the calibration is defined, stated on the calibration certificate and included in the uncertainty budget when the instrument is used in normal service [21]. The unbroken chain of calibrations ensures that dimensional measurements are traceable. Traceability in measurement is defined as a property of the results of a measurement whereby it can be related to stated references, usually national or international standards, through an unbroken chain of comparisons all having stated uncertainties [6].

There are a number of sources of error associated with CMM measurements, which can be categorised as spatial errors and computational errors. Spatial errors are errors in the measured position of a point on the surface of the workpiece and are determined by a) the accuracy of the CMM components, b) the probing strategy used, c) the characteristics of the

workpiece and d) the environment in which the CMM operates. Computational errors are errors in the estimated dimensions and form deviations of the workpiece and are associated with a) the software used by the CMM to estimate the geometry of the workpiece, b) the precision of the CMM computer, c) the number and relative position of points used for workpiece estimation and d) the departure of the workpiece geometry from the ideal geometry. Although modern CMMs are produced to very tight tolerances, there are still errors in the machine components due to imperfect manufacturing or alignment during assembly [22]. There are twenty-one sources of such errors, called kinematic errors of the CMM [20]. The magnitude of each kinematic error can be measured using reference standards such as interferometers, straight edges, squareness standards, etc.; this is known as CMM 'error mapping' [23]. Once kinematic errors are identified, they are corrected for in the CMM software which is known as volumetric error compensation. The error mapping and volumetric error compensation are carried out by the manufacturer on installation and, subsequently as required, since the geometry of the CMM can undergo changes over time.

The series of international standards ISO 10360 were developed to guide the acceptance and reverification tests as well as interim checks for different types of CMMs, in order to demonstrate that a CMM performs in accordance with the manufacturer's specification. For example, standards ISO 10360-2 and ISO 10360-5 are applicable to Cartesian CMMs with contacting probing systems. ISO 10360-2 describes a length measurement verification method where a calibrated test length is used, traceable to the meter, in order to establish whether the CMM is capable of measuring length within the stated maximum permissible error of length measurement for a CMM with a specified ram axis stylus tip offset (both 0 and 150), $E_{0,MPE}$ and $E_{150,MPE}$, and within the stated maximum permissible limit for the repeatability range, $R_{0,MPE}$ [24]. A calibrated test length can be a step gauge or a series of gauge blocks that conform to ISO 3650 [25], ball bars or ball plates, as well as a laser interferometer. ISO 10360-2 requires the measurement of five calibrated test lengths in seven orientations/positions; at each position each length is measured three times, making the total number of measurements 105. The length measurement error is calculated for all 105 measurements as the difference between the measured length value and the calibrated length value. The uncertainties associated with the measurements are calculated as described in ISO 23165 standard [26]. The overall decision on whether the CMM passed or failed the verification test is based on ISO 14253-1, which provides rules for proving conformity and nonconformity with specifications, taking into account the measurement uncertainty [27].

ISO 10360-5 describes another verification procedure, which tests the CMM probing system. The purpose of the test is to establish whether the CMM is capable of measuring within the manufacturer's stated value of the maximum permissible error of form, $P_{FTU,MPE}$. The test procedure is to measure a calibrated test sphere using 25 probing points. These points are

used to produce a least-squares sphere fit. The radial distances between the centre coordinate of the fitted sphere to each of the 25 probing points are then calculated. The apparent sphere form is determined as the difference between the largest and the smallest radial distance, $R_{\max} - R_{\min}$. If this value is less than $P_{\text{FTU,MPE}}$ when taking into account measurement uncertainty, the performance of the probing system is verified.

Despite the fact that the length measurement test is traceable, it is not enough to make a statement about the overall length measurement capability of the CMM due to the complicated way in which the uncertainties associated with the CMM combine [20]. In other words, the limited tests of ISO 10360 do not guarantee the measurement traceability for all possible measurement tasks. It is then up to the user to develop appropriate task-related measuring strategies that will deliver confidence in measurement results. An international standard ISO 15530-3 provides a method for the task-specific uncertainty evaluation of CMM measurements [28]. This method relies on repeated measurements of a calibrated master workpiece, similar to the unknown workpieces in their dimensions and geometry, to evaluate most of the sources of uncertainty. The ISO 15530-3 method is considered to be useful as it captures the appropriate uncertainty sources associated with the CMM system, the workpiece, measurement plan, as well as many of the extrinsic uncertainty sources and their interactions. Unfortunately, the use of a calibrated master workpiece can be both expensive and restrictive, hence, task-specific uncertainty evaluation is mostly applied to simple geometric features where calibrated workpieces of a similar geometry are readily available [29]. The ISO 15530-3 framework is compliant with both the GUM uncertainty framework and ISO 14253-2, a standard developed in order to assist the industry in the practical application of the GUM uncertainty framework. ISO 14253-2 establishes a simplified, iterative procedure of the GUM methods and is intended for geometric product specification measurement [30]. This practical procedure is known as Procedure for Uncertainty Management (PUMA) and is based on the knowledge of the dominant uncertainty components. In most cases this procedure uses very limited resources for estimating uncertainty of measurement; hence, it can often lead to a slight overestimation of uncertainty.

Before undertaking the verification procedures described in ISO 10360 and the task-specific uncertainty evaluation described in ISO 15530-3, it is required that the CMM probing qualification is performed. The probing system qualification is a procedure which establishes the parameters of a probing system necessary for measurement [17]. It must be carried out using a calibrated reference sphere supplied by the manufacturer. The qualification process involves determining the diameters of the stylus tips and the distances between them, which effectively creates an imaginary probing sphere of zero dimensions that can access any point [31]. It is essential to understand that incorrect probing system qualification will result in

incorrect future measurements, making this stage of verification process of vital importance. Those CMM systems that have additional parts, such as a rotary table, will require a further rotary table qualification prior to length measurement verification and probing system verification procedures [20].

Another approach for evaluating measurement uncertainty of the CMM measurement is by means of a virtual CMM (VCMM), such as Calypso (Zeiss) or Quindos (Hexagon Metrology), using a Monte Carlo method. VCMM attempts to simulate all the main components of a CMM's behaviour, including the geometrical and probing errors, etc. Using the VCMM in numerical simulations, it is possible in principle to analyse its behaviour for a particular measurement task and from this determine the estimates of associated uncertainties. One such method which evaluates the uncertainty by numerical simulation is described in ISO 15530-4 [32].

2.2.6 Metrological application of XCT

XCT in dimensional measurement

With continuous advances in science and technology, where components and their manufacturing techniques increase in numbers and complexity, the demand for geometrical and tolerance quality controls is particularly evident. Many industrial components, which have complex internal structures, e.g. components produced by additive manufacturing, multi-material injection moulding, etc. require techniques that can measure their internal structures without causing damage to the components. One such technology that allows the examination of external and internal parts of an object is XCT. XCT uses X-rays to obtain multiple two-dimensional images of an object of interest from different orientations. These images are then processed with the help of computers to construct a three dimensional (3D) model of the object. Using 3D volume visualisation software, e.g. VG Studio (Volume Graphics), a surface of a 3D model of the object is identified. The subsequent fitting of the appropriate geometrical features to this surface allows it to determine coordinates of various parts of the object, thus making it possible to use XCT technology in dimensional measurement.

Initial attempts to perform dimensional measurements using XCT were made in the 1990s [3], and in 2005 the first dedicated dimensional XCT system was presented to the industry [33]. At present, there is a variety of XCT systems on the market that are used for metrological purposes. XCT offers a number of advantages over traditional tactile and optical CMMs: a) it has the ability to simultaneously detect external and internal geometries

of an object, b) the ability to scan parts of complex shapes and structures, c) objects are scanned in a free-standing state, minimising risk of damage or clamping deformation and d) a complete 3D model of an object can be produced by XCT in a relatively short time compared to data processing required for CMMs. Despite the advantages, measurements obtained using XCT are often less reliable than those obtained using traditional CMMs, since they lack traceability due to difficulties in evaluating measurement uncertainty and in determining metrological performance of XCT systems [4]. This difficulty is partly due to the fact that XCT has a large number of complex, not yet well understood influence factors that affect dimensional measurement. In addition, unlike with tactile and optical CMMs, there are currently no internationally standardised guidelines and procedures for performance verification and calibration of XCT. This lack of international standards limits the ability to compare measurement results between different XCT systems, as well as XCT and other measuring systems, and is one of the main reasons why XCT is not yet accepted as a valid measuring technique by the industry [4].

Standards and guidelines in XCT

Although XCT is a fairly new technology in its application for dimensional measurement, it has been used extensively in the medical field [1], as well as in material analysis and non-destructive testing (NDT) for observing internal structures of materials and detecting material defects. Therefore, there are a number of existing international standards related to XCT technology for medical and NDT applications which cover terminology, theory and procedures for performance examination of XCT systems [34]–[45]. As stated previously, XCT systems are complex instruments, consisting of many components that must correctly interact in order to yield images that repeatedly reproduce satisfactory test results [38]. Therefore, in addition to the above mentioned standards, there are a number of standards that describe guidelines for performance verification of individual parts of XCT systems and their parameters. For example, there are standards which specify performance verification procedures of X-ray tubes for XCT and radiography in medical and NDT fields [46]–[55]. The parameters associated with the X-ray tube in XCT systems used in medical and NDT fields which are included in the standards are the stability of voltage and current, focal spot dimensions (length and width), intensity distribution across the focal spot area, dose calculation and specific safety guidelines (for medical XCT). The choice of parameters is driven by the need for good image quality for the purposes of accurate material analysis and medical diagnosis. Likewise, the parameters associated with the X-ray tube in XCT systems used for metrological application must include those parameters which influence the dimensional measurement.

VDI/VDE 2360 guidelines

The current approach to the development of standardised guidelines and procedures for XCT is based on the idea of using knowledge from traditional CMMs and applying it to XCT [56]. This approach is reinforced by the need to achieve comparability of XCT measurements with those of CMMs with tactile and optical probes [57]. At the time of writing, there is a working document prepared by a technical committee ISO/TC 213 "Dimensional and geometrical product specifications and verification", to produce guidelines for the acceptance test for verifying the performance of CMMs with X-ray sensors [57]. This working document will be a part of 10360 series; it parallels ISO 10360-2 and in part ISO 10360-5, which is for CMMs equipped with contact probing systems and ISO 10360-8, for CMMs with optical probing systems. The testing methodology between these three parts of ISO 10360 is intentionally similar [57]. The XCT part of the 10360 series is largely based on the VDI/VDE 2360 guidelines produced by the German VDI/VDE Society for Metrology and Automation Engineering (GMA), which describe the aspects of industrial application of XCT, with the purpose of specifying the procedures that insure the reproducibility and traceability of XCT measurement. The following VDI/VDE 2360 series have been published:

- Part 1.1: Basics and definitions [58]
- Part 1.2: Influencing variables on measurement results and recommendations for computed tomography dimensional measurements [59]
- Part 1.3: Guideline for the application of DIN EN ISO 10360 for coordinate measuring machines with CT-sensors [56]
- Part 1.4: Measurement procedure and comparability [60]
- Part 2.1: Determination of measurement uncertainties in measurements using CT systems (in preparation)

VDI/VDE 2360 Part 1.3 includes such performance characteristics as the length measuring error E_L and the probing error P , in accordance with ISO 10360-2. For XCT application a distinction is made between the form probing error P_F and the size probing error P_S . The form probing error P_F is the span of the radial deviations of the measurement points from the calculated regression sphere. This corresponds to the difference between the maximum distance R_{max} and minimum distance R_{min} from the probing points to the centre of the regression sphere:

$$P_F = R_{max} - R_{min} . \quad (15)$$

The regression sphere is determined using the least-squares method. The size probing error P_S is the difference between the measured diameter D_a of the sphere and the calibrated diameter D_r of the sphere,

$$P_S = D_a - D_r. \quad (16)$$

The length measurement error is determined using calibrated ball bars or calibrated ball plates. The centres of the two probed spheres are calculated for each test length from the probing points through regression analysis. The distance between the two sphere centres is the displayed value L_{ka} of the test length; the difference between the displayed value L_{ka} and the calibrated sphere distance L_{kr} is the sphere distance error S_D [56],

$$S_D = L_{ka} - L_{kr}. \quad (17)$$

In addition to the length measuring error and the probing errors, VDI/VDE 2360 Part 1.3 includes the determination of the structural resolution of an XCT system. The structural resolution in coordinate metrology describes the size of the smallest structures separately measurable. It is important to remember that since XCT measurement data in dimensional measurements always undergo a threshold value process to obtain the relevant geometrical information, the structural resolution for dimensional measurements must, in principle, be distinguished from the structural resolution in the grey scale range of the voxels (described in ISO 15708), since the structural resolution in the grey scale range of the voxels does not encompass the complete dimensional measurement chain [70]. The structural resolution for dimensional measurements D_g is specified as the diameter of the smallest sphere for which the measurement system is able to determine a diameter. The error relative to the calibrated value is stated by the manufacturer. It is recommended that the length measurement error, the form and size probing errors and the structural resolution are measured and stated for at least two different magnifications [56]. In the absence of any international or national standards for metrological application of XCT, a number of manufacturers and research organisations have adopted the VDI/VDE 2360 guidelines for performance verification of their XCT systems [3], [61], [62]. It is important to mention, however, that there is an ongoing discussion on whether the development of standards and procedures for XCT systems should be based on methods and parameters used in performance verification of traditional CMMs, since CMM and XCT are fundamentally different metrological instruments.

Verification procedures and evaluation of measurement uncertainty in XCT

As stated previously, there are currently no internationally accepted standards and procedures for performance verification and calibration of XCT; however, a number of research groups are developing reference objects which can be used for the purposes of verifying metrological performance of XCT systems. Some of these reference objects are described below.

- Reference objects comprising of calibrated spheres (figures 2.2a-e), which are used to verify length measurement capabilities of XCT systems, including scale error correction. The benefit of these objects is that only the centre-to-centre distances of spheres are used, allowing these measurements to be unaffected by the errors associated with the threshold value evaluation.
- Reference objects similar to the object comprising of spheres are calotte plate (figure 2.2f) and calotte cube (figure 2.2g). These objects are used for scale error correction and for mapping 2D and 3D anisotropies within the measurement volume [61].
- Reference objects such as a step cylinder without a bore hole (figure 2.2h) and a step wedge (figure 2.2i) can be used to investigate material-specific absorption and maximum penetration thickness parameters and to evaluate the beam-hardening effect.
- Reference objects such as a step cylinder with a bore hole in the centre (figure 2.2j), hollow cylinders (figure 2.2k) and a pan flute gauge (figure 2.2l) are used for optimising the threshold value evaluation. A ‘cactus’ gauge (figure 2.2m) allows both the scale and threshold optimisation procedures to be performed using just one object with the same properties as real workpieces.
- Reference objects such as a dismountable real workpiece-like reference object (figure 2.2n), a QFM cylinder (figure 2.2o) and CT porosity reference object (figure 2.2p) are developed to closely resemble real workpieces, and are particularly rich in a variety of geometrical features that allow testing various characteristics of CT systems.
- To verify the performance of an XCT system with regard to spatial resolution in 2D images, reference objects, such as JIMA chart (figure 2.2q), line-pair structures (figure 2.2r), sharp edges [63] are used. In addition, cylinders such as in figure 2.2k, microstructures in QFM cylinder (figure 2.2o), ‘Hourglass’ standard (figure 2.2s) and GE performance phantom (figure 2.2t) can be used for the evaluation of spatial and structural resolutions of 3D reconstructed models.



a) CT ball plate, DTU [64]



b) CT tree, DTU [64]



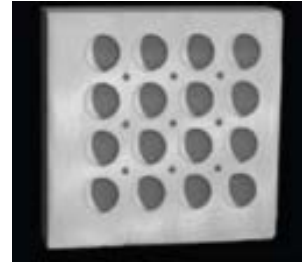
c) CT tetrahedron, University of Padova [4]



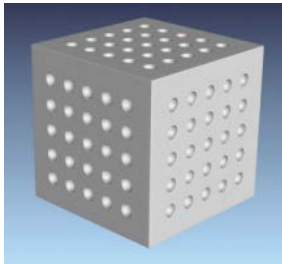
d) 27 ruby spheres, Zeiss [65]



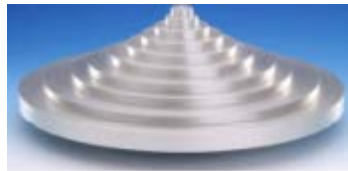
e) CT tube, DTU [66]



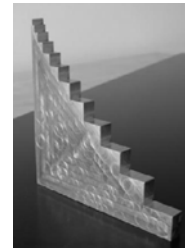
f) Calotte plate, PTB [67]



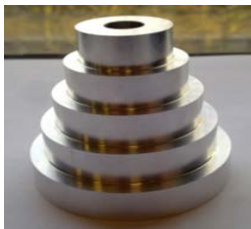
g) Calotte cube, PTB [67]



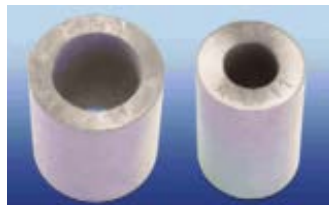
h) Step cylinder without bore hole, PTB [68]



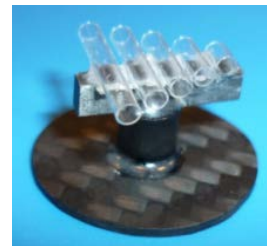
i) Step wedge [69]



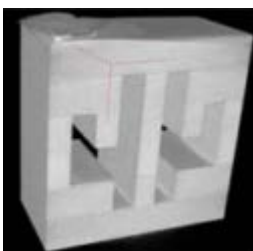
j) Step cylinder with bore hole [70]



k) Hollow cylinders, PTB [68]



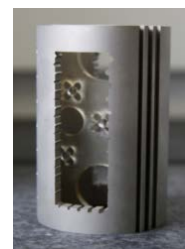
l) Pan flute gauge, University of Padova [4]



m) 'Cactus' gauge, KU Leuven [71]



n) Dismountable real workpiece-like reference object, PTB, BAM [72]



o) QFM cylinder, [4]

Figure 2.2(a-o) Reference objects for verifying metrological performance of XCT systems.

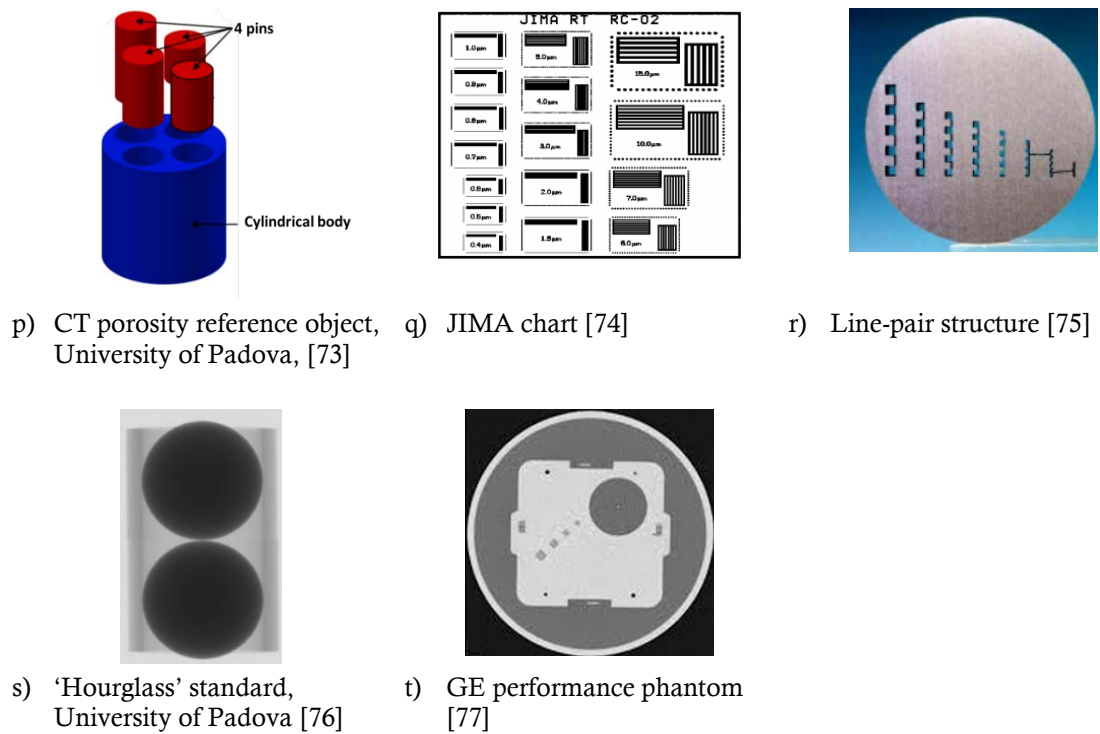


Figure 2.2(p-t) Reference objects for verifying metrological performance of XCT systems.

In addition to the design of reference objects for verifying metrological performance of XCT systems, a number of software techniques were developed which allow the evaluation of different error sources and their influence on final dimensional measurement of 3D models [78]–[84].

As mentioned previously, in traditional CMM systems verification or task-specific uncertainty evaluation procedures must be preceded by qualification procedures of individual CMM parts, e.g. the probe, the rotary table, etc. Given the fact that XCT systems are complex instruments, it is essential to develop guidelines and standards, which allow the qualification of individual components of the XCT system. To achieve this, it is necessary to understand the exact parameters of individual components that influence dimensional measurement. This study is concerned with identifying the parameters of the X-ray tube in micro-focus cone-beam XCT necessary for dimensional measurement. In order to appreciate the complexity of this task the background to X-ray physics and to XCT are presented in the following parts of the thesis.

2.3 Background to X-ray physics

A brief introduction to the background of X-ray physics is presented in this section.

2.3.1 Electromagnetic radiation

X-rays belong to a group of radiations known as electromagnetic radiation (EM radiation), the radiant energy which propagates through space or a medium at a constant speed. EM radiation can be described equally either classically as a wave or quantum-mechanically, as discrete particle-like packets of energy called quanta or photons [1]. According to a wave model, EM radiation is a wave comprising mutually reinforcing electric and magnetic fields, which oscillate perpendicular to each other and perpendicular to the direction of the wave propagation. In a vacuum, EM radiation travels at its maximum speed, the speed of light c^6 . Any wave can be characterised by its wavelength λ and frequency ν , which are related by

$$c = \lambda\nu. \quad (18)$$

Since the speed of EM radiation is constant in any given medium, its frequency is inversely proportional to its wavelength. The wavelength of X-rays is typically between 10^{-13} m to 10^{-8} m [85]. When EM radiation is described as photons, it is characterised by the energy per photon. The mathematical expression for this is

$$E = h\nu = \frac{hc}{\lambda}, \quad (19)$$

where E is photon energy, h is Plank's constant, equal to 6.62×10^{-34} Js and ν is photon frequency. The unit that is used to measure the energy of photons is the electron volt, eV⁷; if E is expressed in keV and λ in nm, then

$$E = \frac{1.24}{\lambda}. \quad (20)$$

⁶ The speed of light $c = 2.998 \times 10^8$ ms⁻¹ [1].

⁷ An electron volt is the amount of energy that an electron gains as it is accelerated through a potential difference of 1 V. X-ray energies are usually measured in kilo-electron volts, keV [91].

2.3.2 Atomic structure model

An atom is the smallest structure of ordinary matter in which the chemical identity of an element is maintained. In the Bohr model⁸, the atom consists of negatively charged electrons orbiting a positively charged nucleus, comprising protons and neutrons. Each electron occupies a discrete energy state in a given electron shell. The electron shells are assigned letters K, L, M, N ..., with K-shell being closest to the nucleus. The shells are also given a principal quantum number 1, 2, 3, 4 ..., with the principal quantum number 1 representing the K-shell. Each shell is composed of one or more subshells, denoted by an orbital quantum number l . For any shell with the principal quantum number n , l can take values from 0 to $n - 1$. The subshells are also given letters s, p, g, f ..., corresponding to $l = 0, 1, 2, 4$..., respectively. Each subshell consists of orbitals where electrons can exist, and only two electrons are allowed per orbital. The maximum number of electrons that each shell can contain is $2n^2$, where n is the principal quantum number of that shell [86]. For example, the first shell K contains one subshell 1s with one orbital and can accommodate 2 electrons; the second shell L contains 2 subshells 2s and 2p, where s has one orbital and p has three orbitals and can therefore accommodate up to 8 electrons, etc. Within the main energy shell, each subshell has a slightly different energy value and different shapes of orbitals. The energy required to remove an electron from its shell is known as the orbital binding energy or ionisation energy. The electrons in the K-shell are closest to the nucleus, and therefore are most tightly bound. The binding energy of the electron shells varies from one element to the other. For example, tungsten atom has atomic number $Z = 74$, i.e. the number of protons in the nucleus and six electron shells with approximate values of different binding energies (figure 2.3).

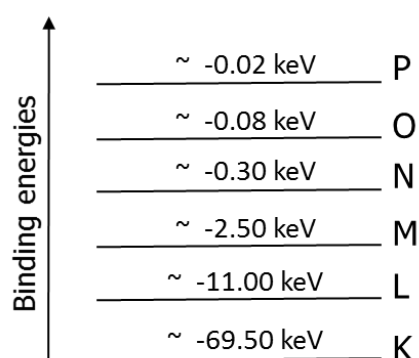


Figure 2.3 Diagram of approximate binding energies of electron shells in tungsten, atomic number $Z = 74$. Larger energies are required to free electrons from the shells that are closest to the nucleus.

⁸ The Bohr model was introduced by a physicist Niels Bohr in 1913.

X-rays are generated as a consequence of two processes: the deceleration of charged particles such as electrons caused by electromagnetic fields within atoms and the transition of electrons between the electron shells of an atom (see sections 2.3.4 and 2.3.5).

2.3.3 The electron beam

The part of the XCT system where X-rays are produced is known as the X-ray tube. Although size and appearance of the X-ray tubes might vary, the fundamental principles of X-ray generation are similar in all tubes [77]. The X-ray tube is a vacuum tube with three main components: a negatively charged cathode acting as the source of electrons, a magnetic lens for focusing the beam of electrons and a positively charged anode containing a metal target. As an example, figure 2.4 shows a typical X-ray tube in an industrial metrology XCT system [87]; figure 2.5 demonstrates a path of an electron beam through an X-ray tube from its emission to the production of X-rays [88].

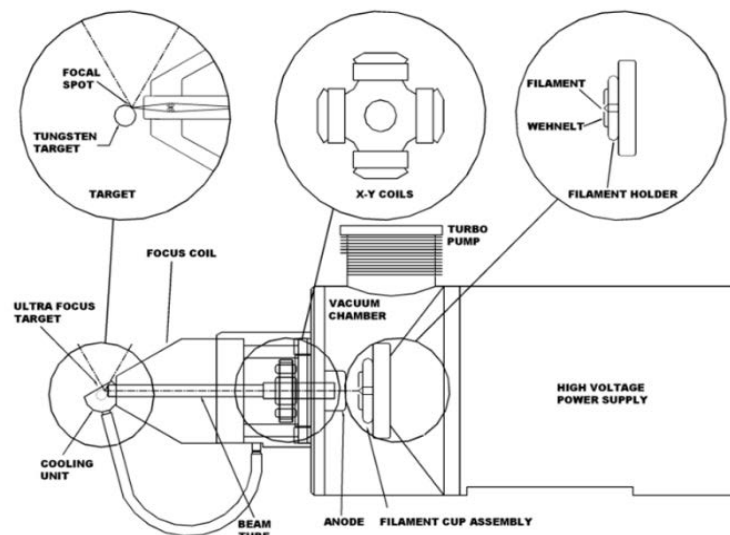


Figure 2.4 Schematic representation of an X-ray tube manufactured by Nikon Metrology [87].

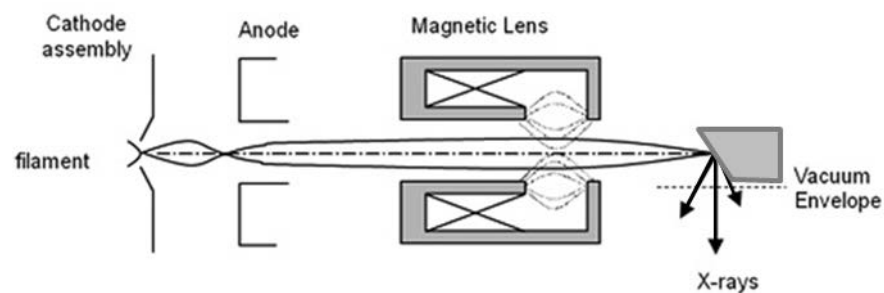


Figure 2.5. Schematic representation of beam path through an X-ray tube, Nikon Metrology [88].

The cathode includes a filament commonly made of thin tungsten wire and a focusing cup, known as the Wehnelt cylinder (figure 2.6). Tungsten is used because it has a high melting temperature of 3695 K and can conveniently be shaped into a strong thin wire.

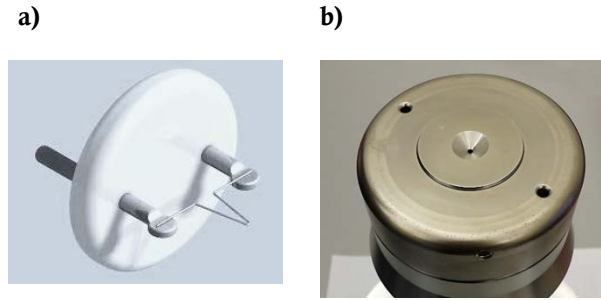


Figure 2.6 Tungsten filament (a); and the focusing cup (Wehnelt cylinder) (b).

Production of the electron beam

As the current passes through the filament, it causes it to heat up. When this thermal energy is absorbed by tungsten atoms, electrons are released from the metallic surface via a process known as thermionic emission, where they are effectively ‘boiled off’ the filament. The number of emitted electrons depends mainly on the temperature of the wire, as well as on its geometrical dimensions and material constants [89]. The physics of thermionic emission is summarised by Richardson’s law, which relates the density of the emitted electron current j_e , to the operating temperature T :

$$j_e = A_0 T^2 e^{-\frac{W}{kT}}, \quad (21)$$

where k is Boltzmann constant⁹, T is the temperature in Kelvin, W is the work function¹⁰ and A_0 is material constant. For tungsten $W = 4.5$ eV and $A_0 = 60 \text{ Acm}^{-2}\text{K}^{-2}$ [90].

The emitted electrons form a cloud around the filament, known as the space charge. This cloud is negatively charged and prevents more electrons from leaving the filament. At the same time, the filament acquires a positive charge due to the loss of the electrons, thus attracting some of these electrons back. For a given filament temperature, the state of equilibrium is quickly reached where the number of the emitted electrons is equal to the number of the returning electrons, allowing the overall number of the electrons in the space charge to remain constant [91]. When the accelerating voltage V_0 is applied between the

⁹ Boltzmann constant relates kinetic energy at the individual particle level with temperature, and is equal to $8.6 \times 10^{-5} \text{ eVK}^{-1}$.

¹⁰ Work function is the minimum energy needed to remove an electron from a solid.

cathode and anode, the electrons travel towards the anode producing current. For low voltages, this relationship is described by the Child-Langmuir law:

$$j_c = \frac{4\pi\epsilon_0}{9} \sqrt{\frac{2e}{m}} \frac{V_0^{3/2}}{d^2}. \quad (22)$$

Here, j_c is the current density at the emitter surface, ϵ_0 is the vacuum dielectric constant, e and m are the charge and the mass of an electron, respectively, d is the distance between the anode and the cathode and V_0 is the accelerating voltage [89]. The low accelerating voltage region is known as the space-charge limited region, where the current is dependent on the voltage. As the accelerating voltage increases, greater numbers of electrons from the space charge are attracted to the anode, until the current reaches its maximum, known as saturation current. Beyond this point, increasing the accelerating voltage will not increase the magnitude of the current (figure 2.7).

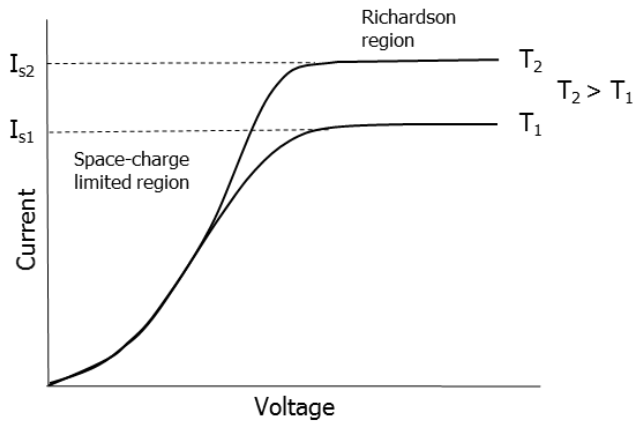


Figure 2.7 Schematic representation of space-charge limited region. As the temperature of the filament is increased from T_1 to T_2 , the rate of electron emission from the filament is also increased, hence the saturation current increases from I_{s1} to I_{s2} . The saturation characteristic is due to the limited number of electrons that can be emitted from the filament for a given filament temperature.

At high accelerating voltages only a small portion of the emitted electrons returns back to the filament, practically eliminating the space-charge; therefore, the current density is mainly determined by the temperature of the filament as described by Richardson law. As the electrons are accelerated through the potential difference, they acquire kinetic energy reaching velocity greater than half the speed of light. This stream of electrons is often referred to as the electron beam. The velocity of the electrons can be determined through the following energy conservation formula [92]:

$$\frac{1}{2}mv^2 = eV_0, \quad (23)$$

where m is the mass of the electron¹¹, e is the charge of the electron¹², v is the electron velocity and V_0 is the potential difference between the cathode and the anode. Due to the mutual repulsion of the electrons, the electron beam would tend to spread out, hitting a wide area of the anode. In order to achieve a focused, controllable and stable electron beam that can pass through the centre of the anode ring, a small negative bias of up to a few hundred volts with respect to the filament is applied to the focusing cup [89]. This bias produces repulsive electrostatic field, which condenses the cloud of electrons by localising the emission from the filament to its tip above the aperture of the focusing cup and forming a focused electron beam.

Steering and focusing of the electron beam

As the electron beam enters through the anode ring, it needs to be steered so that its path is as close as possible along the central axis of the beam tube. Failure to align the beam may result in electrons being lost from the beam, thus affecting the radiation output and potentially damaging the tube. For this purpose two pairs of coils are mounted between the anode ring and the magnetic lens (figure 2.4). Passing a current through these coils steers the electron beam facilitating source alignment [87]. Fluctuations in the current through the coils can affect the quality of the beam alignment.

Since electrons are negatively charged, they have a tendency to repel each other as they are accelerated through the beam tube, making the electron beam diverge. In order to focus the electron beam onto a small part of the target, the beam goes through the magnetic lens located just above the target. A simple magnetic lens consists of a soft iron core surrounded by a helically wound conducting coil carrying a direct current [93]. Such a magnetic lens produces inhomogeneous rotationally symmetric magnetic field (figure 2.8a). When an electron travelling at velocity \mathbf{v} enters the magnetic field \mathbf{B} , it experiences a force which varies continuously both in magnitude and direction and is represented by the Lorentz force law:

$$\mathbf{F} = -e(\mathbf{v} \times \mathbf{B}). \quad (24)$$

¹¹ The mass of the electron, m is 9.11×10^{-31} kg

¹² The charge of the electron, e is -1.60×10^{-19} C

The term $\mathbf{v} \times \mathbf{B}$ is a vector cross-product, where the resulting force \mathbf{F} is perpendicular to both the velocity of the electron \mathbf{v} and the magnetic field \mathbf{B} , which are at angle ϑ to each other. The relative directions of \mathbf{v} , \mathbf{B} and \mathbf{F} are given by Fleming right-hand rule [90]. Since \mathbf{F} has no force component in the direction of motion, the speed of the electron remains unchanged; however, as the electron passes through the magnetic lens, the direction of the magnetic field \mathbf{B} and of electron velocity \mathbf{v} changes continuously, thus changing the magnitude and the direction of the magnetic force. The magnitude of the magnetic force at any given point in a plane can be calculated using

$$F = evB\sin(\vartheta). \quad (25)$$

It is clear from equation (25) that if the initial motion of an electron in the magnetic lens is along the lens axis (optical axis), the electron will experience no magnetic force, and its path will remain unchanged. Now, the magnetic field \mathbf{B} can be resolved into its constituent components: the radial component \mathbf{B}_r and the axial component \mathbf{B}_z (figure 2.8a). The electron beam is directed through the lens in such a way that most electrons enter the magnetic lens off optical axis and parallel to the z-axis. Initially, the electron has only a velocity component \mathbf{v}_z , which is parallel to the z-axis; the electron is affected by the radial component \mathbf{B}_r and experiences the magnetic force in the azimuthal direction \mathbf{F}_φ (figure 2.8b). This force causes the electron to travel in helical path along the lens, giving rise to the azimuthal component of velocity \mathbf{v}_φ . In turn, \mathbf{v}_φ interacts with the axial component of the magnetic field \mathbf{B}_z , giving rise to the magnetic force in the radial direction toward the optical axis \mathbf{F}_r (figure 2.8c). As a result, the electron spirals around the lens closer and closer to the optical axis, causing a parallel electron beam to converge.

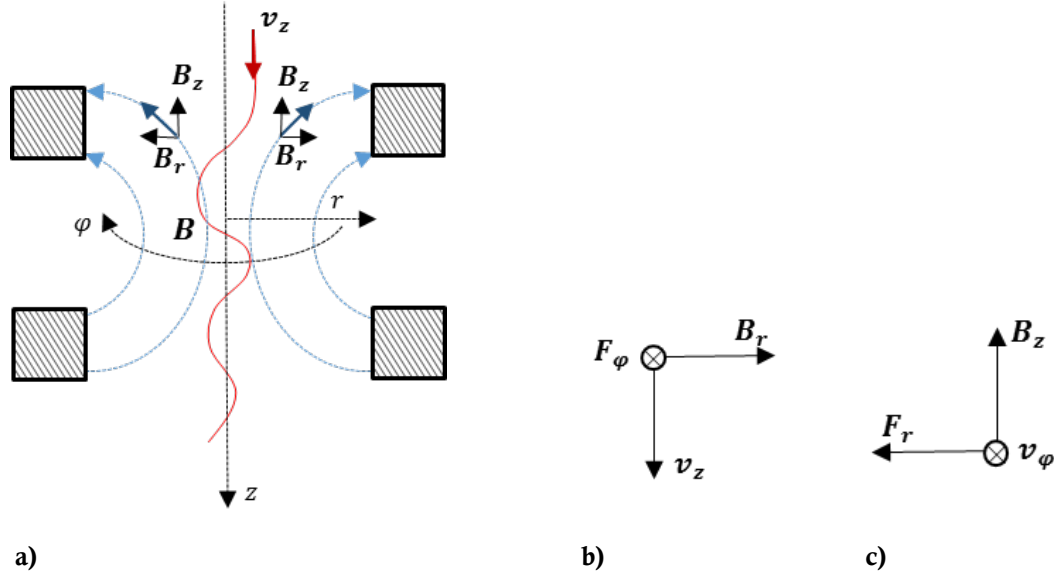


Figure 2.8 a) Schematic representation of a typical magnetic lens with cylindrical coordinates r, φ, z , magnetic field components B_r and B_z and a helical path of an electron with its initial velocity v_z ; b) the interaction of the electron with its initial velocity v_z with the radial component of the magnetic field B_r , produces a magnetic force in the azimuthal direction F_φ , which gives rise to the velocity component v_φ in the azimuthal direction; c) As v_φ interacts with B_z it produces the magnetic force F_r in the radial direction sending the electron towards the optical axis (adapted from [94]).

The distance between the centre of the lens to the point of convergence of the beam is known as the focal length of the lens [95]. For most lenses, the focal length of the magnetic lens f can be estimated using

$$f = \frac{KV}{I^2}, \quad (26)$$

where V is the accelerating voltage and K is a constant, based on the number of turns in the coil and the geometry of the coil and I is a current put through the coil [95]. Changing the magnitude of the accelerating voltage will alter the focal length of the lens; therefore, for each kV setting, the strength of the current is adjusted automatically in order to achieve the required diameter of the electron beam. Irregularities in the internal geometries of the magnetic lens, fluctuations in coil current, as well as fluctuation in the voltage supply can all influence the consistency of the performance of the lens, thus affecting the size and stability of the electron beam and, ultimately, the imaging quality of the X-ray system.

2.3.4 Interactions of the electron beam with target material

As the high speed electron beam passes through the magnetic lens, it strikes the target material, where the electrons undergo a number of possible elastic and inelastic interactions or scattering events [89]. Elastic scattering occurs when the kinetic energy of the incident electron is preserved whilst its direction of travel is modified; in elastic scattering no energy from the beam is transferred to the material. The result of elastic scattering is the generation of backscattered electrons. Inelastic scattering occurs when the incident electron loses its energy through the interactions with the electrons in the atoms of the material. Inelastic scattering can take several forms:

- Secondary electrons
- Auger electrons
- Continuous X-ray spectrum, bremsstrahlung
- Characteristic X-rays
- Heat
- Cathodoluminescence¹³

The area where the electron beam hits the surface of the target is called the focal spot [91]. Interactions of the electron beam with the target, however, happen within a certain volume of the target material, known as the interaction volume. The size and shape of the interaction volume depends on the following parameters: the atomic number or density of the material, the accelerating voltage, the magnitude of the beam current and the angle of incidence. The shape of the interaction volume resembles a teardrop for materials with lower atomic number Z (such as molybdenum with $Z = 42$) and a hemisphere for materials with higher Z (such as tungsten with $Z = 74$) (figure 2.9) [96]. Some scattering events can originate only within certain depths of the interaction volume; this depth depends on the energy that is required to produce a given effect. Other scattering events originate throughout the volume but can escape the target and be detected only if produced near the surface. Figure 2.10 shows a schematic depth profile for different scattering events within tungsten target for an incident electron beam with energy of around 100 keV [89].

¹³ Cathodoluminescence is the emission of visible light by the target material when it is bombarded by fast moving electrons. This effect occurs in semiconductor materials and is not applicable to a tungsten target [90].

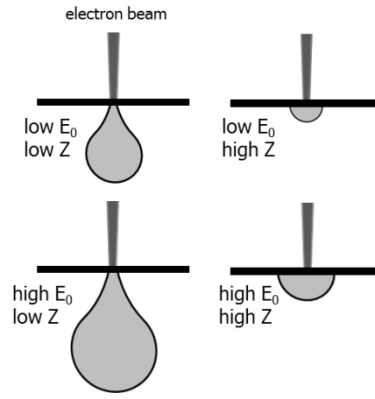


Figure 2.9 Schematic representation of the shape of the interaction volume, and its dependence on the electron beam energy E_0 and the atomic number Z of the target material.

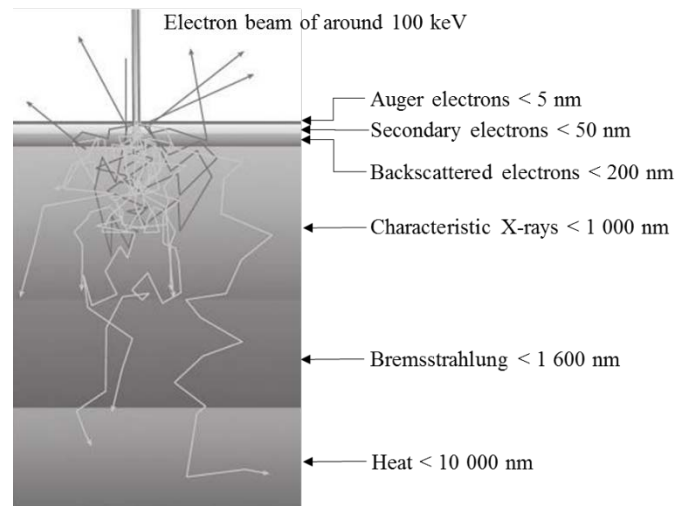


Figure 2.10 Schematic representation of the depth profile for different scattering events within tungsten target for an incident electron beam with energy of around 100 keV [89].

As the electron beam traverses the target material, it loses its energy through various interactions until it comes to a stop. For an electron that is incident perpendicular to the target, the depth of electron penetration x is approximated by an empirical expression

$$x = \frac{0.1V_0^{1.5}}{\rho}, \quad (27)$$

where x is in μm , V_0 is the accelerating voltage in kV, and ρ is the material density in gcm^{-3} [97]. For example, if an electron is accelerated through $V_0 = 100$ kV and strikes tungsten material of $\rho = 18.82$ gcm^{-3} , then its penetration depth will be around $x = 5.31$ μm . A single electron can undergo a number of scattering events before coming to rest. A theoretical

expression for the range r of the electron, i.e. the straight line distance between the point of incidence and the final destination is

$$r = \frac{2.76 \times 10^{-2} A V_0^{1.67}}{\rho Z^{0.89}}. \quad (28)$$

Here, r is in μm , A is average atomic weight in gmole^{-1} , V_0 is the accelerating voltage in kV, and ρ is the material density in gcm^{-3} and Z is the atomic number [98]. For example, if an electron is accelerated through $V_0 = 100$ kV and strikes tungsten material of $\rho = 18.82 \text{ gcm}^{-3}$, $A = 183.84 \text{ gmole}^{-1}$ and $Z = 74$ then its range is around $r = 12.80 \mu\text{m}$.

Backscattered electrons

Backscattered electrons are those electrons in the beam which are scattered at angles above 90° with respect to the direction of motion due to their interactions with the atomic nuclei of the target material. The energy of the backscattered electron depends on its original energy and the number of scattering interactions it undergoes before escaping the material. The majority of backscattered electrons will have energies only slightly lower than those of primary electrons; however, since some primary electrons can undergo initial inelastic scattering before being finally backscattered, their energies can be as low as 50eV. The fraction of the backscattered electrons strongly depends on the atomic number Z of the target material, and can be approximated by the backscattering coefficient n_b , where

$$n_b = n_{b20} \left[1 + a \ln \left(\frac{E_0}{20} \right) \right]. \quad (29)$$

Here,

$$a = -0.11128 + 3.0289 \times 10^{-3} Z - 1.5498 \times 10^{-5} Z^2, \quad (30)$$

$$n_{b20} = -5.23791 \times 10^{-3} + 1.5048371 \times 10^{-2} Z - 1.67373 \times 10^{-4} Z^2 + 7.16 \times 10^{-7} Z^3 \quad (31)$$

and

$$Z = w_1 Z_1 + w_2 Z_2 + w_3 Z_3 \dots, \quad (32)$$

where, w_i and Z_i are the weight fraction and the atomic number of element i of the target material, respectively and E_0 is the electron impact energy in keV [99]. Increasing the tilt

angle ϕ ¹⁴ between the incoming electron beam and the target material increases the backscattering coefficient, with a larger portion of the electrons ‘backscattered’ in the forward direction [100]. The relationship of the backscatter and the tilt angle can be approximated using an empirical formula

$$n_b(Z, \phi) = (1 + \cos(\phi))^{-\frac{9}{\sqrt{Z}}}, \quad (33)$$

where Z is the atomic number of the target material and ϕ is the tilt angle [89], [100]. This phenomenon is demonstrated in figure 2.11.

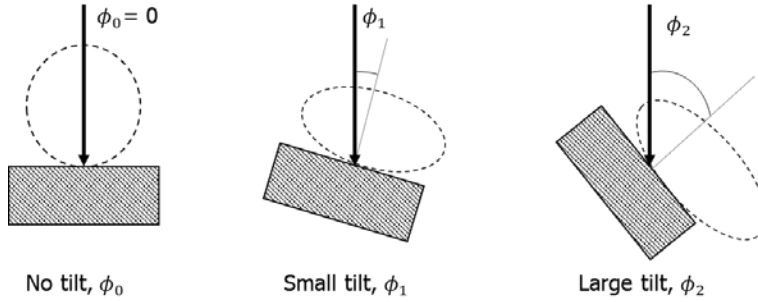


Figure 2.11 Schematic representation of the electron beam striking the target material at different tilt angles, ϕ_i . Increasing the tilt angle changes the radial distribution of the backscattered electrons (marked with dotted lines), where a larger number of these electrons are ‘backscattered’ in the forward direction.

Formulae (29) to (33) were used to evaluate the backscattering coefficient for tungsten target with different incident electron energies and different tilt angles. Figure 2.12 demonstrates that for the electron beam with energies ranging from 75 keV to 225 keV at normal incidence, the increase in backscattering coefficient amounts to only around 3 %. On the other hand, due to the cosine relationship in formula (33), as the tilt angle deviates from the normal by more than about 20°, the backscattering coefficient increases significantly from around 0.5 to unity (figure 2.13). This increase in backscatter reduces the overall number of electrons useful for generating X-rays; therefore, the magnitude of the tilt angle is one of the main factors that needs to be considered in the design of X-ray tubes [89]. In addition, due to their high energy, backscattered electrons can serve as the source of unwanted ‘secondary focal spot’ phenomenon (discussed in more detail in section 4).

¹⁴ The tilt angle ϕ is defined as the angle between the incident electron beam and the normal to the surface of the target.

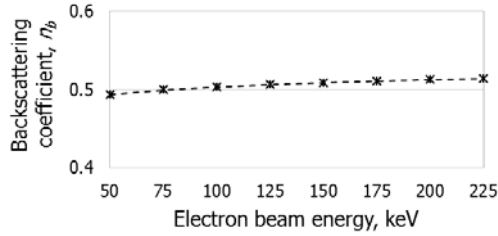


Figure 2.12 Backscattering coefficient at different electron beam energies for tungsten target.

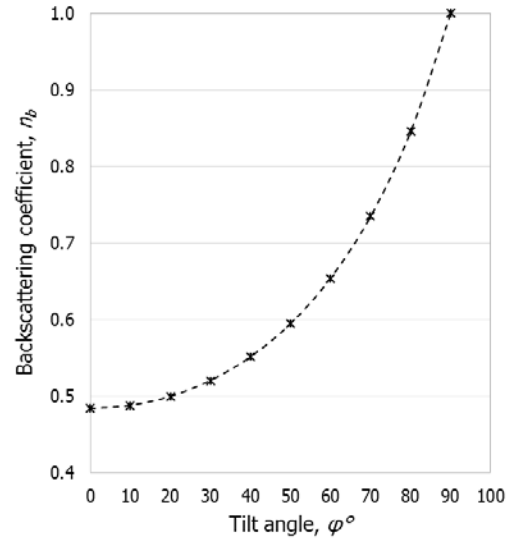


Figure 2.13 Backscattering coefficient for tungsten target at different angles of incidence of the electron beam.

Secondary electrons

Secondary electrons are produced when a primary electron from the beam excites a weakly bound electron from the outer-shell in the target material and loses some of its energy in the process. The excited electron moves towards the surface of the target, whilst undergoing elastic and inelastic scattering. It can then escape the target material, providing its energy is higher than the surface work function energy. The mean free path of a secondary electron in many metals is about 1 nm. Therefore, even though these electrons are produced throughout the interaction volume, only those that originate within 1 nm from the target surface can escape the target. Secondary electrons can have energy of up to 50 eV, although 90 % of them are below 10 eV [101].

Auger electrons

When a fast moving electron from the electron beam removes an inner shell electron in an atom of the target material, a vacancy is created. This vacancy is quickly filled with an electron from a higher shell, releasing energy. The released energy can either produce a characteristic X-ray photon or be transferred to another electron in the same shell or one of the outer shells of the atom, emitting an Auger electron. The kinetic energy of the Auger electron E_{kin} is

$$E_{kin} = E_A - E_B - E_C, \quad (34)$$

where E_A , E_B and E_C are the inner level, first outer shell and second outer shell electron energies, respectively. For example, if an incoming electron removes an electron from the K-shell, then the vacancy is filled with the L-shell electron and the released energy is transferred to another L-shell electron, the notation for this process is called a KLL transition. Relative probabilities of X-ray and Auger electron emissions depend on the atomic number Z of the target material, as illustrated in figure 2.14. For materials with low atomic number, when energy is released by filling in the electron vacancies in the K and L shells of an atom, only a few characteristic X-rays are emitted; in the vast majority of interactions this energy is transferred to produce Auger electrons. On the other hand, for materials with a high atomic number, the probability of characteristic X-ray emission due to the K-shell electron vacancy is close to unity. In high Z number materials, Auger electrons are mainly produced due to electron vacancies in higher electron shells.

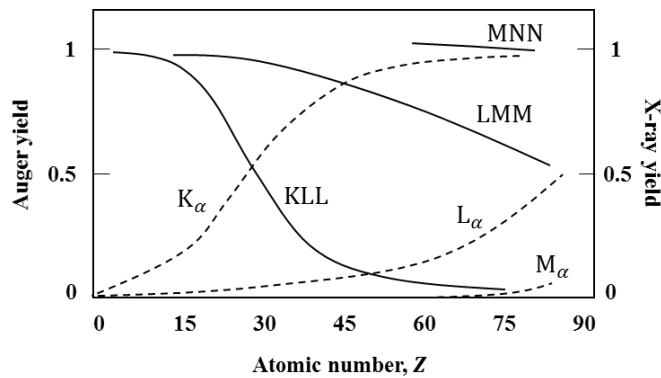


Figure 2.14 Relative probabilities of X-ray and Auger effects. K_{α} , L_{α} , M_{α} are the characteristic X-rays produced when an electron vacancy is filled in the K, L and M shells, respectively. KLL, LMM and MNN are possible transitions for Auger electrons (adapted from [102]).

Continuous X-ray spectrum – bremsstrahlung

As the high energy electron beam enters the target material, some electrons are decelerated or stopped completely by the strong electromagnetic field of atomic nuclei of the material. The decelerating electrons lose their kinetic energy, thus producing X-ray photons. All degrees of electron deceleration are possible; therefore, the resulting X-rays have a continuous range of energies making the X-ray beam to be polychromatic in nature. When the entire energy of the incident electron is transformed into a single X-ray photon, this photon has maximum possible energy E_{max} equivalent to the accelerating tube voltage V . The minimum wave length of an X-ray λ_{min} can then be calculated by rearranging equation (20) to give

$$\lambda_{min} = \frac{1.24}{E_{max}}. \quad (35)$$

Here, λ_{min} is in nm and E_{max} in keV; this is known as the Duane–Hunt law. The continuous energy spectrum is called bremsstrahlung (a German term meaning “breaking radiation”). The bremsstrahlung intensity¹⁵ I_E at photon energy E can be approximated by Kramers’ equation,

$$I_E = C i_b t Z (E_0 - E). \quad (36)$$

Here, I_E is in JMeV^{-1} , C is a constant in $\text{JMeV}^{-2}\text{mA}^{-1}\text{s}^{-1}$, i_b is the electron beam current in mA, t is the exposure time in s, Z is the atomic number of the target material and E_0 is the electron beam energy in MeV [103], [104]. This equation gives a straight line and represents theoretical unfiltered bremsstrahlung spectrum. In reality, the unfiltered spectrum is modified/filtered through the absorption of some of the photons by the target, the walls and aluminium or beryllium aperture of the X-ray tube. The modification of the spectrum is predominantly in the low energy region, high energy X-ray photons distribution remains largely unaffected (figure 2.15).

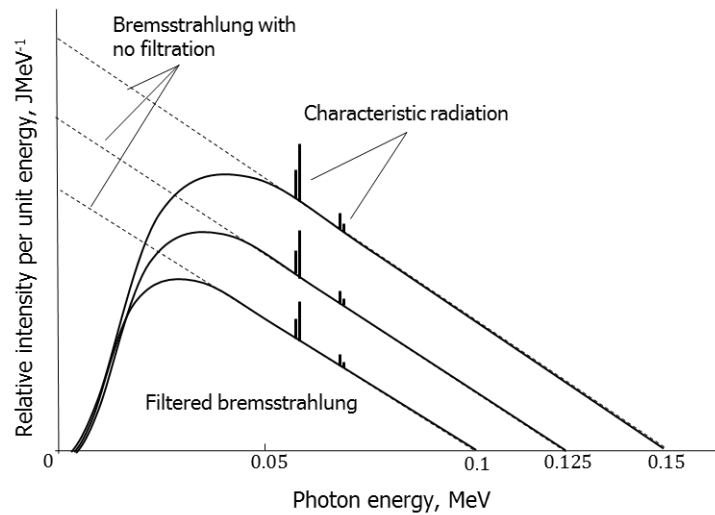


Figure 2.15 Schematic representation of unfiltered and filtered bremsstrahlung spectra as a function of photon energy, with superimposed characteristic emission lines. When the values of the i_b and t are kept constant, the change in V shifts the spectrum in parallels along the axis, without changing its slope.

¹⁵ The intensity of an X-ray beam is defined as the number of X-ray photons in the beam multiplied by the energy of each photon [91].

The total bremsstrahlung intensity I_{total} can be approximated by integrating equation (36) over E , giving

$$I_{total} = C'i_b t Z E_0^2 = C''i_b t Z V^2. \quad (37)$$

This equation demonstrates that for a given atomic number Z , a fixed tube current and exposure time, the amount of radiation produced is proportional to the square of the accelerating tube voltage V . This relationship is valid for unfiltered bremsstrahlung X-ray spectrum; the inherent and added filtration can introduce a different power exponent for V [103]; on the other hand, when the accelerating voltage is fixed, the I_{total} increases proportionally to the tube current and the exposure time. The conversion efficiency from kinetic electron energy to bremsstrahlung energy can be described by

$$\eta = kZV. \quad (38)$$

where k is a material constant found by Kramers theoretically to be equal to $9.7 \times 10^{-7} \text{ kV}^{-1}$, and the acceleration voltage V is given in kV [92]. It is clear that the process of generating bremsstrahlung is extremely inefficient, for example, if an incident electron beam accelerated through the voltage of 225 kV hits tungsten target, only 1.5 % of all electron energy is converted into bremsstrahlung.

Characteristic X-rays

Another mechanism for generating X-rays is known as characteristic radiation. When a fast moving electron from the electron beam removes an inner shell electron in an atom of the target material, a vacancy is created. This vacancy is quickly filled with an electron from a higher shell, emitting a characteristic X-ray photon. The energy of the characteristic X-ray is the difference between the electron binding energy of the respective shells:

$$E_{characteristic \text{ X-ray}} = E_{vacant \text{ shell}} - E_{transition \text{ shell}}. \quad (39)$$

It is clear that in order to generate a characteristic X-ray, the incident electron needs to have enough energy to overcome the binding energy of the inner shell electron. Since different elements have their own unique electron binding energies, the wavelength of characteristic X-rays is representative of the atoms that are being ionised. If the X-ray photon is the result of the vacancy in the K-shell, it is called K_α or K_β characteristic X-rays, depending on whether the vacancy was filled by an electron from the adjacent L-shell (for K_α) or by an electron from the M-shell (for K_β). (Similar description is applied to characteristic X-rays

from other shells; for example, if a vacancy in the L-shell is filled by an electron from the M-shell, the X-ray photon is called L_α). Figure 2.16 demonstrates the production of K_α and K_β characteristic X-rays in tungsten.

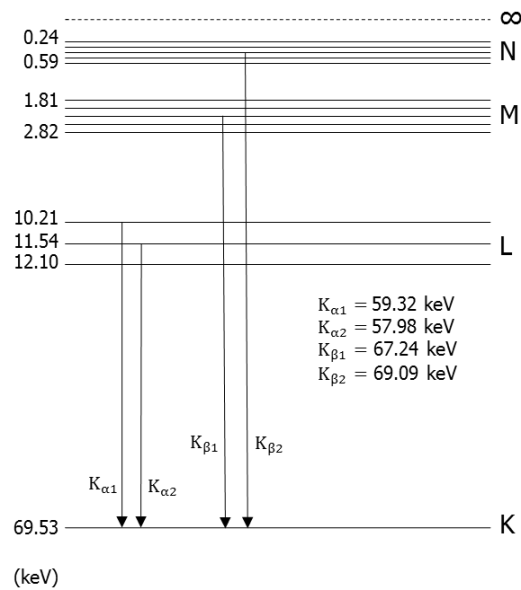


Figure 2.16 Schematic representation of the production of a number of K_α and K_β characteristic X-rays in tungsten (adapted from [105]).

The total X-ray spectrum produced by an incident electron beam is the combination of the bremsstrahlung radiation with superimposed lines from characteristic radiation (figure 2.15). In addition to the bremsstrahlung and characteristic radiation produced by the primary electrons, some of the X-rays are re-absorbed by the target material, producing secondary bremsstrahlung and characteristic radiation of lower energies.

Heat

When an incident electron beam hits the target material, the primary electrons undergo a cascade of elastic and inelastic collisions generating heat, thus significantly increasing the target temperature. The maximum increase in temperature for a material can be approximated by

$$\Delta T = \frac{4.8E_0i_b}{C_t d_0}. \quad (40)$$

Here, E_0 is the energy of the electron beam in keV, i_b is the beam current in μA , C_t is the thermal conductivity of the target material in $\text{Wcm}^{-1}\text{K}^{-1}$ and d_0 is the diameter of the electron

beam in μm [106]. This equation demonstrates that for a given target material, electron beam energy and beam current, there is a limit to how small the beam diameter can be without damaging the target. For example, if an electron beam with $E_0 = 100 \text{ keV}$, $i_b = 100 \mu\text{A}$ and $d_0 = 10 \mu\text{m}$, hits tungsten target with $C_t = 1.74 \text{ Wcm}^{-1}\text{K}^{-1}$, the target will experience temperature increase of around 2760 K; increasing i_b to 140 μA will bring the target to the temperature just below its melting point of 3695 K. To avoid burning the target, many X-ray tubes automatically increase the diameter of the electron beam ('defocus the beam') in response to operator's requested voltage and current settings. In addition, most modern X-ray tubes are equipped with target cooling systems to dissipate the heat more effectively.

2.3.5 Interaction of X-rays with matter

There are four basic ways the way X-rays interact with matter: photoelectric effect, Compton scattering, Rayleigh scattering and pair production.

Photoelectric effect

Photoelectric effect describes a mechanism by which an incident X-ray photon with energy greater than the binding energy of an inner-shell electron interacts with such electron, ejecting it from its orbit. The ejected electron is called a photoelectron. As the photoelectron is ejected from its shell, a cascade of electron transitions occur, resulting in the production of characteristic X-rays, as described in section 2.3.4. During this process the incident X-ray photon gives off its entire energy. The photoelectron acquires kinetic energy E_{pe} , equal to the difference between its binding energy E_b and the energy of the incident X-ray E_0 :

$$E_{pe} = E_0 - E_b . \quad (41)$$

It has been demonstrated experimentally that the probability p of the photoelectric effect follows the following rule of thumb,

$$p \propto \frac{Z^3}{E_0^3} . \quad (42)$$

where Z is the atomic number of the target material [1]. According to equation (42), the probability of the photoelectric effect decreases with increasing energy; however, for all elements, this decreasing trend is interrupted by a sharp rise, called the absorption edge. The absorption edge occurs when the energy of the incident X-ray photon E_0 is only just above

the binding energy E_b of a particular subshell for a given element. This effect is demonstrated in figure 2.17.

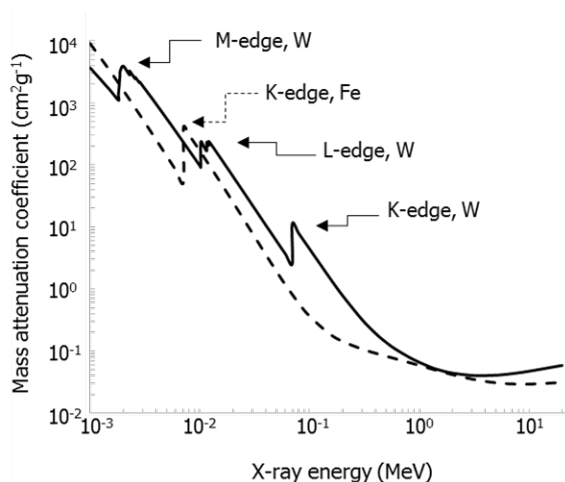


Figure 2.17 Mass attenuation coefficient for tungsten (W) with $Z = 74$ and iron (Fe) with $Z = 26$ as a function of X-ray photon energy. For tungsten its K-absorption edge is at 69.53 keV, L-absorption edge is at 12.11 keV and M-absorption edge is at 2.27 keV; for iron its K-absorption edge is at 7.11 keV. The appearance of absorption edges is due to the increased probability of photoelectric effect, when the energy of the incident X-ray just exceeds the binding energy of the inner shell electrons. Graphs produced using data from NIST website [107]. (Mass attenuation coefficient is explained in section 2.3.6)

In addition, according to equation (42) the probability of the photoelectric effect increases for elements with higher Z . The product of the photoelectric effect is a photoelectron, characteristic X-ray photon and a positive ion.

Compton scattering

Another form of X-ray interaction with matter is known as Compton scattering. Here, a high energy X-ray photon of energy E_0 , strikes an outer shell free¹⁶ electron, ejecting it from its orbit. The photon is deflected in a new direction, losing some of its energy, and continuing its travel with energy E' . The energy of the incident X-ray photon E_0 is equal to the sum of the energy of the scattered X-ray photon E' and the kinetic energy of the ejected electron E_e (figure 2.18). The relationship between the fractional energy loss and the scattering angle θ is given by Klein-Nishina equation

¹⁶ A free electron, is an electron with binding energy significantly less than the energy of the incident X-ray photon. For X-ray photons with energies in the range from 50 keV to 450 keV only the outer shell electrons are considered free for elements with high atomic number Z [91].

$$\frac{E'}{E_0} = \frac{1}{1 + \alpha(1 - \cos(\theta))}, \quad (43)$$

where $\alpha = E_0/(m_0 c^2)$, and $m_0 c^2$ is the rest mass of the electron equal to 511 keV [108]. This formula shows that the final energy E' of the scattered X-ray photon depends on its initial energy E_0 and the scattering angle θ .

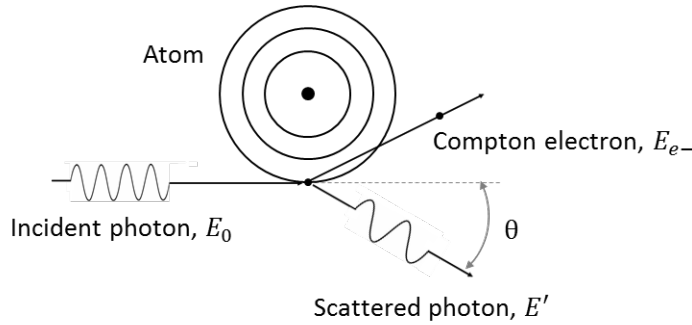


Figure 2.18 Schematic representation of Compton scattering.

The amount of energy retained by an X-ray photon after it undergoes Compton scattering is presented in table 2.1.

Table 2.1 The dependence of Compton scattered X-ray photons energy on their initial energy and different scattering angles. Energies calculated using formula Klein-Nishina equation.

| E_0 (keV) | E' (keV) | | | |
|-------------|---------------------|---------------------|---------------------|----------------------|
| | $\theta = 30^\circ$ | $\theta = 60^\circ$ | $\theta = 90^\circ$ | $\theta = 180^\circ$ |
| 50 | 49.4 | 47.7 | 45.5 | 41.8 |
| 75 | 73.6 | 69.9 | 65.4 | 58.0 |
| 100 | 97.5 | 91.1 | 83.6 | 71.9 |
| 150 | 144.3 | 130.8 | 116.0 | 94.5 |
| 200 | 190.0 | 167.3 | 143.7 | 112.2 |
| 225 | 212.5 | 184.4 | 156.2 | 119.6 |
| 450 | 402.5 | 312.4 | 239.3 | 163.0 |

Table 2.1 demonstrates that for X-ray photon energies of up to 450 keV (a typical range of energies for industrial XCT systems), X-ray photons which are scattered at small angles

retain most of their original energy. These scattered photons represent a problem for XCT imaging, as they can easily reach the detector, contributing to image noise and degrading the image quality.

Compton scattering depends on the probability of an incident X-ray photon interacting with a free electron, which can be estimated by the number of electrons per cm^3 , the product of material density and the number of electrons per gram. Since the number of electrons per gram decreases only slightly with increasing atomic number Z , it can be said that the probability of Compton scattering per unit volume is approximately proportional to the material density, and the probability per unit mass is practically independent of material atomic number Z [1], [109]. In the commercial energy range, Compton scatter is practically independent of the incident X-ray photon energy.

Rayleigh scattering

Rayleigh scattering occurs when an incident X-ray photon of a given frequency λ , causes all of the electrons in the scattering atom to oscillate in phase. The electron cloud, in turn, immediately radiates this energy, emitting a photon of the same frequency λ but in a slightly different direction. Unlike with photoelectric effect and Compton scattering, no electrons are ejected during Rayleigh scattering; therefore no ionisation takes place. In the commercial energy range photoelectric effect and Compton scatter are two dominant mechanisms by which X-rays interact with matter. Rayleigh scattering is typically small but not negligible [36].

Pair production

During pair production, the incident X-ray photon interacts with the atomic nucleus producing an electron-positron pair. This process can only take place for energies above 1.02 MeV, and therefore is not applicable for most commercial XCT systems.

2.3.6 Attenuation of X-rays

Attenuation is defined as the removal of X-rays from the X-ray beam either by absorption or scattering events described in the previous section, as the beam traverses matter [1].

Linear attenuation coefficient

Say, a monoenergetic X-ray beam of N_{in} number of photons is incident upon a piece of material of incremental thickness dx , with a probability of interaction μ , then the reduction of photons from the beam dN is given by

$$dN = -\mu N dx. \quad (44)$$

where $dN = N_{out} - N_{in}$, and N_{out} is the expected number of photons that pass through the material; μ is also called a linear attenuation coefficient with units cm^{-1} . Rearranging equation (44) and integrating across the entire thickness of the piece of material t gives,

$$\int_0^t \frac{dN}{N} = \mu \int_0^t dx. \quad (45)$$

Then

$$\ln(N(t)) - \ln(N(0)) = -\mu x. \quad (46)$$

Since $N(t) = N_{out}$ and $N(0) = N_{in}$, equation (46) becomes

$$\ln(N_{out}) - \ln(N_{in}) = -\mu x. \quad (47)$$

Applying the exponential function to each side and rearranging gives

$$N_{out} = N_{in} e^{-\mu x}. \quad (48)$$

Equation (48) is known as the Beer-Lambert law; it shows that if a monoenergetic X-ray beam passes through a uniform material of thickness x with linear attenuation coefficient μ , there is an exponential relationship between the number of incident photons N_{in} and the number of transmitted photons N_{out} [110].

Attenuation of X-rays is the result of different types of interactions, therefore, the linear attenuation coefficient μ is the sum of individual linear attenuation coefficients for each type of interaction, i.e.

$$\mu = \tau + \sigma + \sigma_r + \gamma, \quad (49)$$

where τ , σ , σ_r and γ are linear attenuation coefficients for photoelectric effect, Compton scattering, Ryleigh scattering and pair production, respectively.

Mass attenuation coefficient

The linear attenuation coefficient μ depends linearly on the density of material ρ . In order to define the attenuation of materials independently of their physical state, the linear attenuation coefficient is normalised by the material density. This is known as the mass attenuation coefficient μ/ρ with units of cm^2g^{-1} . Just as with the linear attenuation coefficient, the total mass attenuation coefficient is the sum of individual mass attenuation coefficients:

$$\frac{\mu}{\rho} = \frac{\tau}{\rho} + \frac{\sigma}{\rho} + \frac{\sigma_r}{\rho} + \frac{\gamma}{\rho}, \quad (50)$$

The contributions of the four attenuation processes to the total attenuation of X-ray in matter depends on the incident X-ray photon energy E_0 , material atomic number Z and material density ρ and is summarised below in table 2.2. As an example, figure 2.19 demonstrates how different attenuation processes contribute to the overall attenuation in lead (Pb).

Table 2.2 Attenuation coefficients dependencies [108].

| Attenuation coefficient | Energy, E_0 | Atomic number, Z | Density, ρ |
|-------------------------|---------------|--------------------|-----------------|
| τ/ρ | $1/E^3$ | Z^4 | - |
| τ | $1/E^3$ | Z^3 | ρ |
| σ | independent* | independent* | ρ |
| σ_r | $1/E^{1.2}$ | - | ρ |

*independent in the region of the X-ray energies used in commercial XCT

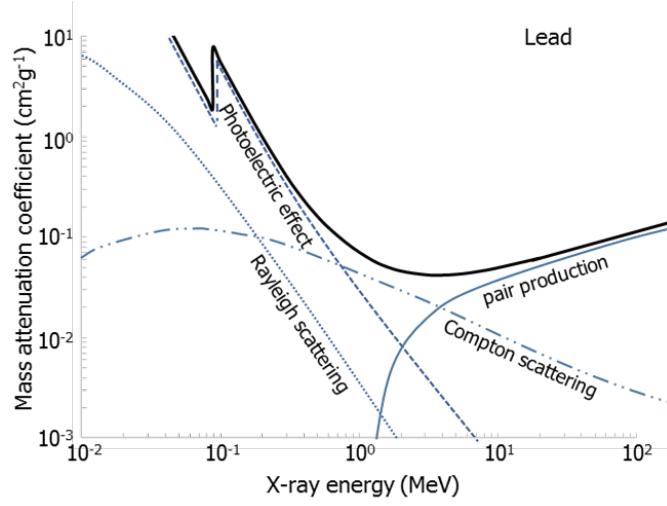


Figure 2.19 Distribution of different types of attenuation effects for lead (Pb), as a function incident X-ray photon energy. Here, pair production dominated for energies above 10 MeV, Compton scattering is dominant at around 1 MeV and photoelectric effect at energies used in commercial XCT systems. Adapted from [92].

Beam-hardening

In commercial XCT systems the X-ray beam is polychromatic in nature, i.e. it contains a spectrum of energies up to the maximum energy, determined by the accelerating tube voltage. For most materials, as the polychromatic X-ray beam passes through material, low energy X-rays are preferentially removed, resulting in the shift of the spectrum to higher effective energies. This increase in the effective energy of the beam as it traverses matter is called beam-hardening. The effective energy of a polychromatic X-ray beam is defined as the energy of the monochromatic beam that is attenuated at the same rate as the polychromatic beam in question [104]. The Beer-Lambert law for a polychromatic X-ray beam with inhomogeneous material becomes

$$N_{out} = \int_E N_{in}(E) e^{\int_t \mu(x,E) dx} dE, \quad (51)$$

where N_{out} is the total number of transmitted X-ray photons, $N_{in}(E)$ is the number of incident X-ray photons of different energies and $\mu(x, E)$ is the linear attenuation coefficient of the material at different energies. The effects of beam-hardening on the reconstructed images are discussed in section 2.4.8)

2.4 Background to X-ray computed tomography

A brief introduction to the basic principles of XCT and XCT system's main constituent parts are presented in this section.

2.4.1 Basic principles of XCT

X-ray computed tomography is a non-destructive X-ray imaging technique, which allows the visualisation of the external and internal structures of a solid object, as well as to obtain qualitative and quantitative information about an object's properties and 3-D geometries. A commercial XCT system comprises several main parts: the X-ray tube (often called the X-ray gun), the mechanical system with a rotary table, the detector and data processing computer. XCT systems are frequently called CT scanners; in this thesis these terms are used interchangeably. Basic principles of XCT are as follows: the X-rays leave the X-ray tube and impinge on an object, as it is rotated on the rotation stage¹⁷. The X-rays propagate through the object and are attenuated due to the absorption and scattering events. X-rays that are transmitted through the object, interact with the detector and form 2-D grey images of the object from multiple orientations. A 2-D grey image is a quantitative map of the linear attenuation coefficient, μ , at each point in the plane [36]. The collection of images of the object from different orientations is called an 'image stack'. The process of acquiring a complete image stack is known as a CT scan of the object. A subsequent mathematical reconstruction of the image stack allows the construction of a 3-D model of the object, which can undergo further measurement tasks. A schematic representation of the XCT process in an industrial cone-beam XCT system is shown in figure 2.20.

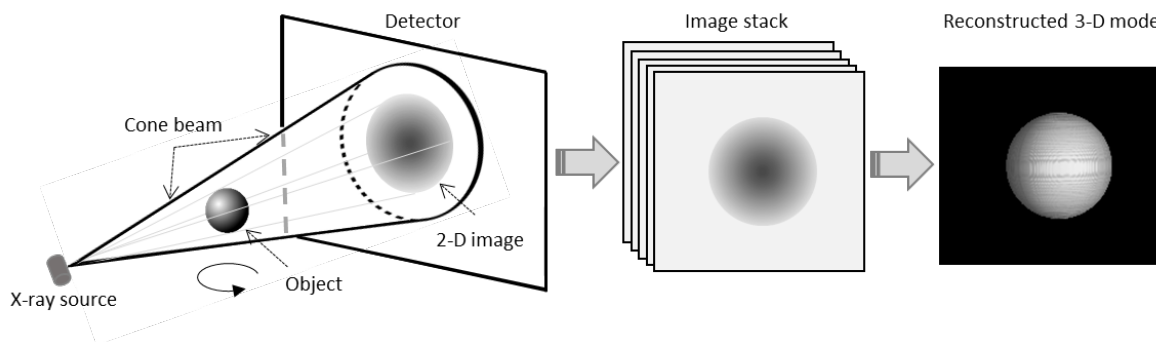


Figure 2.20 Schematic representation of the XCT process in an industrial cone-beam XCT system.

¹⁷ In medical XCT systems, the object, i.e. the patient, remains stationary and the X-ray tube and the detector rotate around the patient (see section 2.4.2).

2.4.2 Scanning configurations

Since their introduction to the medical field in 1971, XCT systems have undergone a number of design changes and are often divided into ‘generations’ [2]:

- First generation XCT systems employed a pencil-like X-ray beam with a single detector, where the beam and the detector had a ‘translate-rotate’ motion;
- Second generation systems employed a narrow fan-like X-ray beam (‘fan-beam’) with a detector array of up to 30 detectors. The motion of the X-ray beam and the detector was the same as with the first generation but in larger steps.
- In third generation systems the span of the X-ray fan-beam was increased to cover the entire object to be imaged. The detector array was arranged in an arc with up to 288 detectors, with detector centre aligned with the centre of the X-ray beam. With such system design, the X-ray tube and the detector were continuously rotating around the object during the scan, eliminating the need for translatory motion.
- Fourth generation scanners also employed the X-ray fan-beam but the detector array was arranged in a ring-like manner, completely surrounding the object to be imaged, with only the X-ray tube rotating during the scan.

In the 1990s, third generation CT scanners with multi-row detector systems were introduced to the market. These systems became the most popular in the medical field to date, and are known as ‘standard scanner configuration’ systems. A number of new XCT technologies adapted to third and fourth generation scanners have subsequently been developed, e.g. cone-beam CT scanners with flat-panel detectors, dual-source CT scanner, dual-energy CT scanner and spiral CT [2]. Fan-beam XCT systems were the first to be used in material analysis and non-destructive testing (NDT). At present, most industrial XCT systems employ a cone-beam¹⁸ X-ray source configuration (figure 2.20) [5].

2.4.3 X-ray tube

Types of cathodes and anodes

The basic principles of X-ray production inside the X-ray tubes are discussed in the previous chapter. The exact design of an X-ray tube and its constituent parts may vary, depending on their application. For example, in most X-ray tubes for medical diagnostic imaging, the

¹⁸ A cone-beam X-ray source, as its name suggests, is a cone-shaped X-ray beam, which allows to obtain 2-D images of an object (figure 2.19).

filament is a tungsten wire tightly wound in a helix of several mm in length. Some cathodes hold two filaments of different length: the short filament is 0.1 mm to 1 mm long, for generating tube current of below 300 mA and the long filament is 0.3 mm to 2 mm long, for generating tube current of up to 7 000 mA [1]. Such tubes can generate focal spots of up to several mm in size. On the other hand, micro-focus XCT systems use a v-shape tungsten wire filament, generating focal spots from 3 μm to 1 mm in size. Most XCT systems, which are used in the field of dimensional metrology, are micro-focus XCT systems.

There are a number of different targets that are used in modern X-ray tubes. Targets can be stationary or rotating. A rotating target has a shape of a disk, which can be rotated at a speed of up to 10 000 revolutions per minute; it is the most widely used target in diagnostic XCT systems, due to its greater heat capacity and higher X-ray intensity output [1]. Stationary targets can be solid-metal or liquid-metal jet. Depending on their application, solid metal targets are made of tungsten ($Z = 74$), tungsten–rhenium ($Z = 75$) alloy, rhodium ($Z = 45$), molybdenum ($Z = 42$), etc. In order to avoid solid-metal target damage, the temperature of the surface of the target must be kept below its melting point; therefore, X-ray tubes with solid-metal targets operate at comparatively low powers. In liquid-metal jet targets, solid metal is replaced by a liquid metal anode, increasing the maximum operating tube power, since the need for operating the tube at temperatures below the melting point is removed [89].

Solid-metal targets can be of transmission and reflection type. In transmission targets, the incident electron beam impinges on a thin layer of metal (mainly tungsten) of 1 μm to 10 μm thickness, emitting X-rays through the target in the same direction as the electron beam. The main advantages of the transmission target are that it allows 1) generation of a small round focal spot of below 1 μm and 2) production of images at very high magnifications, since the object to be imaged can be placed within 0.5 mm from the X-ray source. However, due to the target being only a thin sheet of metal, transmission X-ray tubes are limited in their operating power. In reflection targets, the electron beam is incident on a thick metal target, generating the X-ray beam, which is reflected ‘away’ from the target. The angle of reflection depends on the target geometry and the angle between the electron beam and the target. Reflection targets are more widely used, since they can withstand higher power electron beams before the target overheats and is damaged. Unfortunately, due to the reflection target design, it is not possible to place the object to be imaged closer than approximately 5.5 mm from the X-ray source, thus minimising the magnifying capabilities of the XCT system. Most modern XCT systems with stationary targets employ a variety of cooling mechanisms to dissipate the heat generated during production of X-rays.

Filtration

As mentioned previously, filtration is the removal of X-rays as the beam passes through material. Filtration includes the inherent filtration of the X-ray tube and added filtration. The inherent filtration is due to the geometry of the target, the internal tube design and the type of the aperture window where X-ray emerge. For many X-ray tubes this aperture window is made of a thin sheet of beryllium ($Z = 4$), to allow the transmission of low energy X-rays. Another material often used as an aperture window is aluminium ($Z = 13$), which attenuates practically all X-ray below about 15 keV [1]. Added filtration refers to sheets of metal such as aluminium, copper, lead, etc., placed in the path of the X-ray beam near the aperture window. The purpose of these filters is to absorb lower energy X-ray photons, thus increasing the penetrability of the X-ray beam by shifting its effective energy to higher values (figure 2.21). Thin sheets of metal can also be placed between the object and the detector, with the purpose of filtering out soft scattered radiation, thus improving the image quality. Lead, copper and steel are some of the suitable filtering materials.

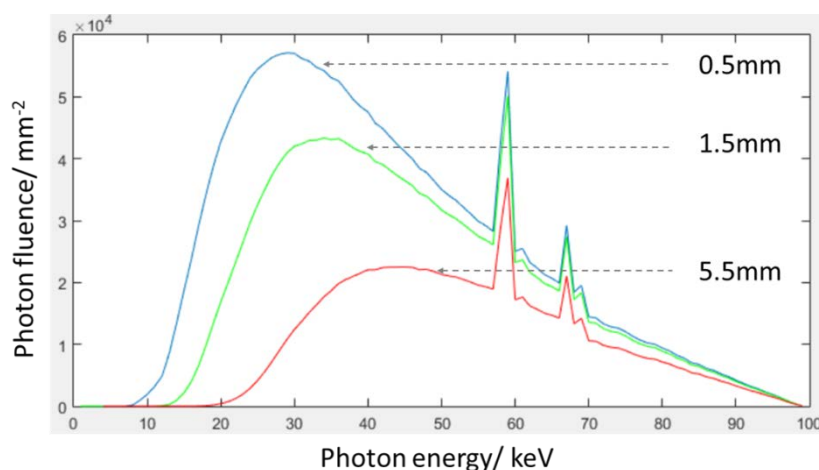


Figure 2.21 A computer simulation of the spectra for tungsten anode with maximum X-ray photon energy set to 100 keV when using different filter thickness. Spectra were simulated 1) using inherent 0.5 mm Al filtration (blue), 2) with the additional 1 mm Al filter (green) and 3) additional 5 mm Al filter (red). The effective energies of the X-ray beam simulated with 0.5 mm, 1.5 mm and 5.5 mm Al filters were calculated to be around 34 keV, 41 keV and 51 keV, respectively.¹⁹

¹⁹ X-ray spectra were simulated using a Matlab code developed by Rong Su (University of Nottingham). The effective energies were calculated using SpekCalc software [150].

Line focus principle

The need for a larger focal spot to allow greater heat loading on one hand, and a smaller focal spot to produce sharper images on the other, is addressed by the line focus principle. The line focus principle is the 'conversion' of the actual focal spot into the effective focal spot (figure 2.22). The actual focal spot is the area on the target that is struck by the electron beam, the size of which is determined by the geometry of the filament, the X-ray tube voltage and current settings, the Wehnelt cylinder and the magnetic lens. The projected focal spot is referred to as the effective focal spot. Geometrically, the size of the actual focal spot and the effective focal spot are related by

$$\text{Effective focal spot length} = \text{Actual focal spot length} \times \sin(\theta), \quad (52)$$

where $\sin(\theta)$ is the anode angle, which differs for different X-ray tube designs.

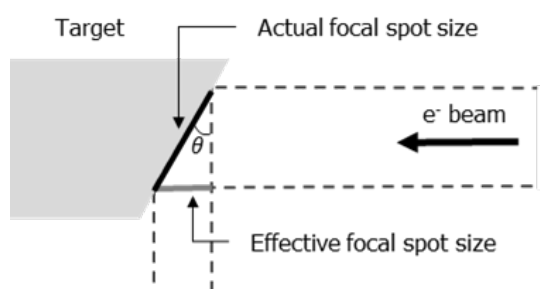


Figure 2.22 Schematic representation of the line focus principle.

Heel effect

As the electron beam strikes the target and X-rays are produced, some X-rays have to travel further through the target before escaping to the surface. The result is that the intensity of the X-ray beam is not uniform throughout the beam diameter: it has higher intensity on the 'cathode side' and lower intensity on the 'target side' of the beam (figure 2.23) [1]. This is known as the heel effect. The exact characteristics of the heel effect are the property of a particular X-ray tube design, i.e. the angle between the incident electron beam and the target and the geometry of the target.

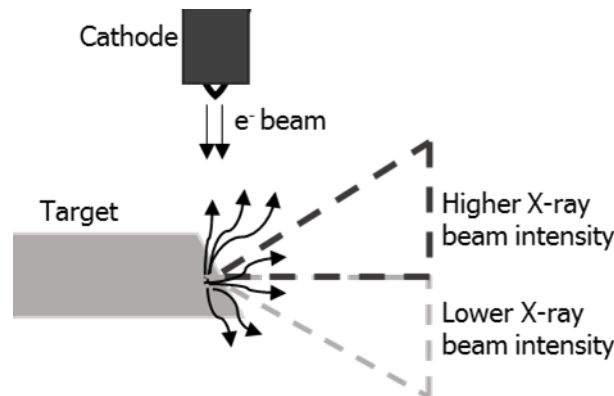


Figure 2.23 Schematic representation of the heel effect. The intensity of the X-ray beam is higher on the ‘cathode side’ and lower on the ‘target side’ of the beam.

Off-focal radiation

Off-focal radiation is produced inside the X-ray tube, when high energy electrons interact with metal surfaces other than the focal track of the target, e.g. other areas of the target, the tube housing and aluminium or beryllium aperture [91]. Most of these interactions are due to backscattered electrons introduced in section 2.3.4. Off-focal radiation causes geometric blurring in the image, reduces image contrast and increases random noise [1]. The exact distribution of off-focal radiation depends on the number and the direction of motion of backscattered electrons, distance from target to the tube housing, the exact geometry and material of the housing, as well as the overall tube design. In some X-ray tubes the off-focal radiation that reaches the detector constitutes more than 10 % of the total signal, which is not insignificant for an XCT system’s performance [89], [111]. There are a number of methods to minimise the effects of off-focal radiation which depend on the design and application of the X-ray tube. For example, some tubes have housing made of low Z metals, therefore when backscattered electrons strike the housing, only low energy X-rays are produced [91]. These X-rays do not have enough energy to reach the detector and do not interfere with the process of image acquisition. In other X-ray tube designs, a small lead collimator aperture²⁰ is placed near the tube aperture window; this helps to intercept X-rays which produced away from the focal spot [1]. Some have applied software methods for correcting the off-focal radiation effects [89], [111]. The subject of off-focal radiation is discussed further in chapter 4.

²⁰ Collimator is a device which helps to adjust the shape and size of the X-ray beam emerging from the X-ray tube [1].

2.4.4 Detector types

The purpose of the detector is to measure the transmission of X-rays through the object along different ray paths by transforming the incident X-ray intensity into an electrical signal, which is amplified and converted into a digital form [40]. Most modern industrial XCT systems employ the use of either flat panel digital X-ray detectors, consisting of 2D arrays of individual detector elements (pixels), or straight or curved line digital X-ray detectors, consisting of a 1D array of pixels [61]. The flat panel digital detectors can be of two types: direct-conversion detectors and indirect-conversion detectors for converting X-rays into an electric charge (figure 2.24). In both detector types thin-film transistor (TFT) arrays are used as active electronic elements. TFT arrays are typically deposited onto a glass substrate, starting with the readout electronics at the lowest level, followed by electric charge collector arrays, then X-ray absorption materials (depending on detector type) are deposited to form the top layer of the TFT arrays. The whole assembly is fitted with protective enclosure and connected to the computer [112]. TFT arrays are divided into individual pixels, each having a charge collection electrode, capacitor for storing electric charges and a switching transistor for readout process.

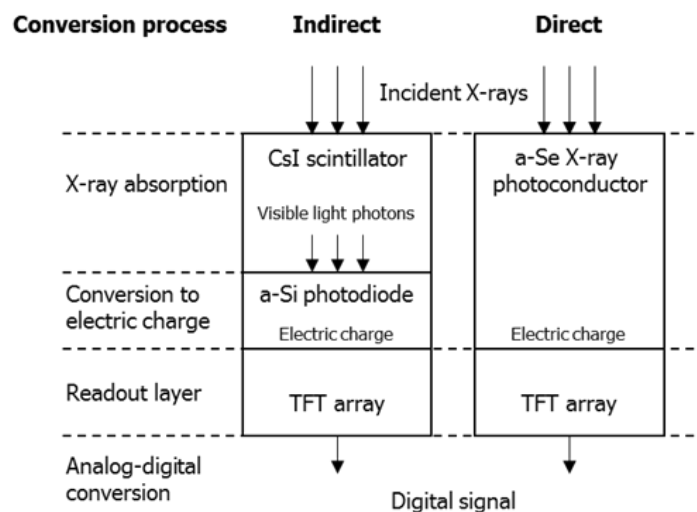


Figure 2.24 Schematic representation of direct-conversion and indirect-conversion digital flat panel detectors. The operation of both detector types is discussed in the text.

Direct-conversion detectors use amorphous selenium-coated TFT array to capture and convert X-rays directly into electric charge. Incident X-rays generate electron-hole pairs in the selenium layer proportional to the X-ray intensity. The electrons or holes in each pixel drift towards an electrode, under a bias voltage applied across the detector structure, and are temporarily stored in a capacitor. During the readout process, the charge in each pixel is

amplified, converted to a proportional voltage, the voltage level is then digitised, resulting in a grey value for each pixel in a TFT matrix [1]. Indirect-conversion detectors use a two-step process for X-ray detection. During the first step, the incident X-rays are captured by a scintillator such as cesium iodide (CsI), often doped with thallium (Tl), or gadolinium oxysulfide (GOS), converting them into visible light photons. (The visible light is proportional to the X-ray intensity). CsI is often a preferred scintillator material for two reasons. Firstly, CsI has a needle-like crystal structure, compared to GOS with a grain-like crystal structure. The needle-like structure allows light photons to be channelled directly to the photodiode layer, thus reducing the spread of light in the phosphor layer and improving spatial resolution. Secondly, a large proportion of a grain-like scintillator comprises binding material, which reduces phosphor packing density, making it less efficient in absorbing X-rays [113]. During the second step, the light photons are detected and converted into electric charge by an array of amorphous silicon (a-Si) thin-film diodes (TFDs), often called photodiodes. As with the direct-conversion detector, within each pixel the electric charge is captured and stored in a capacitor, then amplified, digitised and transferred to the computer during the readout process using the TFT arrays. (Some systems use charge-coupled devices (CCDs) as an alternative light collection array and readout method [112]).

Direct-conversion digital detectors have superior spatial resolution capability compared to indirect-conversion digital detectors, due to the absence of the scintillator layer and the spreading of light within it. However, because of the relatively low atomic number of a-Se ($Z = 34$), its absorption efficiency at higher X-ray energies is low; therefore, most industrial XCT systems employ indirect-conversion digital detectors [114]. At present, standard commercial 2D detectors are available for energy ranges from 20 kV to 15 MV. Typical pixel sizes are 150 μm , 200 μm , 250 μm or 400 μm , with detector matrix comprising 1024×1024 pixels, 2048×2048 pixels, 2880×2880 pixels or 4096×4096 pixels [115]. For inspection of objects made from high density materials, such as metal alloy turbine blades and casted parts, 2D flat panel detectors are often replaced by 1D line detectors with indirect-conversion technology. (X-ray fan-beam geometry is used with 1D line detectors).

2.4.5 Mechanical system

As mentioned previously, in industrial XCT systems the X-ray tube and the detector usually have a fixed position, whilst the object is rotated on the rotation stage between the X-ray tube and the detector (with or without vertical translational motion for a 1D detector or a 2D detector, respectively). The mechanical part of the XCT system usually consists of the following (figure 2.25):

- the rotation stage, for a stepwise or continuous rotation of the object during image acquisition;
- a horizontal translation axis for moving the rotation stage between the X-ray source and the detector for adjusting the object's magnification (often referred to as z-axis or magnification-axis);
- horizontal and vertical translation axes (referred to as x-axis and y-axis), for flexible positioning of the object on the rotation stage within the system's scanning volume.

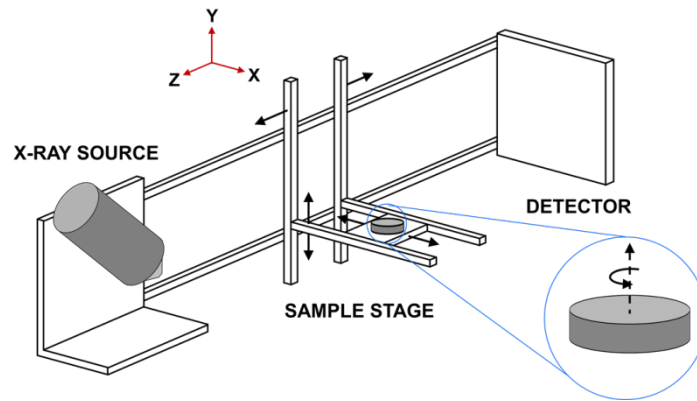


Figure 2.25 Schematic representation of a typical mechanical system in industrial XCT system.

Precision, repeatability and stability of magnification, horizontal, vertical and rotational axes are essential in achieving accurate reconstruction and, subsequently, performing accurate measurements of scanned object [3], [40].

2.4.6 Reconstruction

Radon transform

Once a scan of an object is completed and the image stack is acquired, the process of reconstruction takes place. The reconstruction algorithms can be divided into two classes: analytical, based on the Fourier slice theorem and iterative²¹, based on solving systems of linear equations [77], [110]. The mathematical foundation for the XCT image reconstruction was laid by Radon in 1917, who showed that if the set of line integrals of a function, which is finite over some region of interest and zero everywhere else, is known for all ray paths through the region, then the value of the function over that region can be uniquely determined [34], [116]. A line integral represents the integral of some parameter of the object along a line. In XCT this parameter is the total attenuation of the X-ray beam as it

²¹ Iterative algorithms are discussed elsewhere [110], [151].

propagates in a straight line through the object. For example, the object is represented by a 2D function $f(x, y)$ and each line integral by the (t, θ) parameters [110]. In figure 2.26 the equation for any line parallel to line L in its normal form is given by

$$x \cos(\theta) + y \sin(\theta) = t. \quad (53)$$

The line integral $P(t, \theta)$ is

$$P(t, \theta) = \int_{\text{line}(t, \theta)} f(x, y) ds. \quad (54)$$

Using Dirac delta function²², this can be rewritten as

$$P(t, \vartheta) = \iint_{-\infty}^{+\infty} f(x, y) \delta(x \cos(\theta) + y \sin(\theta) - t) dx dy. \quad (55)$$

The function $P(t, \vartheta)$ is known as the Radon transform of the function $f(x, y)$ [110].

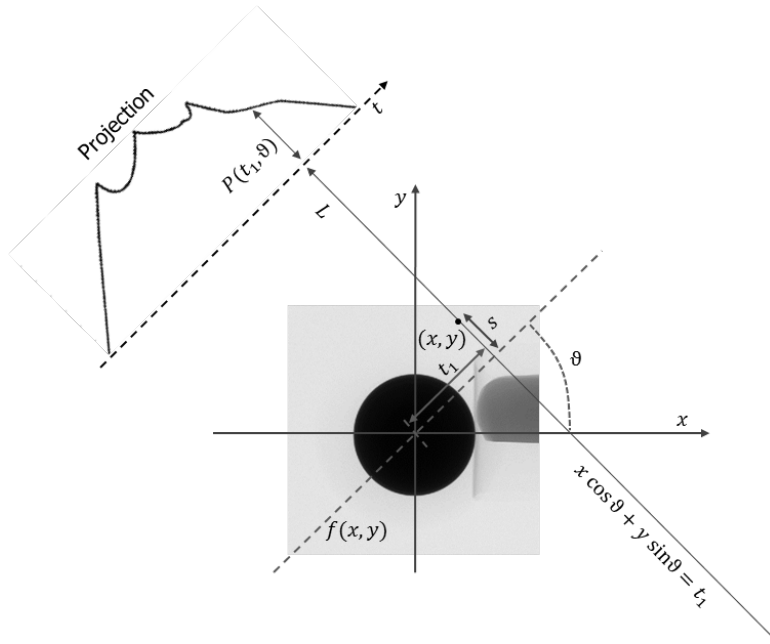


Figure 2.26 Schematic representation of the object $f(x, y)$ and a line integral $P(t_1, \vartheta)$. A projection is formed by combining a set of such line integrals [110].

²² In mathematics, the Dirac delta function δ , is a generalised function defined by the properties [92]:

$$\delta(x) = \begin{cases} 0 & \text{for } x \neq 0 \\ \infty & \text{for } x = 0 \end{cases} \text{ and } \int_{-\infty}^{\infty} \delta(x) dx = 1.$$

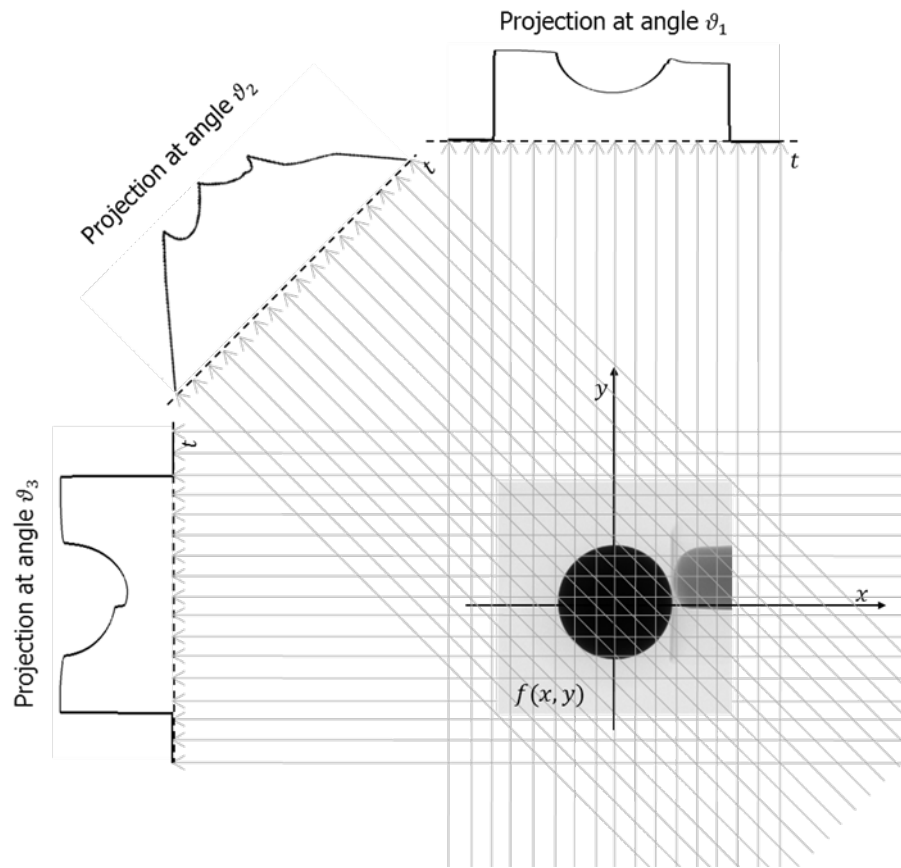


Figure 2.27 Schematic representation of parallel projections taken at angles ϑ_1 , ϑ_2 and ϑ_3 .

A projection is formed by combining a set of such line integrals (figure 2.27). Projection must be collected at all angles ϑ . The objective of the process, therefore, is to reconstruct the function $f(x, y)$ from the set of acquired projections.

Fourier slice theorem

The theory that governs XCT reconstruction is known as the Fourier slice theorem or the central slice theorem [77]. The Fourier slice theorem states that the one-dimensional Fourier transform of a parallel projection of an object $f(x, y)$ obtained at angle θ , is equal to a slice of the two-dimensional Fourier transform of $f(x, y)$ taken at the same angle (figure 2.28) [110].

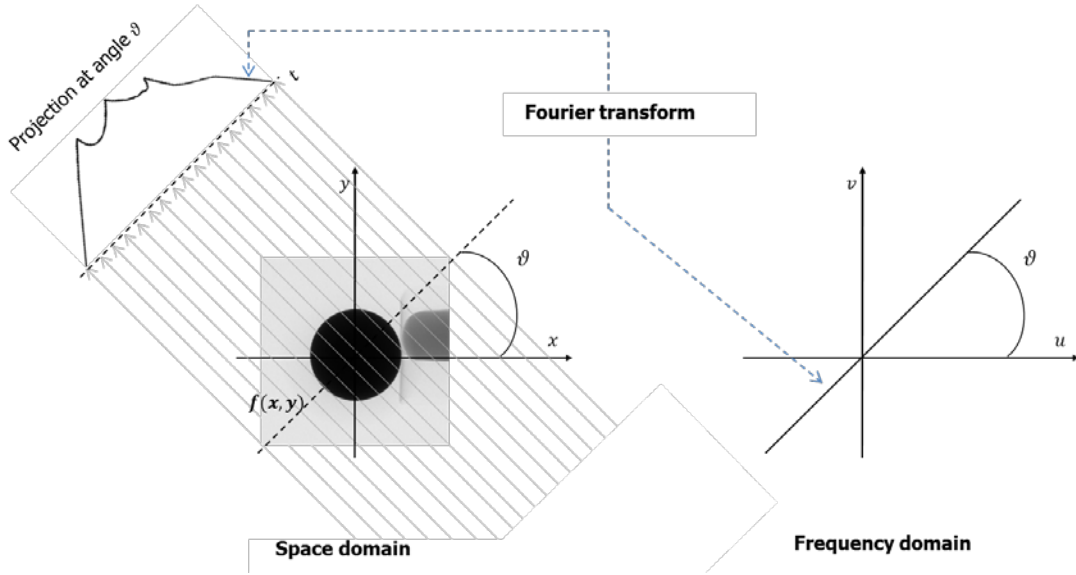


Figure 2.28 Schematic representation of the Fourier slice theorem.

The two-dimensional Fourier transform of a function $f(x, y)$ is defined as

$$F(u, v) = \iint_{-\infty}^{\infty} f(x, y) e^{-j2\pi(ux+vy)} dx dy. \quad (56)$$

In the same way, the Fourier transform of a projection at angle θ , $P(t, \theta)$ over variable t is denoted as $S(w, \theta)$:

$$S(w, \theta) = \int_{-\infty}^{\infty} P(t, \theta) e^{-j2\pi wt} dt. \quad (57)$$

Evaluated at $v = 0$,

$$F(u, 0) = \iint_{-\infty}^{\infty} f(x, y) e^{-j2\pi ux} dx dy. \quad (58)$$

Since there is no longer dependence on y , the above equation can be re-written as

$$F(u, 0) = \int_{-\infty}^{\infty} \left[\int_{-\infty}^{\infty} f(x, y) dy \right] e^{-j2\pi ux} dx. \quad (59)$$

For a parallel projection along the lines of constant x and $\theta = 0$,

$$P(x, 0) = \int_{-\infty}^{\infty} f(x, y) dy. \quad (60)$$

Substituting equation (60) into equation (59) gives

$$F(u, 0) = \int_{-\infty}^{\infty} P(x, 0) e^{-j2\pi ux} dx, \quad (61)$$

where the right-hand side of the equation represents a one-dimensional Fourier transform of the projection at $\theta = 0$; hence,

$$F(u, 0) = S(u, 0). \quad (62)$$

In other words, it has been shown that the Fourier transform of the parallel projection of the object $f(x, y)$ acquired at angle θ , is equal to a slice of the two-dimensional Fourier transform of the object at the same angle.

The Fourier slice theorem can be derived by considering the coordinate system (t, s) as the rotated version of the coordinate system (x, y) (figure 2.26),

$$\begin{bmatrix} t \\ s \end{bmatrix} = \begin{bmatrix} \cos(\theta) & \sin(\theta) \\ -\sin(\theta) & \cos(\theta) \end{bmatrix} \begin{bmatrix} x \\ y \end{bmatrix}. \quad (63)$$

In the (t, s) coordinate system, a projection along lines of constant t becomes

$$P(t, \theta) = \int_{-\infty}^{\infty} f(t, s) ds. \quad (64)$$

The Fourier transform for the above projection is given by equation (57). Substituting equation (64) into equation (57) gives

$$S(w, \theta) = \int_{-\infty}^{\infty} [f(t, s) ds] e^{-j2\pi wt} dt. \quad (65)$$

This result can be transformed into the (x, y) coordinate system by using equation (63)

$$S(w, \theta) = \iint_{-\infty}^{\infty} f(x, y) e^{-j2\pi w(x\cos(\theta) + y\sin(\theta))} dx dy. \quad (66)$$

It is evident that the right-hand side of equation (66) represents the two-dimensional Fourier transform at a spatial frequency of $(u = w\cos(\theta), v = w\sin(\theta))$. In other words,

$$S(w, \theta) = F(u, v) = F(w \cos(\theta), w \sin(\theta)). \quad (67)$$

Taking a sufficient number of projections at angles between 0 and π and using their Fourier transforms, the Fourier space of the object can be filled. Now, by taking the inverse two-dimensional Fourier transform, the object can be recovered in the space domain.

Although the Fourier slice theorem is theoretically straightforward, it has challenges in the actual implementation. Figure 2.29 demonstrates that the sampling pattern in Fourier space is in polar coordinates.

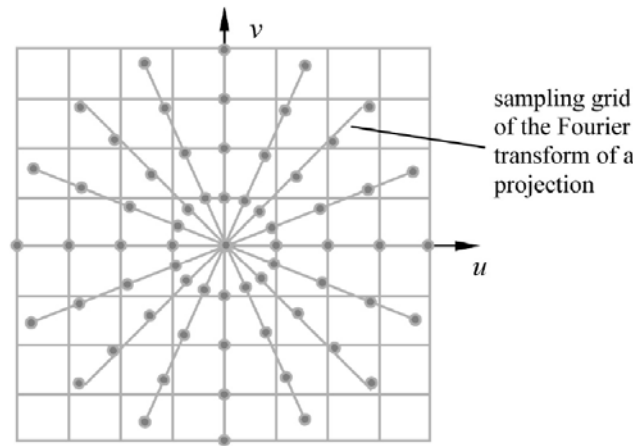


Figure 2.29 Sampling pattern in Fourier space based on the Fourier slice theorem [77].

In order to perform a 2D inverse Fourier transform, these samples must be interpolated to a Cartesian coordinate system. Interpolation in the frequency domain is not as straightforward as interpolation in real space. Error produced on a single sample in Fourier space affects the appearance of the entire image. Secondly, if there is a need to examine a small region within an object, it is difficult to use direct Fourier space reconstruction of that region, since the size of the inverse Fourier transform is inversely proportional to the size of the targeted region of interest. For a very small region of interest, the matrix size becomes very large, thus presenting problems with the application of the method.

Filtered backprojection

An alternative approach in implementing the Fourier slice theorem is known as filtered backprojection algorithm (FBP). Based on the Fourier slice theorem, the 2D Fourier transform of an object is obtained by putting together multiple 1D Fourier transforms (slices). Ideally, these slices would be shaped as a pie (figure 2.30a), but in reality they are more like strips (figure 2.30b). When such strips are summed, the centre region becomes

enhanced and the outer region is underrepresented. To approximate the desired pie-shape, each slice is multiplied by the weighting function (the weighting function has a lower intensity near the centre and a higher intensity near the edge) (figure 2.30c). If N projections are spaced evenly over 180° at a given frequency w , each wedge has a width of $2\pi|w|/N$. As a result, the summation of the weighted slices has the same ‘mass’ as the summation of the pie-shaped slices.

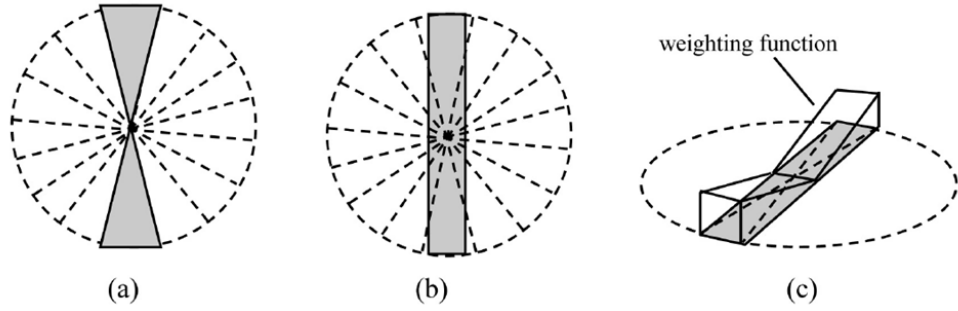


Figure 2.30 Illustration of the FBP: a) Ideal frequency data from one projection; b) actual frequency data from one projection; c) weighting function in the frequency domain to approximate ideal conditions [77].

The derivation of the FBP presented here follows [110] and is rather straightforward. An object $f(x, y)$ can be presented using its inverse Fourier transform as

$$f(x, y) = \iint_{-\infty}^{\infty} F(u, v) e^{j2\pi(ux+vy)} du dv. \quad (68)$$

Since the Fourier transform of each parallel projection falls on a polar coordinate system (w, θ) , the Cartesian coordinate system (u, v) needs to be replaced by making substitutions

$$u = w \cos(\theta) \quad (69)$$

$$v = w \sin(\theta) \quad (70)$$

$$du dv = w dw d\theta \quad (71)$$

The inverse Fourier transform of an object can now be written as

$$f(x, y) = \int_0^{2\pi} \int_{-\infty}^{\infty} F(w, \theta) e^{j2\pi w(x \cos(\theta) + y \sin(\theta))} w dw d\theta. \quad (72)$$

Chapter 2

The above integral can be split by considering two intervals from 0 to π and from π to 2π ,

$$f(x, y) = \int_0^{\pi} \int_{-\infty}^{\infty} F(w, \theta) e^{j2\pi w(x\cos(\theta) + y\sin(\theta))} w dw d\theta + \int_{\pi}^{2\pi} \int_{-\infty}^{\infty} F(w, \theta + 180^\circ) e^{j2\pi w(x\cos(\theta+180^\circ) + y\sin(\theta+180^\circ))} w dw d\theta. \quad (73)$$

Using the property $F(w, \theta + 180^\circ) = F(-w, \theta)$, equation (73) becomes

$$f(x, y) = \int_0^{\pi} \left[\int_{-\infty}^{\infty} F(w, \theta) |w| e^{j2\pi w t} dw \right] d\theta, \quad (74)$$

where

$$t = x\cos(\theta) + y\sin(\theta). \quad (75)$$

Substituting the Fourier transform of the projection at angle θ , $S(w, \theta)$, for the two-dimensional Fourier transform $F(w, \theta)$, gives

$$f(x, y) = \int_0^{\pi} \left[\int_{-\infty}^{\infty} S(w, \theta) |w| e^{j2\pi w t} dw \right] d\theta. \quad (76)$$

Using equation (75), this integral can then be re-written as

$$f(x, y) = \int_0^{\pi} Q(t, \theta) d\theta = \int_0^{\pi} Q(x\cos(\theta) + y\sin(\theta), \theta) d\theta, \quad (77)$$

where

$$Q(t, \theta) = \int_{-\infty}^{\infty} S(w, \theta) |w| e^{j2\pi w t} dw. \quad (78)$$

Equation (78) represents a filtering operation, where the frequency response of the filter is given by $|w|$ (often referred to as the Ramp filter); therefore, $Q(t, \theta)$ is called ‘filtered projection’. These filtered projections for different angles θ are then added together to form the estimate of $f(x, y)$.

Equation (76) can be re-written in terms of convolution for projections generated over 360 degrees:

$$f(x, y) = \frac{1}{2} \int_0^{2\pi} \int_{-\infty}^{\infty} P(t, \theta) h(x \cos(\theta) + y \sin(\theta) - t) dt d\theta, \quad (79)$$

where $h(\bullet)$ is the impulse response of the ramp filter [116].

When using a cone-beam source, the reconstruction takes into account the fact that voxels do not stay in the same horizontal projection plane while the part is rotated, hence the Feldkamp FBP algorithm (FDK) is applied [117]. The FDK algorithm is an extension of 2D fan-beam reconstruction algorithm for a circular scan in 3D space. Schematic representation of fan-beam and cone-beam circular geometries is shown in figure 2.31.

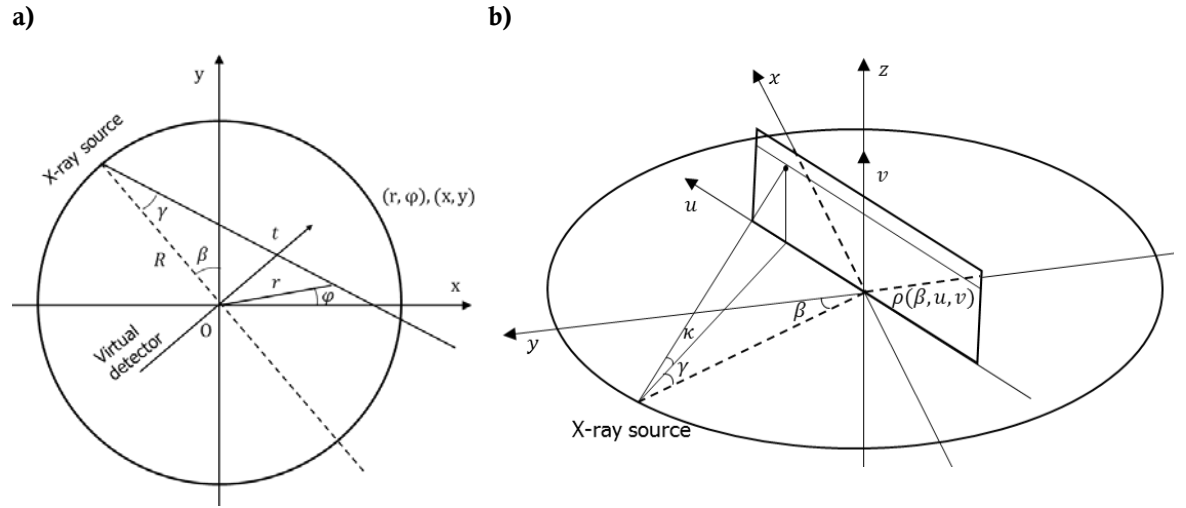


Figure 2.31 Schematic representation of a) fan-beam and b) cone-beam circular scan geometries (adapted from [116]).

For an equal-spaced fan-beam reconstruction algorithm it can be shown that

$$f(x, y) = \frac{1}{2} \int_0^{2\pi} \frac{R^2}{(R + x \sin \beta - y \cos \beta)^2} \int_{-\infty}^{\infty} g(t, \beta) \frac{R}{\sqrt{R^2 + t^2}} h(t' - t) dt d\beta, \quad (80)$$

where $g(t, \beta)$ denotes the equal-spaced fan-beam projection, R is the distance between the X-ray source and the iso-centre, t is the virtual detector and $t' = R \frac{y \sin \beta + x \cos \beta}{R + x \sin \beta - y \cos \beta}$ [116]. On closer examination of equation (80) it becomes apparent that the fan-beam algorithm requires the scaling of the projection prior to filtering and a weighted backprojection. The scaling factor $\frac{R}{\sqrt{R^2 + t^2}}$ is equal to $\cos(\gamma)$, where γ is the fan angle.

The cone-beam reconstruction algorithm can be written as

$$f(x, y, z) = \frac{1}{2} \int_0^{2\pi} \frac{R^2}{(R + x \sin \beta - y \cos \beta)^2} \int_{-\infty}^{\infty} \rho(\beta, u, v') \frac{R}{\sqrt{R^2 + u^2 + v'^2}} h(u' - u) du d\beta, \quad (81)$$

where $\rho(\beta, u, v')$ denotes the cone-beam projection, R is the distance between the X-ray source and the iso-centre, (u, v) is a virtual detector, placed on the axis of rotation, $v' = \frac{zR}{R + x \sin \beta - y \cos \beta}$ and $u' = R \frac{y \sin \beta + x \cos \beta}{R + x \sin \beta - y \cos \beta}$ [116]. For cone-beam reconstruction algorithm the scaling factor is

$$\frac{R}{\sqrt{R^2 + u^2 + v'^2}} = \frac{\sqrt{R^2 + u^2}}{\sqrt{R^2 + u^2 + v'^2}} \cdot \frac{R}{\sqrt{R^2 + u^2}} = \cos(\kappa) \cos(\gamma), \quad (82)$$

where γ is the fan angle and κ is the cone angle as shown in figure 2.31.

It is important to note that the FDK reconstruction algorithm is an approximate reconstruction algorithm with the exact reconstruction preserved a) on circular trajectory plane, b) for objects homogeneous along the z -axis, c) the longitudinal integral of the reconstruction is exact and d) the integral of the reconstruction is exact along a set of oblique lines [116]. The FDK algorithm performs reasonably well for cone angles below 10° [118]. The FDK algorithm is widely accepted by the industry as a standard reconstruction method for cone-beam XCT systems. However, this algorithm is sensitive to the misalignments of the source, rotation axis and the detector, requiring regular adjustment and adequate error correction [82].

2.4.7 Surface determination and dimensional measurement

Once the reconstruction process is completed and a 3D voxel model of a scanned object is obtained, the surface determination procedure is performed. The surface determination, also known as thresholding, converts 3D voxel data into 3D surface data [61]. The most common method is to determine the surface by setting a global thresholding value, where any voxel with a grey value less than the threshold is considered to be a background. This threshold value is calculated by using a histogram of the number of voxels vs voxel grey value. For example, for a single material object the histogram would depict two peaks, one for background and another for material; the mid-value between the two peaks is then taken as the threshold value (figure 2.32). This method is often called ISO-50 % [3]. Alternatively surface determination can be performed using local thresholding. Here, starting from the

global threshold value, the surface is identified by the local highest grey value gradient within a designated number of voxels.

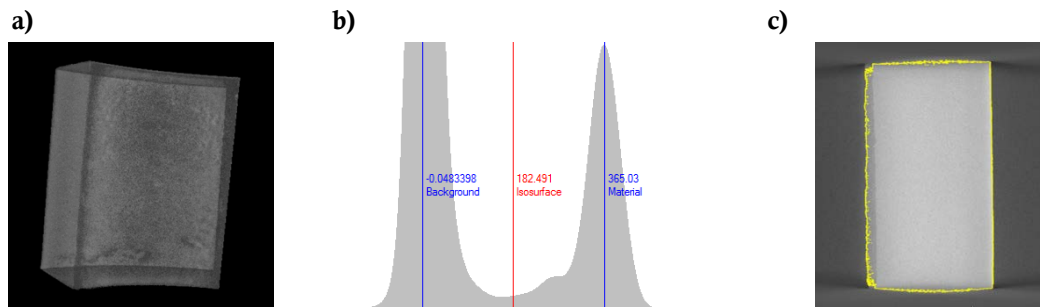


Figure 2.32 Surface determination procedure. Here a) is a reconstructed 3D model of a metal object, b) is the histogram of the number of voxels vs voxel grey value and c) is a 2D slice through the 3D model with identified surface voxels shown in yellow.

The edge detection generally results in a point cloud (i.e. a collection of points located at the interface between various materials). This point cloud is then generally turned into a geometrical surface model by topological association of neighbouring points [61]. The association is mainly achieved by generating a mesh model representative of the scanned object and different material regions within it. In order to perform dimensional analysis of the acquired data, an additional processing step is required: a surface model of an object (or regions within the object) is fitted with geometrical features, such as planes, spheres, cylinders, etc. This allows further calculation of the geometrical data, such as position, orientation, dimension, angle, form error, etc.

2.4.8 Artefacts

All XCT data and subsequently, its dimensional analysis are affected by the presence of artefacts. Artefacts are defined as the discrepancy between the reconstructed values in an image and the true attenuation coefficients of the object [77]. Given the complex nature of XCT systems, it is not surprising that artefacts have a number of different causes:

- Beam-hardening artefacts are the result of the discrepancy between the polychromatic nature of the X-ray beam used in XCT systems (see section 2.3.6) and the monochromatic nature of the X-ray beam assumed by the reconstruction algorithm. This results in errors estimating the attenuation coefficient of the material, leading to subsequent errors in surface determination and dimensional analysis. Beam-hardening artefacts (combined with scatter, see below) often manifest themselves as ‘cupping’, where flat surfaces appear barrel-shaped

and sharp edges appear rounded and ‘streaking’, where dark streaks between high density objects appear in images. A number of beam-hardening correction methods, such as the filtration of the X-ray beam using physical metal filters, the linearisation of the beam path, the dual-energy technique are used to improve image quality [77].

- Scatter artefacts. Due to the physical process of Compton scattering (described in section 2.3.5) many of the X-ray photons that reach the detector are not primary photons but scattered radiation. These scattered photons make the detected signals deviate from the true measurement of the X-ray intensities, contributing to cupping and streaking artefacts [77]. In addition, scattered radiation is characterised as low frequency background noise in projections, causing the decrease in signal-to-noise ratio and loss of sharpness in images [3]. Scatter correction methods such as beam-stop arrays, beam-hole arrays, anti-scatter grids or scatter-deconvolution techniques are often used to reduce the effects of Compton scatter [119]–[122].

- Other artefacts may include ring artefacts, caused by uncorrected faulty pixels, manifesting themselves as concentric rings centred around the axis of rotation ; noise artefacts, caused by quantum and electronic noise; sampling artefacts, caused by the discrete sampling of projections; Feldkamp errors due to increasing cone angles resulting in distortions of the geometric forms of scanned objects, etc. [2], [3], [77], [123].

A number of the artefacts described above are shown in figure 2.33.

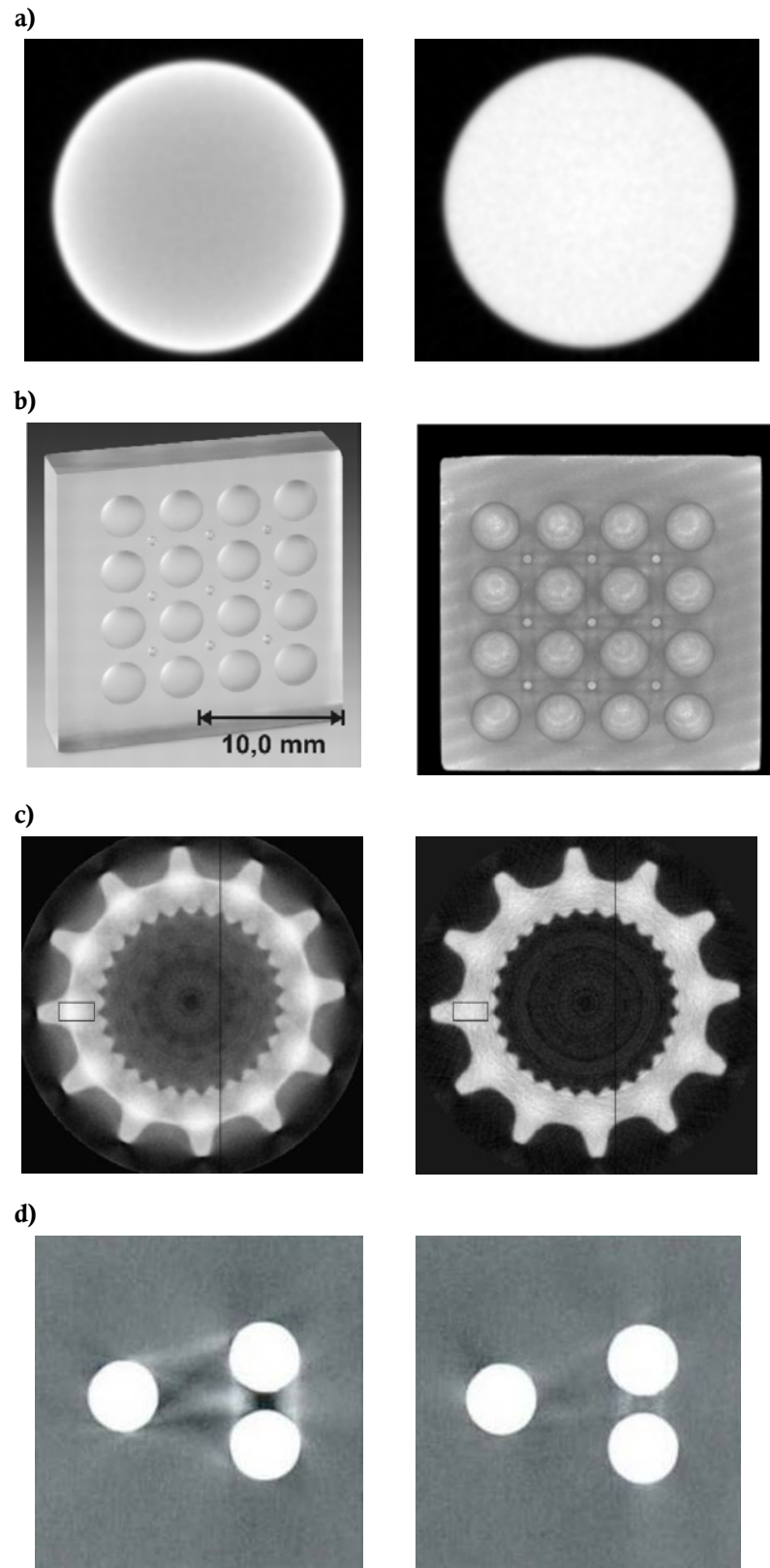


Figure 2.33 Examples of XCT artefacts: a) an aluminium sphere reconstructed without (left) and with (right) beam-hardening correction; b) Ball calotte plate reconstructed with dark streaks due to beam-hardening [124]; c) a metal part reconstructed without (left) and with (right) scatter correction [121]; d) three-rod phantom showing partial volume effect. The rods were intruded halfway into the X-ray beam with 7 mm collimator, with the original image (left) and corrected image (right) [77].

2.4.9 Summary of the overview

The overview of dimensional metrology, the X-ray physics and XCT technology presented in this thesis clearly demonstrate that XCT is a complex measuring technique with numerous factors which can potentially influence the measurement result. The influence factors (also known as ‘sources of error’) are often grouped according to the components of the XCT system they originate from, i.e. influence factors associated with the X-ray tube, the mechanical system, the detector, data processing, etc. [59], [61], [62], [125], [126].

As stated previously, the study described in this thesis focuses on sources of error associated with the X-ray tube. In the absence of any international or national standards for metrological application of XCT, a number of manufacturers and research organisations have adopted the VDI/VDE 2360 guidelines for performance verification of their XCT systems. VDI/VDE 2360 guidelines suggest a number of potential influence factors associated with the X-ray tube: voltage and current stability, location, size, shape and drift of the focal spot, inherent source filtration and beam divergence; however, no procedures for evaluating these influence factors are provided. No literature related to dimensional metrology which discusses the influence of off-focal radiation on measurement was identified. Based on the review of background, current standards for medical and non-destructive testing applications of XCT and additional metrology literature, the study of the X-ray tube parameters such as the positional stability of the focal spot, the focal spot size, the focal spot shape and off-focal radiation and their influence on dimensional measurement is presented in the following chapters.

Chapter 3: An investigation of the positional stability of the focal spot and its influence on dimensional measurement in cone-beam micro-focus XCT systems

3.1 Background to the experiments

The first property of the focal spot investigated in this work is its positional stability. Based on the background information given in chapter 2, the positional instability of the focal spot during an XCT scan can be attributed primarily to two factors. Firstly, the positional instability of the focal spot can be due to the electrical instabilities in steering coils and the focusing magnetic lens, as the electron beam propagates inside the tube, which can cause the focal spot to ‘wander’ on the surface of the target. Secondly, the great amount of heat produced during regular operation of the X-ray tube can significantly increase the tube temperature. This temperature increase causes a change in the geometry of the tube, e.g. elongation of the tube, expansion of the target, etc., thus modifying the position of the focal spot (figures 3.1 and 3.2). The positional instability of the focal spot leads to instability in the imaging geometry, thereby introducing errors in the image reconstruction process and affecting the accuracy of dimensional measurements [91].

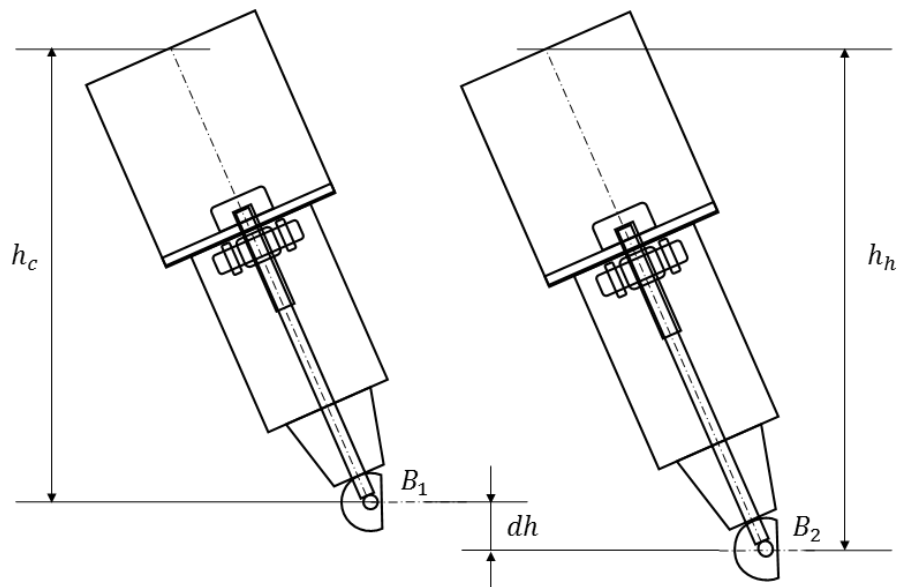


Figure 3.1 Schematic representation of the focal spot positional shift due to the elongation of the X-ray tube. Here, B_1 and B_2 are the central X-ray beams for the cold and hot tube, respectively; h_c and h_h are the height values for the cold and hot tube, respectively; and dh is the magnitude of the tube elongation due to heat.

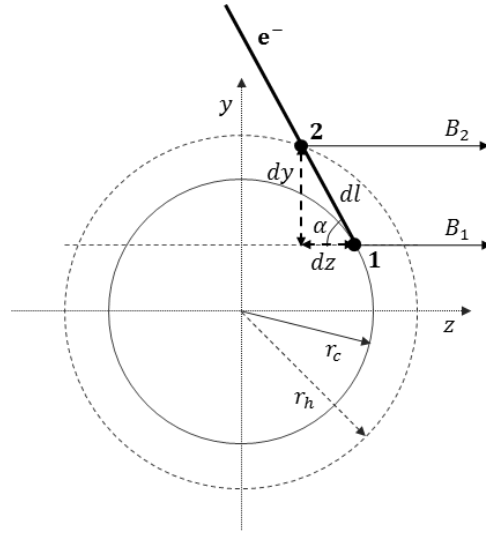


Figure 3.2 Schematic representation of the shift in the position of the focal spot due to thermal expansion of the target. Here, e^- is the incoming electron beam, interacting with the target at angle α ; 1 is the positions of the focal spot when the tube is cold and 2 is the position of the focal spot when the tube is hot; B_1 and B_2 are the central X-ray beams for the cold and hot tube, respectively; r_c and r_h are the radii of the cold and hot tube, respectively; dl is the change in the position of the focal spot, with dz and dy as dl components along the z -axis and the y -axis, respectively.

The influence of focal spot drift on the positional stability of 2D images has been studied previously experimentally, as well as using computer simulation techniques [62], [127]–[132]. Most experimental methods consist of observing the drift of a stationary reference object in 2D images over a period of time. Reference objects used in experiments include a small metal sphere [62], calibrated ruby spheres [131], a calibrated hole plate [127] and a cross wire [132]. Specific features of such reference objects are determined in each projection and the change in position of the feature between images is calculated. The observed positional changes of the feature are attributed to the instability of the focal spot. In literature, the instability of the focal spot is often referred to as the drift of the focal spot. Assigning the instabilities of 2D images solely to the drift of the focal spot can be misleading, since other factors, such as the mechanical rigidity of the X-ray tube-object-detector assembly, variations in the X-ray flux and electronic properties of the detector can all influence the overall stability of 2D images. Understanding how much each factor contributes to the drift in 2D images can be problematic. During experimental investigations it has been observed that even with the same X-ray system, different experimental arrangements can produce different values of the overall drift (see sections 3.3.3 and 3.3.4). Another technique for measuring the focal spot drift is described in [133]. Here, the focal spot drift was attributed to and derived from the length extension of the X-ray tube due to its thermal expansion, which was measured using a micrometer gauge.

Although the aforementioned investigations provided estimates for the magnitude of the drift attributed to the focal spot, it was difficult to perform a comparison of the results. The difficulty was in part due to the fact that the studies were carried out using a number of XCT systems with a variety of experimental set-ups. The comparison was complicated further by the differences in the way the focal spot was defined and the drift data was presented and interpreted. For example, one study reported a repeatable nature of the focal spot drift, where the focal spot drift was identified as the main contributor to the positional instability of 2D images [127]. Another study found the drift to be linear with superimposed sinusoidal oscillations [62]. Such differences in experimental set-ups and data reporting stem from the fact that there are currently no internationally accepted standards and procedures for characterising focal spot drift in industrial XCT systems. Despite the difficulties in comparing the results from previous investigations, a few conclusions about focal spot drift can be drawn: a) a shift in the position of a reference object in 2D images was evident in all reported experiments; b) the largest shift in 2D images was observed in the first few minutes of the experiment, corresponding to the largest focal spot drift due to rising temperatures inside the X-ray tube; and c) increasing the power of the X-ray tube increases the magnitude of the focal spot drift [131].

The purpose of the present study was to

- conduct an investigation of the focal spot drift and its correlation with thermal behaviour in an industrial microfocus cone-beam XCT system built for metrological applications;
- to evaluate the effect of the focal spot drift on dimensional measurement using computer simulations;
- based on the experimental results, to propose techniques which allow the evaluation of the focal spot drift as part of the acceptance test, re-verification test, interim checks or probe verification procedure in XCT systems.

3.2 Methodology

3.2.1 XCT system

The present study of focal spot drift was the first to be conducted on an industrial XCT system built specifically for metrological applications. The system used in this study was a Nikon Metrology XT H 225 M located at the National Physical Laboratory (NPL). One distinct feature of this XCT system is that the target part of the X-ray gun is mounted into a metal bracket which is firmly attached to the metal frame inside the chamber. Such design mitigates the effect of the elongation of the X-ray tube due to thermal expansion during scanning on the positional stability of the focal spot. The manufacturer's specification of the system is shown in table 3.1.

Table 3.1 XT H 225 M system manufacturer's specification

| | |
|-----------------------------|--------------------------------------|
| Dimensions: | |
| Source-to-detector distance | 1180.071 mm (nominal) |
| Enclosure temperature | 19 °C to 21 °C |
| X-ray source: | |
| Type | Nikon Metrology 225 kV open tube |
| Operating voltage | 25 kV to 225 kV |
| Beam current | 0 mA to 2 mA |
| Target material | tungsten, molybdenum, silver, copper |
| Target type | reflection |
| Detector: | |
| Type | PerkinElmer XRD 1620 AN3 CS |
| Active pixels | 2 000 × 2 000, with 200 µm pitch |

The tungsten part of the multi-target was used during these experiments.

3.2.2 Materials and experimental setup

Environmental conditions and temperature recordings

The XCT system was located in an air-conditioned laboratory with the temperature controlled to $20.0\text{ °C} \pm 0.1\text{ °C}$ and relative humidity of $45\% \pm 5\%$. The system is fitted with an internal cooling system which is specified to maintain the temperature inside the chamber at $20.0\text{ °C} \pm 1.0\text{ °C}$. In order to record temperature fluctuations during the experiments, an Edale CD1.1 thermometer with three disc thermistors for measuring surface temperature was used. The resolution of the thermometer is $\pm 0.01\text{ °C}$. Sensor 1 was placed on the metal part of the X-ray tube just above the target. Sensor 2 was attached to the water pipe below

the target and sensor 3 was attached to the filter mount adjacent to the reference object (figure 3.3). Temperature readings from each sensor were taken every 8 s.

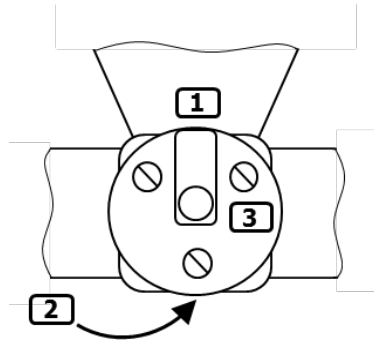


Figure 3.3 Positions of three thermal sensors on the X-ray tube: Sensor 1 is attached to the lower part of the tube, sensor 2 is attached to the water pipe underneath the target, and sensor 3 is attached to the filter holder next to the reference object.

The design of the reference object

In this study of the focal spot drift, a novel reference object was designed with the aim of minimising the number of factors that can contribute to the overall instability in 2D images. The reference object was a steel sphere of 0.79 mm diameter attached to a borosilicate glass plate of 10 mm thickness (figure 3.4). The nominal thermal expansion coefficient of steel is $12 \times 10^{-6} \text{ K}^{-1}$ [134] and that of borosilicate is $3.3 \times 10^{-6} \text{ K}^{-1}$ [135]. Both materials can be easily purchased off the shelf. Such design of the reference object offered several advantages in observing the drift of the focal spot. Firstly, the ability to place the reference object directly into the filter holder, attached to the opening of the X-ray tube, allowed the elimination of the structure containing the rotation stage as an additional source of mechanical instability. Secondly, such close proximity to the opening of the X-ray tube maximised the magnification, thus improving the sensitivity in the observed focal spot drift. The magnification factor m was approximately 130. Thirdly, since steel has a relatively high attenuation coefficient compared to borosilicate, 2D images of a sphere have good signal-to-noise ratio, allowing for a more accurate edge detection during image processing. In addition, due to borosilicate acting as an extra filter for filtering soft X-rays, the uniformity of the background in 2D images over the scan duration was also improved.

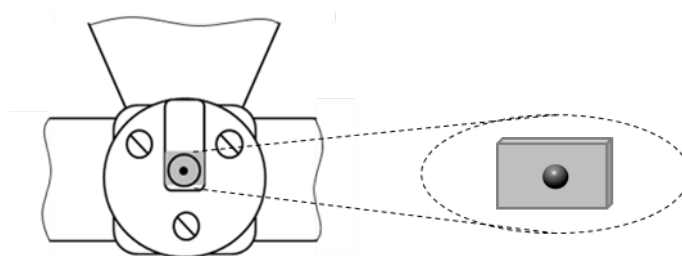


Figure 3.4 The reference object fitted into the filter holder at the opening of the X-ray tube (not to scale).

Image acquisition

To analyse the focal spot drift in the Nikon Metrology XT H 225 M, thirty-eight scans were acquired over a three month period. During this time the filament was changed twice. The X-ray tube was operated at power below 6 W, so as to avoid the auto-defocusing of the focal spot. Image acquisition settings were at one frame per second, with one frame per projection. In all experiments the reference object was placed in the holder for at least two hours before being scanned, to minimise motion due to settling of the object. In accordance with the manufacturer's instructions, the XCT system remained switched on even when no X-rays were produced. To assess the influence of the X-ray tube temperature, experiments were performed in two modes: cold and hot.

Cold mode:

- no X-rays were generated before the start of the scan,
- each scan comprised 3 142 images (the optimal number of images for these settings),
- eighteen cold scans were acquired.

Hot mode:

- the X-rays were switched on for at least twenty minutes prior to the scan,
- each scan comprised 10 000 images (the maximum number of images),
- eighteen hot scans were acquired.

To evaluate the behaviour of the focal spot over a much longer period of time, two additional scans lasting over eleven hours were performed. Such scan duration was achieved by setting the maximum number of images to 10 000 and adjusting the image acquisition settings to four frames per projection (at one frame per second).

Image analysis

After completing each scan, a stack of 2D images was analysed in Matlab (MathWorks) using a procedure described in [62]. Images of the reference sphere were first cropped and the edge of the sphere was detected using the Canny edge detection algorithm with customised threshold parameters (figure 3.5a) [136]. The Canny edge detection algorithm was used, since it is widely regarded as the best ‘all-around’ edge detection method developed to date and is readily available with the image processing toolbox in Matlab (for more detail see Appendix A). As the (x,y) coordinates of the edge were identified, a circle was fitted to these coordinates using a well-established non-linear least squares circle fitting algorithm (figure 3.5b) [137]. The x and y coordinates of the centre of the fitted circle were then determined. To calculate the shift in the (x,y) coordinates of the centre of the fitted circle throughout the whole scan, the (x,y) centre coordinates in the first image were subtracted from the (x,y) centre coordinates in all subsequent images.

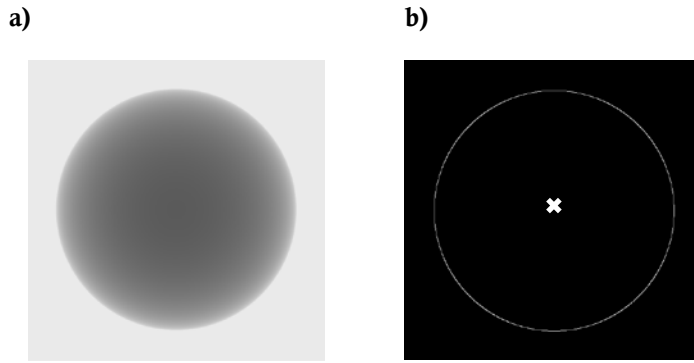


Figure 3.5 Image processing: a) a cropped image of the reference sphere and b) circle fitted to the traced boundary.

Once the shift in the (x,y) centre coordinates was identified, the focal spot drift was then calculated using equation (83), a graphical representation of which is shown in figure 3.6. This procedure was repeated for all cold and hot scans.

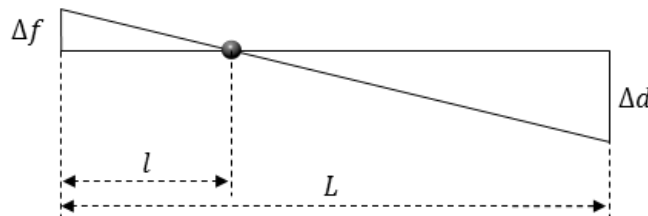


Figure 3.6 Schematic representation of the relationship between the shift of the (x,y) centre coordinates and the drift of the focal spot. Here, Δf is the drift of the focal spot, Δd is the corresponding shift of the centre of the reference object in the image plane, l is the distance between the focal spot and the centre of the reference object and L is the distance between the focal spot and the image plane.

$$\Delta f = \Delta d \frac{l}{L-l} = \frac{\Delta d}{m-1}, \text{ where } m = \frac{L}{l}. \quad (83)$$

Here, Δf is the drift of the focal spot, Δd is the corresponding shift of the centre of the reference object in the image plane, l is the distance between the focal spot and the centre of the reference object, L is the distance between the focal spot and the image plane and m is magnification.

3.2.3 Simulation of the focal spot drift

An additional computer simulation study was conducted for the purpose of evaluating the influence of the focal spot drift on the reconstructed 3D model of the sphere. Simulations of 2D images of a sphere were performed in Matlab, using a bespoke code.

Parameters used to simulate 2D images:

1. The coordinate system used for simulating 2D images is shown in figure 3.7.

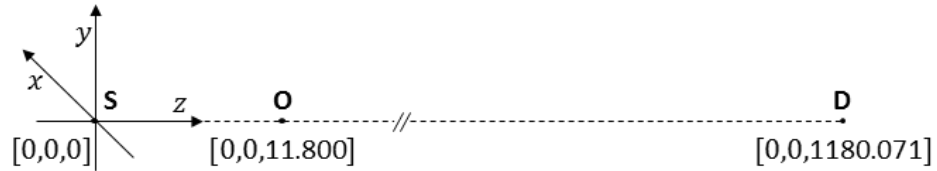
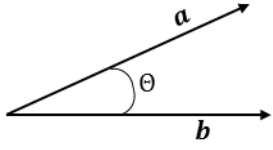


Figure 3.7 Schematic representation of the coordinate system for simulating 2D images of the sphere. The $[x, y, z]$ coordinates of the point source S were set to $[0, 0, 0]$; the coordinates of the centre of the detector D were set to $[0, 0, 1180.071]$ and the coordinates of the centre of the sphere O were set to $[0, 0, 11.80071]$.

2. The coordinates $[x, y, z]$ of the point source were set to $[0,0,0]$; the coordinates $[x, y, z]$ of the centre of the detector were set to $[0,0,1180.071]$, where 1180.071 is the source-to-detector distance (SDD) in mm, used here since this is the value of SDD in the XCT system used in the experimental study; the coordinates $[x, y, z]$ of the centre of the sphere were set to $[0,0,11.80071]$, where 11.80071 is the source-to-object distance (SOD) in mm at magnification $m = 100$.
3. The diameter of the sphere was set to 1 mm and the pixel size was set to 0.2 mm.

4. First, the $[x, y, z]$ centre coordinates for all pixels in the image (in mm) are calculated. Then, the angles between the position vector of the centre of the sphere and the position vector of the centre of each pixel are calculated using the dot product of two vectors:



$$\cos(\theta) = \frac{\mathbf{a} \cdot \mathbf{b}}{|\mathbf{a}||\mathbf{b}|} , \quad (84)$$

where \mathbf{a} and \mathbf{b} are vectors and θ is the angle between them. Knowing all the angles allows the calculation of the ray paths through the sphere.

5. The lengths of the paths of the rays through the sphere was calculated using equation (85), and is schematically represented in figure 3.8.

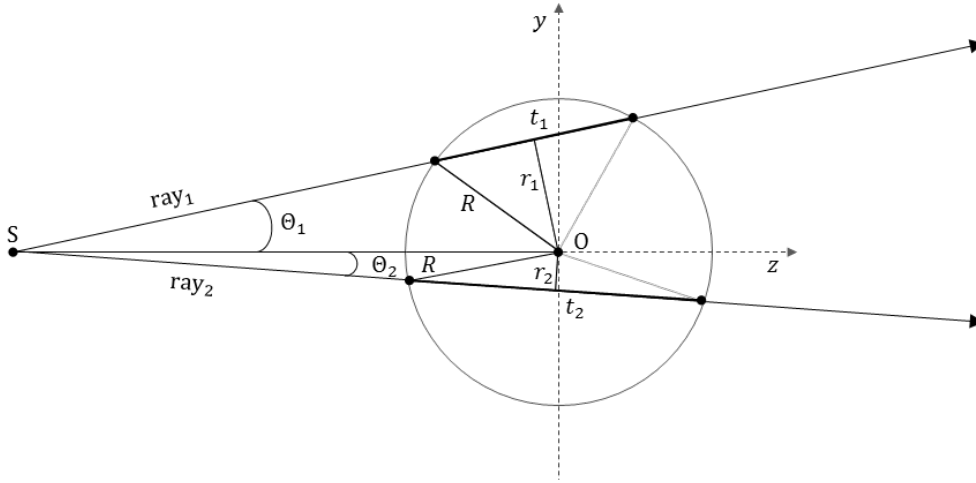


Figure 3.8 Schematic representation of X-ray paths through the sphere; where R is the radius of the sphere, r_i is the distance from the centre of the sphere to a given X-ray, SO is the source-to-object distance, θ_i is the angle between SO and a given X-ray and t_i is the length of the path of a given X-ray through the sphere.

$$t_i = 2\sqrt{R^2 - r_i^2} , \text{ where } r_i = SO \times \sin(\theta) \quad (85)$$

where R is the radius of the sphere, r_i is the distance from the centre of the sphere to a given X-ray, SO is the source-to-object distance, θ_i is the angle between SO and a given X-ray and t_i is the length of the path of a given ray through the sphere.

6. The intensity value I of each pixel in the image was calculated using the Beer-Lambert law for a monochromatic X-ray beam

$$I = I_0 e^{-\mu t}, \quad (86)$$

where I_0 is the initial X-ray intensity, set to 60 000; the linear attenuation coefficient μ was set to 9.488 cm^{-1} , which is the linear attenuation of iron at 60 kV; and t is the length of the X-ray path through the sphere. (These values for the linear attenuation coefficient and the accelerating voltage were used in computer simulations in order to approximate the conditions set during the experimental study). All images were simulated without additional noise or scatter effects.

7. Several image stacks of the sphere were simulated using different source settings:

- a) Image stack 1 was simulated with the source $[x, y, z]$ coordinates set to $[0, 0, 0]$ for every image, i.e. the image stack was produced using stationary source;
- b) Image stack 2 was simulated using the focal spot drift data from cold scan A, acquired during the experimental part of the study.
- c) Image stacks 3, 4 and 5 were simulated with the position of the source gradually drifting by up to $10 \text{ }\mu\text{m}$ during the course of 361 images. For image stack 3 the drift was in the x -axis, for image stack 4 the drift was in the y -axis and for image stack 5 the drift was in the x -axis and the y -axis simultaneously.
- d) Image stacks 6, 7, 8, 9 and 10 were simulated with the position of the source gradually drifting by up to $50 \text{ }\mu\text{m}$ during the course of 361 images. For image stacks 6 and 7 the drift was in the x -axis and the y -axis, respectively; for stack 8 the drift was in the x -axis and the y -axis simultaneously. For image stacks 9 and 10 the drift was in the positive and the negative z -axis, respectively. Although the drift value of $50 \text{ }\mu\text{m}$ is many times greater than any value observed during the experimental part of the study, it was chosen in order to understand how large values of the focal spot drift can affect dimensional measurement.

Figure 3.9 shows the profiles of the first and the last images in the image stacks simulated using different source drift settings.

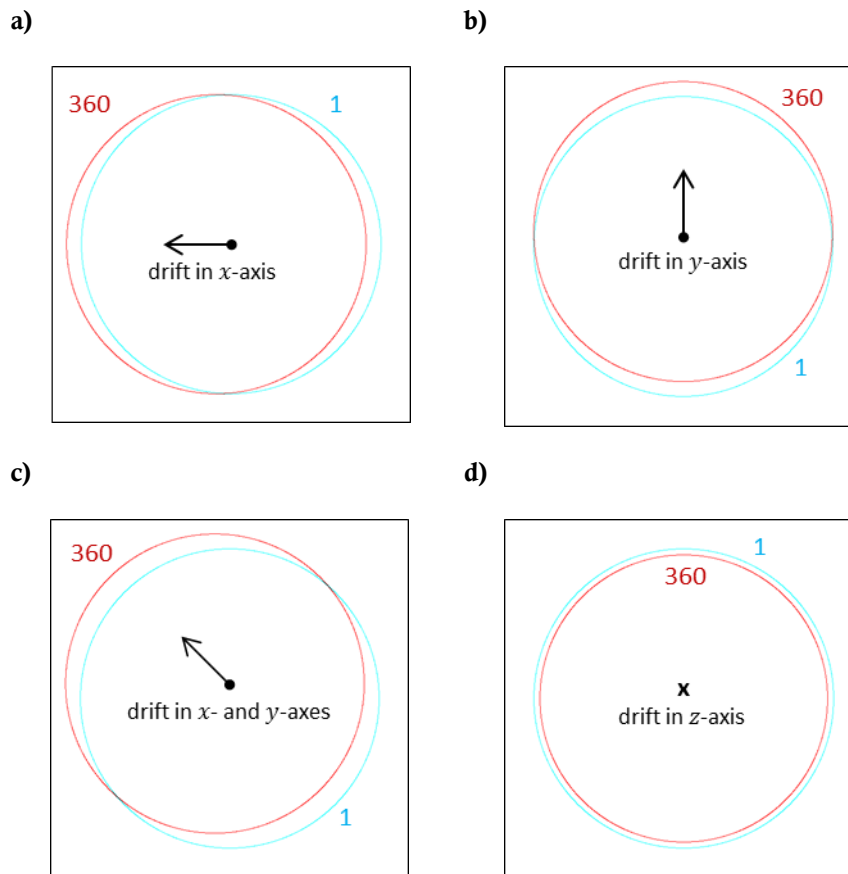


Figure 3.9 The profiles of the first (blue colour) and the last (red colour) images in the image stacks simulated using different source drift: a) drift in the x -axis; b) drift in the y -axis; c) drift in the x -axis and the y -axis and d) drift in the z -axis.

8. Simulated image stacks were then reconstructed in to 3D volumes of spheres using Nikon CT Pro 3D software. The reconstructed 3D volumes were analysed using VG Studio. The iso-surface of the sphere model was calculated using the mean grey value of the background and the mean grey value of the material. Subsequently, a sphere was fitted to iso-surface using Gaussian (least squares) fit with 1 000 sampling points. This enabled the calculation of the diameter of the fitted sphere and the range of the radial residuals to the fit, i.e. the apparent form error of the reconstructed sphere (figure 3.10). The diameter and the form error of the 3D model of the sphere simulated using a stationary source, were compared to the diameter and the form error of the 3D models of the spheres simulated using a moving source.

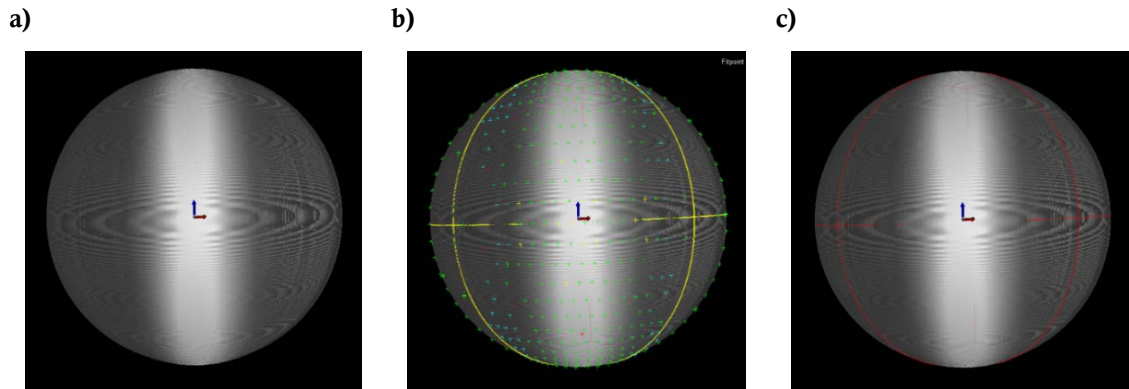


Figure 3.10 The analysis of the reconstructed 3D sphere volume using VG Studio software: a) an image of the 3D volume of the sphere; b) image showing the process of sphere fitting using Gaussian (least squares) fit and c) an image of the sphere fitted to the iso-surface of the 3D volume.

3.2.4 A short comparison study

A short comparison study of the focal spot drift using the newly developed reference object and cold scan settings was subsequently performed on the Nikon Metrology XT H 225 M located at the University of Padova, Italy. The X-ray tube was operated at power below 6 W. The three thermal sensors were placed as follows: Sensor 1 was placed on the metal part of the X-ray tube just above the target; sensor 2 was attached to the detector and sensor 3 was attached to the filter mount adjacent to the reference object (figure 3.11). The resolution of the thermometer was ± 0.1 °C. Temperature readings from each sensor were taken every 30 s. Image analysis and further calculations of the focal spot drift were performed using the above described methodology. The focal spot drift data acquired during the comparison study was then used in the simulation study for image stack 11.

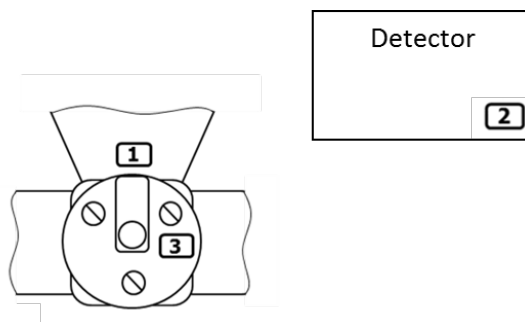


Figure 3.11 Positions of three thermal sensors in the comparison study: Sensor 1 is attached to the lower part of the X-ray tube, sensor 2 is attached to the detector and sensor 3 is attached to the filter holder next to the reference object.

3.3 Results and discussion

3.3.1 Analysis of cold scans

Temperature data analysis

Eighteen cold scans were acquired over a period of three months. Figure 3.12 shows a temperature log of the sensors 1, 2 and 3 of a typical cold scan, here scan A. From the moment the X-rays were switched on, the temperature sensor attached to the lower part of the tube, sensor 1, showed a steady increase in temperature of around 0.2 °C over the initial eight minutes of the scan. Thereafter the temperature stabilised, varying within less than 0.05 °C throughout the scan. The sensor attached to the water pipe, sensor 2, recorded a stable temperature irrespective of whether the X-rays were switched on or off. The readings were fluctuating within 0.06 °C throughout the experiment. Sensor 3, which was attached to the filter holder adjacent to the reference object, recorded a more rapid and of greater magnitude increase in temperature. Here, temperature increased by almost 0.9 °C within the first four minutes, thereafter it stabilised and continued to fluctuate within 0.05 °C. In the XCT system used in these experiments, there is a time delay between the production of X-rays at the start of the scan and the acquisition of the first image. This delay varies from several seconds to several minutes depending on scan settings; for scan A the delay was around 30 s. During this time sensor 3 recorded a rise in temperature of over 0.4 °C, which is almost half of its total increase. Since sensor 3 was placed close to the reference object, it can be inferred that the reference object underwent a similar temperature increase to the one recorded by sensor 3. It is unlikely, however, that any movement of the reference object associated with its thermal expansion influenced the calculation of the focal spot drift. This is due to the fact that the design of the reference object and its positioning in the filter holder would have ensured the isotropic thermal expansion of the object, thus allowing the calculation of the (x,y) centre coordinates of the fitted circle in each image to be unaffected.

At the start of each scan, sensor 1 displayed approximately 1 °C higher temperature than sensors 2 and 3. This is due to the fact that sensor 1 was attached to the lower part of the gun where the focus coil, which is constantly energised, is located.

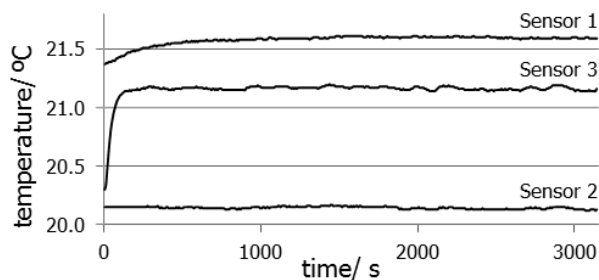


Figure 3.12 Temperature log of the three sensors in scan A. Here, sensor 1 is attached to the lower part of the tube, sensor 2 is attached to the water pipe and sensor 3 is attached to the filter holder adjacent to the reference object.

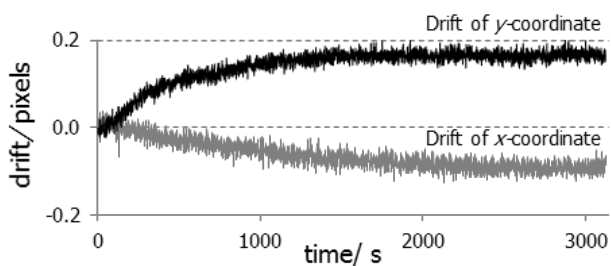


Figure 3.13 Drift of the (x,y) centre coordinates in the image plane in scan A.

Drift data analysis

Figure 3.13 shows the drift of the (x,y) coordinates of the centre of the fitted circle in a series of 2D images acquired during scan A. It is essential to note that this drift is due to the combination of the relative motion between the focal spot, the reference object and the detector; therefore, it is difficult to establish a direct correlation between observed drift and any individual components in the system. However, with the current experimental setup, it was reasonable to assume that the instabilities of the 2D images were predominantly due to the drift of the focal spot.

In scan A, the total drift of the x -coordinate was around 0.1 pixels ($20\text{ }\mu\text{m}$) and the drift of the y -coordinate was just below 0.2 pixels ($40\text{ }\mu\text{m}$). At magnification of 130 and the detector pixel size of $200\text{ }\mu\text{m}$, the corresponding drift of the focal spot in the x -axis was calculated using equation (79) to be around $0.15\text{ }\mu\text{m}$, and in the y -axis was approximately $0.3\text{ }\mu\text{m}$. (Overall, the drift of the (x,y) centre coordinates in the x -axis did not exceed 0.15 pixels ($30\text{ }\mu\text{m}$), corresponding to approximately $0.25\text{ }\mu\text{m}$ drift of the focal spot; and the drift in the y -axis did not exceed 0.4 pixels ($80\text{ }\mu\text{m}$), corresponding to approximately $0.6\text{ }\mu\text{m}$ drift of the focal spot for any cold scan acquired during this study). In most cold scans a slightly larger drift of the y -coordinate, compared to the x -coordinate was observed. The initial drift of the y -coordinate was predominantly in the upward y -direction; no such preferential direction of motion was seen in the x -axis. The drift patterns of the (x,y) coordinates appear to be in close correlation with the rise in temperature recorded by the sensor 1, attached to the lower part of the tube (figure 3.14).

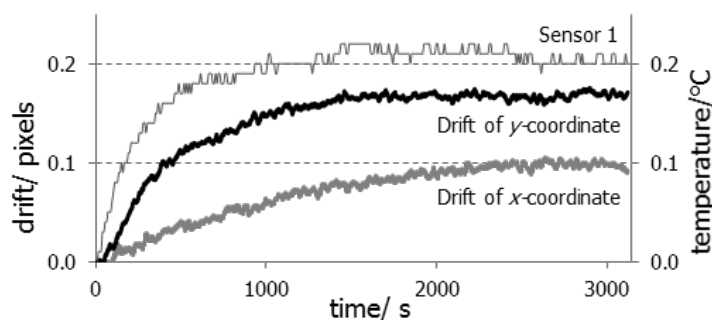


Figure 3.14 Correlation of the temperature log of sensor 1, which is attached to the lower part of the tube and the magnitude of the rolling average of the drift of the x -coordinate and the y -coordinate in the image plane in scan A.

The correlation between the drift of the y -coordinate in the upward y -direction and the increase in tube temperature is a clear indication that the observed drift was predominantly due to the changing geometry inside the tube and the expansion of the target in particular, as discussed in section 3.1 figure 3.2. It is hypothesised that any deviation in the form of the target rod from the perfect cylinder either due to manufacturing process or material damage and any deviation from its alignment along the x -axis can produce the drift of the centre coordinate in the x -axis. In addition, the possible instability associated with the electronic parts of the X-ray tube used for steering and focusing the electron beam can also contribute to the observed drift.

3.3.2 Analysis of hot scans

Temperature data analysis

Figure 3.15 shows the temperature log of a typical hot scan (scan B). Unlike cold scans, where a clear increase in temperature was recorded by sensor 1 and sensor 3, no such increase was observed in hot scans. The temperature fluctuations for all three sensors did not exceed $0.1\text{ }^{\circ}\text{C}$ in any of the scans. These results confirm that switching the X-rays on for at least twenty minutes prior to the start of the scan, allows the XCT system to reach its thermal equilibrium, which is sustained throughout every experiment.

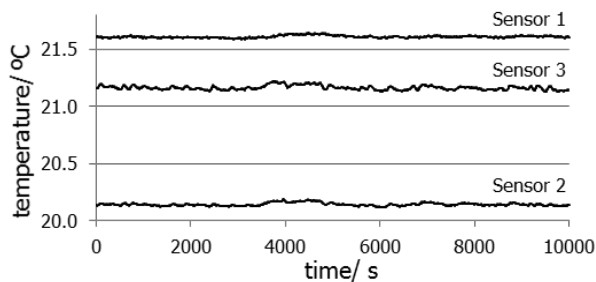


Figure 3.15 Temperature log of the three sensors in scan B.

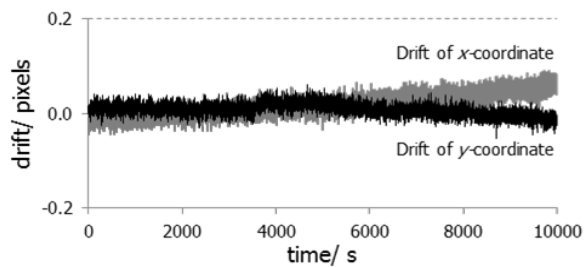


Figure 3.16 The drift in the (x,y) centre coordinates in the image plane in scan B.

Drift data analysis

Figure 3.16 shows the drift of the (x,y) coordinates of the centre of the fitted circle in scan B. Despite stable temperature recorded by all three sensors, there was a presence of the drift in both axes. The drift of the x -coordinate was less than 0.07 pixels ($14\text{ }\mu\text{m}$); at magnification of 130 it corresponds to approximately $0.1\text{ }\mu\text{m}$ drift of the focal spot in the x -axis. The drift of the y -coordinate was around 0.03 pixels ($6\text{ }\mu\text{m}$), corresponding to approximately $0.05\text{ }\mu\text{m}$ drift of the focal spot in the y -axis. In all eighteen hot scans, lasting 10 000 s each (three times the length of a standard industrial scan), no drift of the (x,y) centre coordinates exceeded the magnitude of 0.1 pixels ($20\text{ }\mu\text{m}$). This value corresponds to approximately $0.15\text{ }\mu\text{m}$ drift of the focal spot in either axis. It is interesting to note that most of the drift was observed approximately 75 minutes after the start of the scan (around 4 500 images), indicating that if a standard industrial scan of 3 143 images was performed using hot scan conditions, any shift in the (x,y) centre coordinates would have been within the image noise. The results of the drift data for the hot scan suggest that, unlike in cold scans, the recorded drift of the (x,y) centre coordinates is not due to the thermal conditions inside the X-ray tube. Possible reasons for the observed drift can be a combination of the changing surface of the target due to the prolonged bombardment by X-rays, the instability within the ‘X-ray tube-metal frame-detector assembly’ over the duration of the hot scan, as well as the instability associated with the electronic parts of the X-ray tube used for steering and focusing of the electron beam. The comparison of the results of the hot and cold scans supports the idea that although the focal spot drift was due to a number of the above mentioned factors, the largest observed drift of the (x,y) centre coordinates was associated with the increasing temperature of the X-ray tube.

3.3.3 Long-term stability

Drift analysis of the eleven hour scan with reference object placed into the filter holder

The purpose of the first long scan was to evaluate a long-term stability of the XCT system at power below 6 W. The long scan comprised 10 000 images and lasted over eleven hours (scan C). Although this scan was performed in cold mode, due to the length of the experiment, there was a time delay of approximately ten minutes between the start of the scan when the X-rays were switched on and the time of the acquisition of the first image. Consequently, most of the temperature rise happened before the acquisition of the first image.

Just as in hot scans the temperature sensors recorded stable temperatures slightly fluctuating within 0.1 °C throughout the scan. Despite the thermally stable conditions, a clear drift of the (x,y) centre coordinates was observed (figure 3.17). Over eleven hours a total drift of the x -coordinate was just over 0.4 pixels (80 μm), corresponding to approximately 0.6 μm drift of the focal spot in the x -axis. The drift of the y -coordinate was around 0.1 pixels (20 μm), corresponding to 0.15 μm drift of the focal spot in the y -axis.

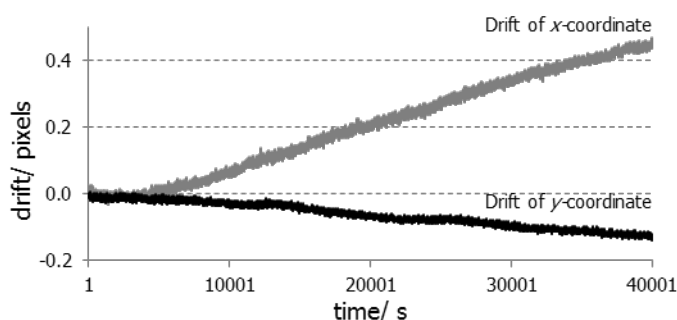


Figure 3.17 The drift of the (x,y) centre coordinates in the image plane in scan C.

Based on these results, it can be inferred that the observed drift was not due to increasing temperature inside the X-ray tube. As stated previously, the possible explanation for the observed drift was a combination of the changing surface of the target due to the prolonged bombardment by X-rays, the instability within the 'X-ray tube-metal frame-detector assembly' over 11 hours, as well as the instability associated with the electronic parts of the X-ray tube used for steering and focusing of the electron beam. Just as in hot scans, most of the drift was observed after 75 minutes from the start of the scan, with any shift of the (x,y) centre coordinates during the time required for a standard industrial scan being within the image noise. However, understanding the focal spot drift pattern during a prolonged period

of time can give a good indication of the maximum number of frames per projection that can be used before introducing unwanted effects from the focal spot drift.

Drift analysis of the eleven hour scan with reference object placed next to the rotation stage

The purpose of the second long scan (scan D) was to evaluate the long-term drift in 2D images when the reference object was mounted onto the mechanical structure containing the rotation stage. The reference object was glued to a metal stand which was fixed to the metal plate on the source side of the rotation stage, on the axis, so as to remain nominally stationary during the stage rotation associated with measurement. The reference object was then left for two hours before being scanned, in order to minimise motion due to the settling of the sample. Due to the motion of the rotation stage, some parasitic motion of the reference object was anticipated during measurement. Magnification in this experiment was around 61. All other experimental settings were identical to those of the previous long scan. As in scan C, the temperature fluctuations for all three sensors did not exceed $0.1\text{ }^{\circ}\text{C}$ throughout the experiment. Figure 3.18 shows the drift of the (x,y) centre coordinates in scan D. Over eleven hours the drift of the x -coordinate was linear in nature with magnitude of around 1.6 pixels ($320\text{ }\mu\text{m}$), corresponding to approximately $5.3\text{ }\mu\text{m}$ drift of the focal spot in the x -axis. The drift of the y -coordinate was random in nature with fluctuations of up to 0.2 pixels ($40\text{ }\mu\text{m}$), corresponding to around $0.66\text{ }\mu\text{m}$ drift of the focal spot in the y -axis. The comparison of data from scans C and D in figures 3.17 and 3.18 clearly demonstrates that the contribution to the total drift in 2D images due to the instability of the structure containing the rotation stage is greater than the contribution from drift of the focal spot at tube power below 6 W.

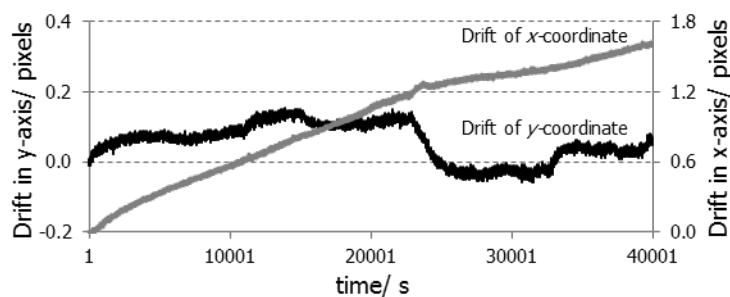


Figure 3.18 The drift of the (x,y) centre coordinates in the image plane in scan D.

3.3.4 Analysis of the cold scan acquired on the XCT system at the University of Padova, Italy

Figure 3.19 shows a log of temperature changes recorded by sensors 1, 2 and 3 during the cold scan acquired on the Nikon Metrology XT H 225 M at the University of Padova. From the moment the X-rays were switched on, the temperature sensor attached to the lower part of the tube, sensor 1 showed a continual increase in temperature by approximately 1.6°C throughout the initial forty minutes of the scan. Thereafter the temperature stabilised, varying within less than 0.1°C . The sensor attached to the detector, sensor 2, recorded a stable temperature throughout the scan, apart from a few short periods, where temperature increased by 0.1°C . Sensor 3, which was attached to the filter holder adjacent to the reference object, recorded a rapid increase in temperature by approximately 1.2°C during the initial 20 minutes. Thereafter, the temperature stabilised, varying within less than 0.1°C .

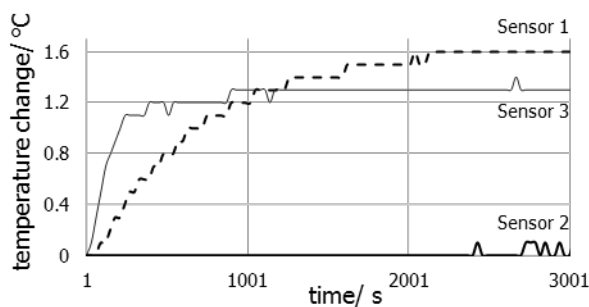


Figure 3.19 The log of the temperature change in cold scan in the comparison study. Here, sensor 1 is attached to the lower part of the tube, sensor 2 is attached to the detector and sensor 3 is attached to the filter holder adjacent to the reference object.

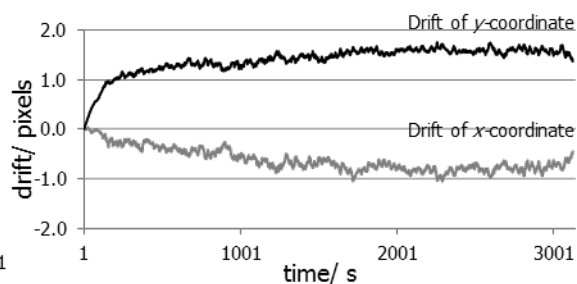


Figure 3.20 The magnitude of the rolling average of the drift of the (x,y) centre coordinates in the image plane in the comparison study.

Although the X-ray tube was operated at power below 6 W, temperature increase recorded in this study was significantly larger than in the study conducted at NPL. This was due to the fact that at the time of scan acquisition, the XCT system at Padova was experiencing malfunctioning in its cooling system. Figure 3.20 shows the drift of the (x,y) coordinates of the centre of the fitted circle in cold scan acquired during the comparison study. Here, the total drift of the x -coordinate was around 0.7 pixels ($140\text{ }\mu\text{m}$) and the drift of the y -coordinate was around 1.3 pixels ($260\text{ }\mu\text{m}$). At magnification of 120 and the detector pixel size of $200\text{ }\mu\text{m}$, the corresponding drift of the focal spot in the x -axis was calculated using equation (1) to be around $1.1\text{ }\mu\text{m}$, and in the y -axis was approximately $2.2\text{ }\mu\text{m}$.

It is interesting to note that the temperature increase recorded by sensor 1 in the comparison study was about eight times larger than the temperature increase recorded in cold scan A. The calculated magnitude of the focal spot drift in the x - and y -axes in the comparison study

was about 7.3 times larger than in cold scan A (for both axes). Although this data is not sufficient to establish the exact numerical relationship between the increase in the tube temperature and the increase in the magnitude of the focal spot drift, it further supports the idea that greater changes in tube temperature correspond to greater drift of the focal spot.

3.3.5 Analysis of the effects of the focal spot drift on size and shape of the reconstructed 3D volume of the sphere using computer simulated data

A computer simulation study was conducted in order to assess the influence of the focal spot drift on the reconstructed 3D model of the sphere. For this purpose, the image stacks were simulated using different types of the source motion, as described in sections 3.2.3 and 3.2.4. The diameter and the form error of the 3D model of the sphere with image stacks simulated using a stationary source were compared to the diameter and the form of the 3D models of the sphere with image stacks simulated using a moving source. The results are summarised in table 3.2.

Table 3.2 Comparison of reconstructed 3D models of the simulated steel sphere. The image stacks were simulated using different values of the source drift: 1) stationary source; 2) the source was shifted using data for the focal spot drift in the x - and y -axes from scan A; 3) a linear shift in the position of the source of up to 10 μm in the x -axis; 4) a linear shift in the position of the source of up to 10 μm in the y -axis; 5) a linear shift in the position of the source of up to 10 μm in the x - and y -axes; 6) a linear shift in the position of the source of up to 50 μm in the x -axis; 7) a linear shift in the position of the source of up to 50 μm in the y -axis; 8) a linear shift in the position of the source of up to 50 μm in the x - and y -axes 9) a linear shift in the position of the source of up to 50 μm in the positive z -axis; 10) a linear shift in the position of the source of up to 50 μm in the negative z -axis; 11) the source was shifted using data for the focal spot drift in the x - and y -axes from the comparison study scan.

| Source drift | Centre of rotation/ pixel | Diameter/ mm | Difference in diameter with sphere 1/ μm | Form error (peak-to- valley)/ μm |
|--|------------------------------|-----------------|--|---|
| 1. No drift | 0.0006 | 0.99916 | - | 0.89 |
| 2. Drift data from scan A | 0.1309 | 0.99914 | -0.02 | 1.13 |
| 3. 10 μm in x -axis | 2.4488 | 0.99904 | -0.12 | 4.01 |
| 4. 10 μm in y -axis | 0.0010 | 0.99896 | -0.20 | 4.85 |
| 5. 10 μm in x - and y -axes | 2.4509 | 0.99905 | -0.11 | 6.35 |
| 6. 50 μm in x -axis | 12.2800 | 0.99747 | -1.69 | 8.25 |
| 7. 50 μm in y -axis | 0.0096 | 1.00324 | +4.08 | 8.40 |
| 8. 50 μm in x - and y -axes | 12.3000 | 1.00746 | +8.30 | 8.84 |
| 9. 50 μm in the positive z -axis | 0.0005 | 1.00118 | +2.02 | 1.49 |
| 10. 50 μm in the negative z -axis | 0.0010 | 0.99702 | -2.14 | 1.34 |
| 11. Drift data from comparison study | 0.4030 | 0.99911 | -0.05 | 1.38 |

When comparing the values for the diameter and the form error presented in table 3.2, the following conclusions can be made:

- This simulation study confirms that the drift of the focal spot in the x -axis, y -axis and z -axis affects the size and the form of the reconstructed object.
- Increasing the magnitude of the focal spot drift increases the size error and the form error of the reconstructed object.
- The focal spot drift in the y -axis results in the larger size error and form error compared to the drift in the x -axis. This can be due to the fact that the reconstruction software CT Pro 2D 3.1, used in this study, corrects for instabilities in the x -axis by adjusting the centre of rotation, as seen in table 3.2 column 3.

- The drift of the focal spot in the z -axis introduces changes in magnification, causing a scaling error in the reconstructed volume, thus affecting the size of the reconstructed object. For example, for image stack 9, where the position of the source was shifted incrementally from 0 to 50 μm in the positive z -axis, the magnification increased from 100 to 100.42. For image stack 10, where the position of the source was shifted incrementally from 0 to 50 μm in the negative z -axis, the magnification decreased from 100 to 99.58. Such changes in magnification resulted in an increased diameter of 1.00118 mm for sphere 9 and in a decreased diameter of 0.99702 mm for sphere 10. When the reconstructed object is a sphere, the drift in the z -axis appears to have only a minimal influence on the form error.
- For the XCT systems used in this study and the comparison study, the manufacturer's specification for maximum permissible error (MPE) in length measurement is $(9 + L/50) \mu\text{m}$, where L is in mm. No specification is given with regards to the size error and form error. However, VDI/VDE 2630 guidelines part 1.3 states that the size error and form error must be significantly smaller than the MPE in length measurement. It can be seen that the calculated values for the diameter and the form error of the spheres simulated using drift data from cold scan A and drift data from the comparison study are in accordance with the guidelines.
- For spheres simulated using the magnitude of the source drift of 10 μm and 50 μm , both the size error and the form error are significantly increased. As stated previously, increasing the power of the X-ray tube can increase the magnitude of the focal spot drift. Since all experimental scans in this study were produced at X-ray tube power setting below 6 W, it is essential that the XCT system undergoes the focal spot drift evaluation for higher tube power settings.
- Only spheres were simulated in this study. Further study investigating the effects of the focal spot drift on measurement of length, size and form of more complex objects is needed.

3.4 Conclusions and future work

The present study of focal spot drift and its correlation with thermal behaviour of an XCT system was the first study which was conducted on an industrial XCT system built specifically for metrological applications. In order to observe the drift of the focal spot in the XCT system, a novel experimental set-up and reference object were designed in a way so as to minimise the number of factors that can influence the positional stability of 2D images. The scans were performed in two modes: cold and hot. Each cold scan comprised 3142 images, the recommended number of images for this XCT system. Each hot scan comprised 10 000 images, the maximum number of images for this XCT system. In addition, two 11 hour scans were acquired in order to assess a long-term performance of the system, as well as to evaluate the influence of the reference object positioning on the drift data.

A further novel aspect of this research was the fact that the focal spot drift data acquired during the experimental study was then used in the computer simulation study in order to assess the influence of the focal spot drift on the measurement performance of the XCT system. The newly developed focal spot drift evaluation technique was subsequently used in a short comparison study, where the magnitude of the focal spot drift and its influence on the measurement performance of the XCT system at the University of Padova, Italy were assessed. The following observations and conclusions were made:

- The thermal performance of the XCT system used in the study at NPL is summarised in table 3.3. On the basis of these results it can be concluded that the system demonstrated stable and repeatable thermal behaviour at X-ray tube settings of up to 6 W. Further studies are needed to evaluate the thermal behaviour of the system at higher power settings.

Table 3.3 Temperature data summary. Sensor 1 was placed on the metal part of the X-ray tube just above the target; sensor 2 was attached to the water pipe below the target and sensor 3 was attached to the filter mount adjacent to the reference object.

| Sensors | Temperature before switching the X-rays on | Temperature at the end of the experiments |
|----------|--|---|
| Sensor 1 | 21.38 °C ± 0.01 °C | 21.60 °C ± 0.01 °C |
| Sensor 2 | 20.15 °C ± 0.03 °C | 20.15 °C ± 0.03 °C |
| Sensor 3 | 20.30 °C ± 0.01 °C | 21.20 °C ± 0.01 °C |

- The presence of the focal spot drift was evident in all cold and hot scans.

- For all cold scans acquired over a period of fifty-three minutes, the drift of the (x,y) centre coordinates in the x -axis did not exceed 0.15 pixels (30 μm), corresponding to approximately 0.25 μm drift of the focal spot. The drift in the y -axis did not exceed 0.4 pixels (80 μm), corresponding to approximately 0.6 μm drift of the focal spot.
- In cold scans most of the drift in both axes happened during the initial eight to ten minutes. The pattern of the drift was in close correlation with the pattern of temperature increase recorded by the sensor attached to the lower part of the X-ray tube. It can, therefore, be concluded that the observed drift is predominantly due to the instability of the focal spot as the temperature inside the X-ray tube begins to rise. Others have reported the drift pattern stabilising approximately two hours after switching on the X-ray tube [131]. Given such variations in the length of time it takes for different X-ray tubes to stabilise, it is advisable for the user to identify the behaviour of the focal spot drift that is characteristic to their particular X-ray system. It is then advised, whenever possible, to allow the X-ray tube to stabilise for an appropriate length of time prior to image acquisition.
- For all hot scans acquired over a period of around three hours, the magnitude of the drift of the (x,y) centre coordinates did not exceed 0.1 pixels (20 μm) in either axis, corresponding to approximately 0.15 μm drift of the focal spot. It is important to note that most of the drift was observed approximately 75 minutes after the start of the scan (around 4 500 images), indicating that if a standard industrial scan of 3 143 images was performed using hot scan conditions, any shift in the (x,y) centre coordinates would have been within the image noise.
- No general trend to the direction of the drift was observed in hot experiments. The start direction of the drift appeared to be random; however, once the direction was initiated, the drift continued in that direction. Unlike other studies, where the drift was found to be a repeatable phenomenon, these findings make even the notion of positional correction of 2D images using previously known focal spot drift data impossible.
- The results from the 11 hour scan, with the reference object placed in the filter holder, revealed a presence of a steady drift of the (x,y) centre coordinates throughout the duration of the scan despite stable temperature readings from all three sensors. It can, therefore, be inferred that the observed drift was not only due to thermal conditions inside the X-ray tube, but also the result of additional factors that require further investigation. One possible explanation is that the drift is the result of the gradual change of the surface of the target due to its damage by the electron beam. Another possibility is that the observed drift is caused by the relative movement in the X-ray tube, metal frame and detector assembly.

- Data acquired from the 11 hour scan, where the reference object was placed onto the structure containing the rotation stage, shows a very different drift pattern of the (x,y) centre coordinates compared to all other cold and hot scans both in magnitude and direction. The result demonstrates that for this XCT system the contribution to the total drift in 2D images due to the instability of the structure containing the rotation stage is greater than the contribution from the focal spot drift. The significance of this finding is twofold. Firstly, if the main objective is to investigate the drift of the focal spot in an XCT system, it is essential that the reference object and the experimental set-up are designed in such a way as to eliminate as many additional sources of motion as possible; otherwise, drift data acquired from 2D images can be wrongly attributed to the drift of the focal spot. Secondly, if the main objective is to correct for the positional instability of 2D images using a reference object technique, it is important that the reference object is mounted in such a way that during a scan it 'follows the path' of the object of interest as closely as possible. Otherwise, this process of correction itself may introduce errors into the reconstructed 3D volume. This is not a trivial task and requires an in-depth understanding of how various parts of the XCT system perform during different scanning conditions.
- The influence of the focal spot drift on the measurement of the reconstructed object was confirmed during the computer simulation part of the study.
- The use of the focal spot drift experimental data in computer simulation study showed that when the XCT system is operated at power of up to 6 W, the magnitude of the focal spot drift characteristic to this system has only a small effect on the MPE stated by the manufacturer.
- A short comparison study of the focal spot drift and its effects on measurement in the XCT system at Padova showed that the newly developed focal spot drift evaluation technique is transferable and can be successfully applied to different XCT systems (although, the positioning of the reference object might need adjustment, depending on the design of the individual XCT system).

Based on the findings of this research the following recommendations can be made:

- The positional stability of the focal spot is an important characteristic of the X-ray probe, which can affect the overall measurement performance of an XCT system. It is, therefore, recommended that the evaluation of the focal spot drift becomes a part of the acceptance test, re-verification test, interim checks and X-ray tube qualification of XCT systems.
- Each XCT system has its own characteristic focal spot drift pattern, which can be influenced by many factors, such as the system design, the age and shape of the filament,

the settings for the steering coils and the focusing magnetic lens, the operating power of the tube, the stability of the system frame assembly, etc. Therefore, in order to effectively assess the focal spot drift of any given XCT system the following is recommended:

- a) the reference object and its positioning are adjusted in accordance with the XCT system design in such a way as to minimise the number of factors that can contribute to the overall instability in 2D images;
- b) in order to assess the influence of the focal spot drift on measurement performance of the XCT system, the focal spot drift data acquired during the experimental part of the focal spot drift evaluation is used in conjunction with further computer simulation study;
- c) since the focal spot drift can be different for different X-ray tube power settings, it is recommended that the focal spot drift evaluation technique is applied to all power settings that are frequently used by the operator.
- d) since the focal spot drift pattern is subject to change due to the factors listed above, it is recommended that the focal spot drift evaluation is performed on a regular basis, as well as every time a new filament is installed or any other changes are observed within the system.
- e) it is recommended that the results from every focal spot drift evaluation procedure are recorded. This will allow the operator to assess the long-term stability and repeatability of focal spot drift characteristics in a given XCT system.

The novel technique for evaluating the focal spot drift can be improved further by designing the reference object to comprise two calibrated spheres, which will allow the evaluation of the focal spot drift in the x -, y - and z -axes ²³. In addition, the simulation of more complex objects and phenomena, such as beam-hardening, scatter, etc., will allow investigation of the effects of the focal spot drift on measurement of length, size and form using more realistic conditions.

Novelty and contribution: a novel technique, which combines experimental analysis with computer simulations, for evaluating the focal spot drift in industrial micro-focus XCT systems has been developed; Solid evidence was acquired to support the proposition that the evaluation of the focal spot drift needs to become an essential part of the overall procedure of X-ray tube qualification.

²³ At the time of writing, a study examining the drift of the focal spot in all three axes is conducted at NPL with results to be published in Measurement Science and Technology.

Chapter 4: An investigation of the effects of off-focal radiation on dimensional measurement in cone-beam micro-focus XCT systems

4.1 Background to the study

For all X-ray tubes used in XCT systems, X-rays are assumed to originate from a single focal spot, the area of the X-ray tube where the electron beam hits the surface of the target [91]. However, as previously discussed in section 2.3.4, when the incoming electron beam interacts with the surface of the target, backscattered electrons are produced. These backscattered electrons interact with metal surfaces other than the focal spot, generating off-focal radiation. The off-focal radiation can subsequently give rise to unwanted ‘secondary focal spot’ phenomenon. In the literature, the off-focal radiation is also known as ‘secondary’, ‘extra-focal’ or ‘parasitic’ radiation [43], [89], [138]. Here these words are used interchangeably.

The exact characteristics of off-focal radiation may vary depending on the number and the direction of motion of backscattered electrons, distance from target to the tube housing, the geometry and material of the target and the housing, as well as the overall tube design. For example, in X-ray tubes with rotating anode, backscattered electrons are accelerated back towards the anode outside the focal spot area, causing low intensity X-ray emission over the entire anode area, thus reducing image contrast and increasing random image noise [1]. Dedicated apertures positioned close to the focal spot area, additional shielding as well as software algorithms have been employed to reduce the effects of off-focal radiation on image quality [89].

Unlike X-ray tubes with rotating anode, in transmission and reflection type micro-focus X-ray tubes, backscattered electrons are not accelerated back to the target. Instead, they interact with the tube housing material, generating additional high-energy X-rays inside the tube structure, thus producing characteristic secondary images of scanned objects (figure 4.1). Here, the secondary image surrounding the scanned object is also referred to as the ‘shadow effect’.

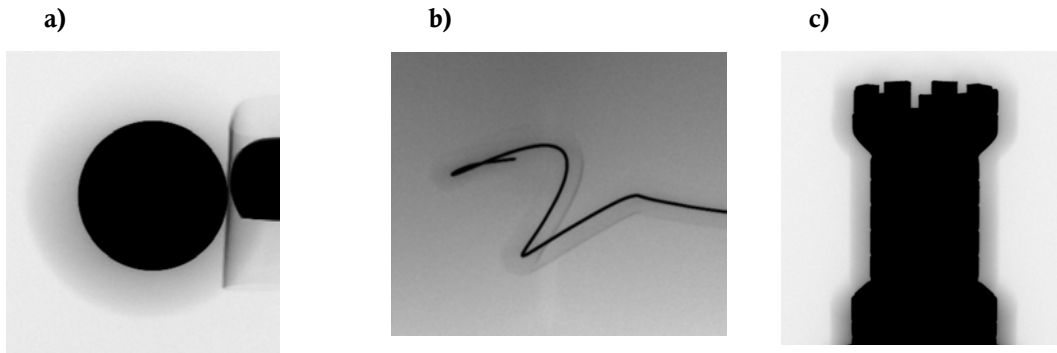


Figure 4.1 a) An image of a ruby sphere with shadow due to the secondary focal spot effect; b) an image of a tungsten wire with shadow due to the secondary focal spot effect; c) an image of a metal part with shadow due to the secondary focal spot effect. (In all images contrast is adjusted for shadow visibility). Images were produced on the Nikon Metrology XT H 225 M system at NPL: images a) and b) were produced with a new X-ray tube and image c) was produced with an old X-ray tube.

The presence of the shadow effect in 2D images was first observed when performing routine scans on the Nikon Metrology XT H 225 M system at NPL. The system underwent technical upgrades, during which the X-ray tube was replaced. The presence of the shadow effect was further seen when examining images produced using the new X-ray tube, as well as in images produced on a similar XCT system at the University of Padova, Italy.

The effects of off-focal radiation in X-ray tubes with rotating anode have been widely discussed in the literature [77], [89], [138]. However, in transmission and reflection micro-focus X-ray tubes such effects are practically undocumented [111]. Furthermore, no literature discussing the effects of off-focal radiation on dimensional measurements in micro-focus cone-beam X-ray tubes has been identified.

Following the experimental observations of the effects of off-focal radiation a novel study of this phenomenon was conducted at NPL. The purpose of the study was to

- understand the origins of the secondary radiation in micro-focus cone-beam XCT system;
- investigate the effects of off-focal radiation on dimensional measurement in an industrial micro-focus cone-beam XCT system;
- based on the results of the study, to validate whether secondary radiation in micro-focus cone-beam XCT system needs to be considered as one of the characteristics in X-ray probe verification procedure.

4.2 Methodology

4.2.1 XCT system and environmental conditions

The present study was conducted on an industrial XCT system built specifically for metrological applications. The system used in this study was a Nikon Metrology XT H 225 M located at NPL.

Table 4.1 XT H 225 M system manufacturer's specification

| | |
|-----------------------------|----------------------------------|
| Dimensions: | |
| Source-to-detector distance | 1180.071 mm (nominal) |
| Enclosure temperature | 19 °C to 21 °C |
| X-ray source: | |
| Type | Nikon Metrology 225 kV open tube |
| Operating voltage | 25 kV to 225 kV |
| Beam current | 0 mA to 2 mA |
| Target material | tungsten |
| Target type | reflection |
| Detector: | |
| Type | PerkinElmer XRD 1620 AN3 CS |
| Active pixels | 2 000 × 2 000, with 200 µm pitch |

The XCT system was located in an air-conditioned laboratory with the temperature controlled to $20.0\text{ °C} \pm 0.1\text{ °C}$ and relative humidity of $45\% \pm 5\%$. The system is fitted with an internal cooling system, which is specified to maintain the temperature inside the chamber at $20.0\text{ °C} \pm 1.0\text{ °C}$.

In this XCT system, the tilt angle, i.e. the angle between the incoming electron beam and the normal to the surface of the target, is around 60 degrees. Theoretically, at this angle, around 65 % of incoming electrons can be backscattered, with a large proportion of these 'backscattered' in the forward direction (see section 2.3.4). It is important to note that no manufacturer's specification or instructions with regards to the presence of off-focal radiation existed for the X-ray tube used in the above system.

4.2.2 Experimental setup and computer simulations

- 1) In order to observe the effects of off-focal radiation in the abovementioned XCT system during the initial stage of the experimental work, a large number of 2D images were acquired using different objects, at different magnifications, with different voltage and

current settings of the X-ray tube. Some of the scanned objects were: an old tungsten filament, tungsten edges, steel spheres and ruby spheres, etc. Voltage settings varied between 70 kV and 225 kV and current settings varying between 40 μA and 250 μA .

- 2) Once the presence of the effects of off-focal radiation was firmly established, a number of 2D images were further analysed in order to understand geometric characteristics of the secondary source and to investigate possible sources of its origin. Steel spheres of 6.36 mm and 0.79 mm in diameter, a steel gauge of 8.95 mm in width and a thin silicon window of 25.4 mm in diameter were the objects of choice for further research because of their simple geometry and availability. The analysis of 2D images of the above mentioned objects, where the sizes of the images due to primary and secondary sources were measured and compared. The derivation from the magnification geometry allowed the postulation of the possible size and location of the secondary radiation source.
- 3) A number of 2D images of spheres were simulated with the presence of the secondary source. These images were analysed and compared with the 2D images of real spheres produced on the XCT system at NPL. Simulations of 2D images of spheres were performed in Matlab using the code described in section 3.2.3, parts 1-6, with adjustments made to the magnification values. The secondary source effect was achieved by simulating a circular secondary source of 3.8 mm in diameter, displaced from the primary source by 6 mm along the z-axis in the positive direction. (The values for the secondary source were estimated from 2D image analysis as discussed in section 4.3.4). The magnitude of the intensity due to secondary source was set to 10 % of the intensity due to primary source, which was in good agreement with experimental data. All simulations were produced using a monochromatic X-ray beam of 60 kV, with iron as the sphere material (unless stated otherwise). The 2D images were analysed using Matlab and ImageJ (open source image processing software).
- 4) In order to assess the influence of off-focal radiation on the measurement performance of the XCT system, a number of additional 2D image stacks of different sphere arrangements were simulated using primary source only, and primary and secondary sources together. These stacks were reconstructed using Nikon CT Pro 3D software. The 3D volumes of the reconstructed spheres were analysed using VG Studio software. The iso-surfaces of the sphere models were identified by 'automatic' and 'advanced' surface determination techniques available in this package. The 'automatic' technique, also known as ISO-50 % [61], identifies a surface by calculating the average between the mean grey value of the background and the mean grey value of the material. In the 'advanced' technique the surface is identified by the local highest grey value gradient within the specified number of voxels, where the average between the mean grey value of the

background and the mean grey value of the material is used as the starting point. Subsequently, spheres were fitted to iso-surfaces using Gaussian (least squares) fit with 1 000 sampling points. This enabled the calculation of sphere diameters and the range of the radial residuals to the fit, i.e. the apparent form error of the reconstructed spheres. The diameter of the sphere, the form error of the sphere and, where appropriate, the uni-directional and bi-directional distances between spheres in the 3D models simulated using the primary source only were compared to the measurements in 3D models simulated using both primary and secondary sources.

- 5) Following the experimental investigation and the computer simulation study a novel test object was designed. The purpose of the test object was to assist the XCT user in evaluating the non-uniformity of the intensity distribution due to the secondary source.

4.3 Results and discussion

4.3.1 Initial analysis of 2D scanned images

In order to observe the effects of off-focal radiation in Nikon Metrology XT H 225 M during the initial stage of the experimental work, a large number of 2D images were acquired using different objects, at different magnifications, with different voltage and current settings of the X-ray tube. Some of these images are shown in figure 4.2.

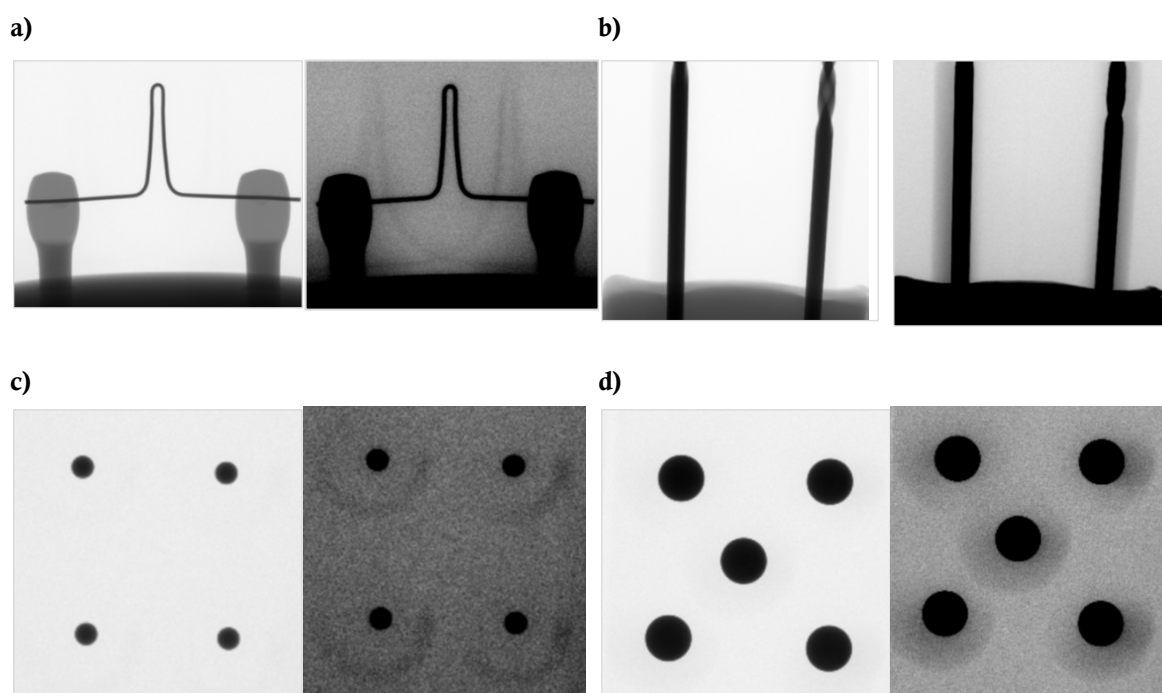


Figure 4.2 A selection of images from the initial experimental stage of the study (with original images on the left and images with adjusted contrast for shadow visibility on the right). Images were acquired using different objects and X-ray tube settings. a) An image of a filament, produced at 150 kV, 40 μ A and magnification of 40; b) an image of two drills of 1.99 mm in diameter, produced at 150 kV, 100 μ A and magnification of 10; c) an image of four steel spheres of 0.79 mm in diameter, produced at 75 kV, 80 μ A and magnification set to 15 and d) an image of five steel spheres of 2.36 mm in diameter, produced at 75 kV, 80 μ A and magnification set to 15.

When analysing multiple images taken during the initial stage of the study, the following observations about the effects of off-focal radiation have been made:

- the presence of shadow effect was evident in all 2D images, irrespective of the objects' materials or the X-ray tube settings;
- the shape and the size of the shadow in images varied depending on the size, shape and magnification of the object. For example, for small objects, such as spheres of 0.79 mm in diameter (figure 4.2c), the shadow appeared as a separate 'ring' around the sphere, whereas

for larger objects, such as the spheres of 2.36 mm in diameter (figure 4.2d), the shadow was merged with the object, thus affecting the grey value of the bulk of the object material;

- the shape and the size of the shadow in images pointed to the likelihood that the secondary source was circular in shape, located marginally in front of the primary focal spot;
- it was clear from the images that the intensity of the shadow was not radially uniform, indicating non-uniformity of the secondary source;
- the position of the shadow in 2D images did not change when adjusting the position of the primary focal spot by altering the direction of the electron beam using the X-Y steering coils. This suggested that the secondary source was due to a permanent feature inside the tube housing, which is in agreement with theoretical understanding of the origins of secondary radiation in micro-focus X-ray tubes;
- the presence of off-focal radiation affected not only the background surrounding the object, manifested as the shadow, but the imaging of the inner parts of objects themselves. For example, figure 4.3 shows images of a steel edge of 0.9 mm thickness, produced with the X-ray tube settings of 90 kV and 62 μ A, with magnification of 40. The presence of the darker area in the background, the shadow, and the lighter area inside the steel edge are clearly visible in figures 4.3b and 4.3c. The mean grey value of the background in this image is around 60 160, the mean grey value of the shadow is around 58 800, the mean grey value of lighter part of the steel edge is around 16 300 and the mean grey value of the remainder of the steel edge is 14 600.

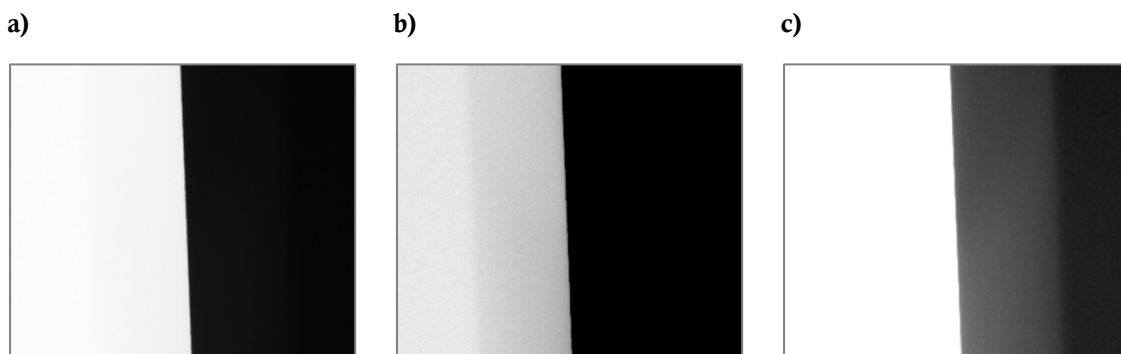


Figure 4.3 An image of a steel edge of 0.9 mm thickness: a) original image; b) same image with pixel values set between approximately 61 000 and 51 000; c) same image with pixel values set between approximately 23 000 and 13 000.

In other words, the presence of off-focal radiation can affect the grey value of the background, as well as the grey value of the object itself reducing the contrast-to-noise ratio

(CNR)²⁴. For example, the CNR of the steel edge image shown in figure 4.3 was reduced from around 286 to around 89. When comparing the profiles taken through the central row of pixels in the image of the steel edge in figure 4.3 and the image of the edge simulated without off-focal radiation, the impact of off-focal radiation on the edge profiles is clearly visible (figure 4.4). Such changes in the edge profiles can potentially lead to errors in the edge (surface) determination procedure (following the 3D reconstruction), especially for multi-material objects and objects with complex geometries.

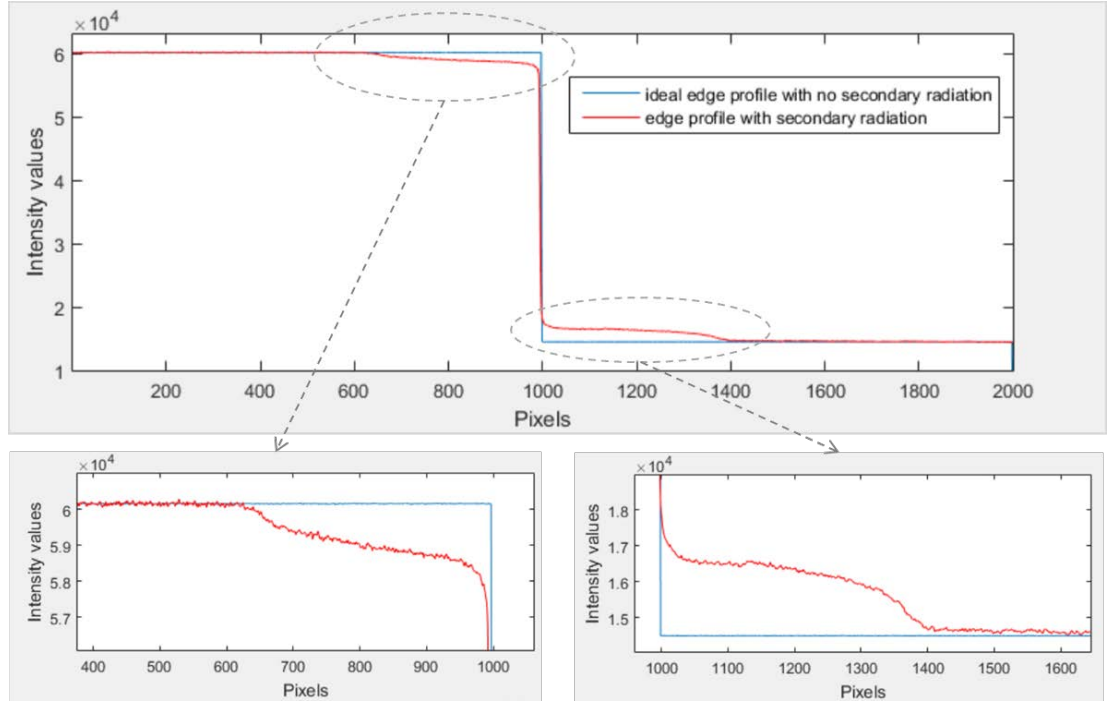


Figure 4.4 Demonstration of the difference between the profiles taken through the central row of pixels in the image of the steel edge in figure 3 and the image of the edge simulated without off-focal radiation. The edge profile is altered by the presence of off-focal radiation.

- when examining the 2D images of spheres, another interesting observation was made: for a certain sphere size and magnification setting, in addition to the shadow surrounding the sphere, there was a much darker area at the centre of the sphere, giving an appearance of a secondary object/material (figure 4.5). This effect also pointed to the likelihood of a circular secondary source.

²⁴ Contrast-to-noise ratio (CNR) is an object size-independent measure of the signal level in the presence of noise [1]. $CNR = (\bar{x}_{bg} - \bar{x}_{obj})/\sigma_{bg}$, where \bar{x}_{bg} and σ_{bg} are the mean grey level value and the standard deviation of the background, respectively, and \bar{x}_{obj} is the mean grey level value of the object.

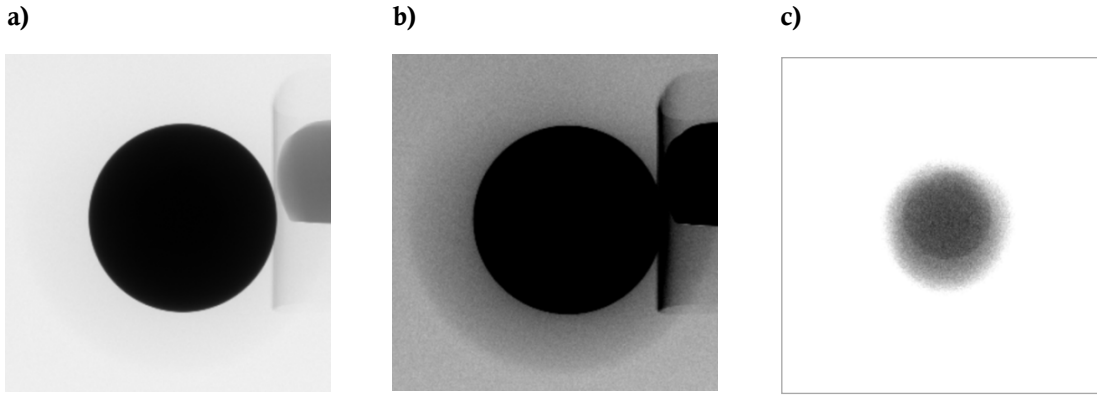


Figure 4.5 An image of a steel sphere of 6.36 mm in diameter, produced with the X-ray tube settings of 75 kV, 100 μ A and magnification 17: a) original image; b) same image with pixel values set between approximately 64 000 and 51 000; c) same image with pixel values set between approximately 300 and 1 700.

The above listed observations have been further investigated during the next stage of the study.

4.3.2 Magnification geometry in X-ray imaging

As stated previously, no a priori knowledge about the X-ray tube housing inner geometry existed; therefore, the initial location of the source of secondary radiation was estimated by trial and error, when comparing the image size due to primary radiation with the image size due to secondary radiation. Such an approach relies on the understanding of 2D X-ray image geometry and is described below.

When X-rays are emitted from a point source, magnification m of a scanned object can be determined by a ratio of the source-to-detector distance divided by the source-to-object distance:

$$m = \frac{a + b}{a}, \quad (87)$$

where a is the source-to-object distance and $(a + b)$ is the source-to-detector distance, as shown in figure 4.6. Magnification m is also known as geometric magnification [91].

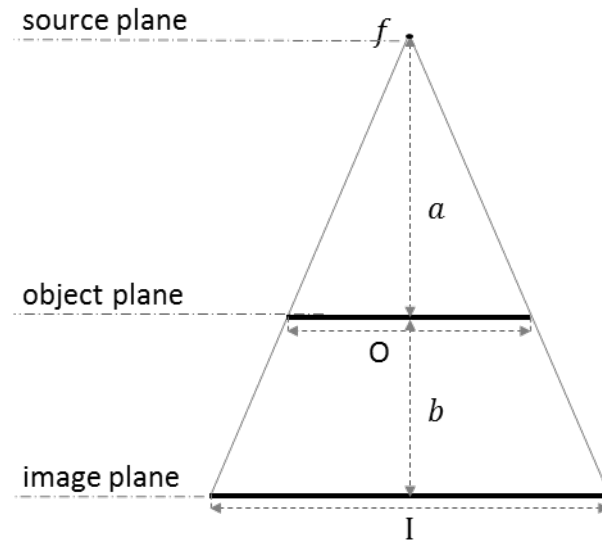


Figure 4.6 Geometry of a magnified image I of object O , produced with a point source f . Here, a is the source-to-object distance and $(a + b)$ is the source-to-detector distance.

However, for 2D images acquired using X-ray sources of finite size, the magnification value is modified. Figure 4.7 shows a schematic representation of a 2D image of a scanned object acquired using an extended X-ray source.

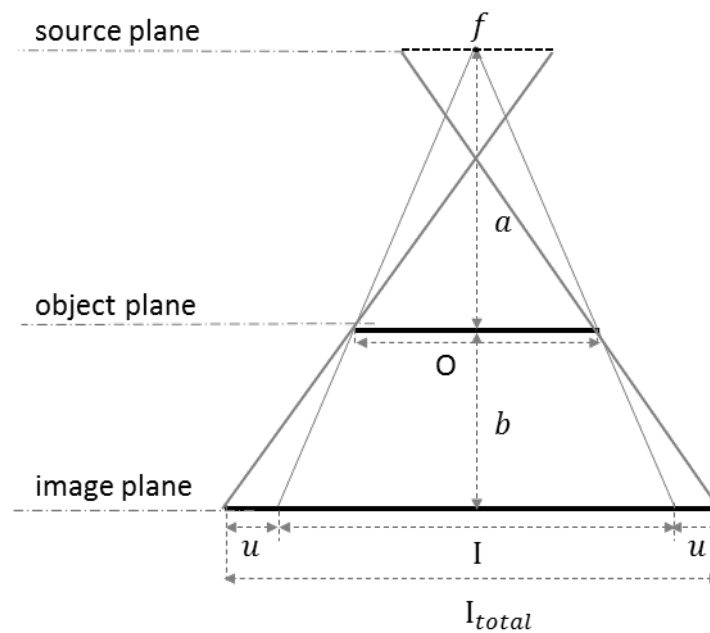


Figure 4.7 Geometry of a magnified image produced by an extended source. Here, O is the size of an object, I is the size of an image due to a point source, f is the size of an extended source, a is the source-to-object distance and $(a + b)$ is the source-to-detector distance, u is the penumbra and I_{total} is the image due to the extended source and is equal to $(I + 2u)$.

The derivation of the magnification due to the extended source, also known as ‘true magnification’ can be achieved by examining just one half of the image, as shown in figure 4.8.

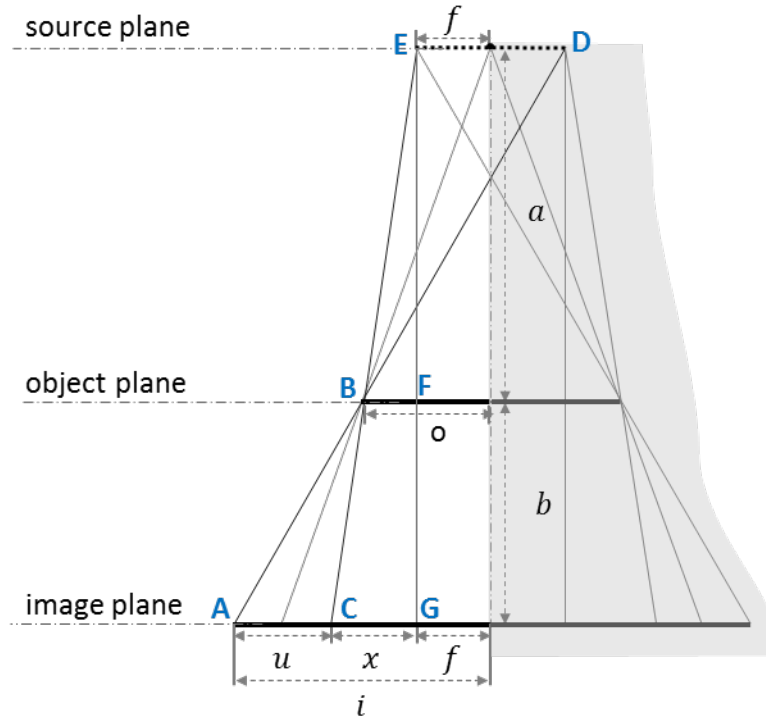


Figure 4.8 Schematic representation of image formation with the extended source. For the purposes of derivation of magnification due to the extended source, only one half of the image formation (the left side) is taken into account. Here, o is half the size of an object, f is half the size of the extended source, a is the source-to-object distance and $(a + b)$ is the source-to-detector distance and i is half the size of an image and is equal to $(f + x + u)$.

From figure 4.8 it can be seen that given an extended source of size $2f$, the left hand side of the image of size i can be represented by its constituent parts:

$$i = u + x + f. \quad (88)$$

Geometric magnification, i.e. magnification due to a point source is given by equation (87), and can be also written as

$$m = 1 + \frac{b}{a}. \quad (89)$$

Using properties of similar triangles for triangles CEG and BEF and equation (87), the following relationships are obtained:

$$\frac{x}{o - f} = \frac{a + b}{a} = m, \quad (90)$$

re-arranging the above equation, gives

$$x = m(o - f). \quad (91)$$

From the similar triangles ABC and DBE, the following relationship is obtained:

$$\frac{u}{2f} = \frac{a}{b}, \quad (92)$$

substituting (89) into (92) and re-arranging gives

$$u = \frac{2fa}{b} = 2f(m - 1). \quad (93)$$

Then, substituting values of x and u from (91) and (93) into (88) gives

$$\begin{aligned} i &= 2f(m - 1) + m(o - f) + f = \\ &= 2fm - 2f + mo - mf + f = \\ &= f(2m - 2 - m + 1) + mo. \end{aligned} \quad (94)$$

In other words, the image size due to the extended source is

$$i = f(m - 1) + mo, \quad (95)$$

and the true magnification M is, therefore,

$$M = \frac{i}{o} = \frac{f}{o}(m - 1) + m. \quad (96)$$

It can be seen from equation (96) that the true magnification is a function of not only the quotient of source-to-detector distance to source-to-object distance as with geometric magnification, but also a function of the quotient of source size to object size.

4.3.3 Initial evaluation of the secondary source properties

Taking into account the geometry of image formation, the production of backscattered electrons, observations from multiple images acquired during stage 1 of the study and the limited knowledge about the inner geometry of the X-ray tube (figure 4.9), it was proposed that the secondary source was produced from the edge of the exit window in the target housing of about 4 mm in diameter, located around 6 mm in front of the primary focal spot. The target housing is made of tungsten/copper alloy, a material suitable for generating X-rays.

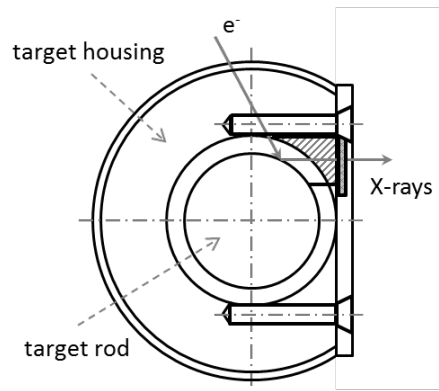


Figure 4.9 An approximate schematic representation of the micro-focus X-ray target assembly. The hatched area is part of the target housing which surrounds X-rays as they exit the target assembly through the beryllium or aluminium window (shaded area). As the backscattered electrons interact with the target housing made of tungsten/copper alloy near the exit window, secondary X-ray radiation is produced.

To confirm the initial assumptions about the size and the location of the origin of the secondary focal spot, a number of 2D images of a steel gauge of 8.95 mm in width and a thin silicon disk of 25.4 mm in diameter were examined further (figure 4.10). Using equations (87) to (96) and the properties of the XCT system as given in table 4.2, the theoretical sizes of the images of the steel gauge at three different magnification settings and of the silicon disk at one magnification setting produced by primary and secondary sources were calculated. These theoretical values were then compared with the experimentally measured values of the images of the steel gauge and the silicon disk due to the primary and secondary radiation sources. Experimental measurements of the image sizes were obtained in ImageJ by taking a profile through the central row of pixels and evaluating the boundaries between the background and images due to the primary and secondary sources based on the changes in grey values along the profile. This method adds a small amount of uncertainty due to the manual boundary selection. The results are summarized in table 4.3.

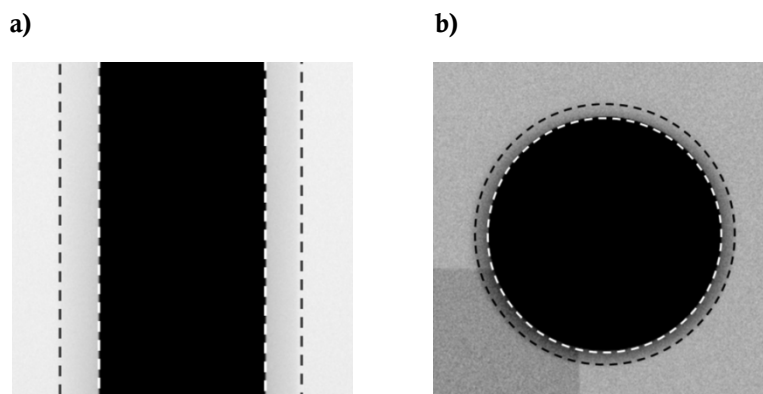


Figure 4.10 Images of a steel gauge (a) and a silicon disk (b). In both images the white dashed lines indicate images due to the primary source and the black dashed lines indicate images due to the secondary source.

Table 4.2 Summary of the XCT system properties used in calculating the image sizes of a steel gauge and a silicon window produced by primary and secondary sources.

| Properties of the XCT system | Measurements/ mm |
|---|-------------------------|
| Pixel size | 0.2 |
| Primary source to detector distance | 1180.071 |
| Estimated secondary source to primary source distance | 6 |
| Estimated secondary source to detector distance | 1174.071 |
| Estimated secondary source size/ diameter | 3.8 |

Table 4.3 Summary of the experimentally measured and theoretically calculated image sizes of the steel gauge and the silicon window produced by primary and secondary sources.

| | Magnification due to primary source | Measured image size due to primary source/ pixels | Theoretical image size due to primary source/ pixels | Measured image size due to secondary source/ pixels | Theoretical image size due to secondary source/ pixels |
|----------------|--|--|---|--|---|
| Steel gauge | 7.04 | 314 | 316.982 | 430 | 429.743 |
| Steel gauge | 9.97 | 446 | 446.448 | 648 | 646.875 |
| Steel gauge | 13.85 | 622 | 620.643 | 923 | 926.343 |
| Silicon window | 6.94 | 894 | 892.301 | 1029 | 1026.723 |

As seen in table 4.2, the secondary source of 3.8 mm in diameter located 6 mm in front of the primary focal spot was used in the calculations. Data presented in table 4.3 shows that the experimentally measured values of image sizes produced by primary and secondary radiation sources were in good agreement with the values calculated using equations (87)-(96).

4.3.4 Analysis of 2D simulated images

Having acquired numerical evidence to support the initial postulate about the size and the location of the secondary source, a computer simulation study was conducted for further investigations. During this study a number of 2D images of spheres of different sizes, materials and magnification settings were acquired on the XCT system; the images were then compared with relevant simulated 2D images. For example, figure 4.11a shows a simulated image of an iron sphere of 6.36 mm in diameter with magnification set to 9 and other parameters as per table 4.2. Adjusting the image contrast allows the effects of the secondary radiation to be clearly visible (figures 4.11b and 4.11c). (The 'dark core' inside the

sphere image is the product of individual images of the sphere, produced by multiple secondary focal spots around the exiting window, overlapping each other). For a given size of secondary source, the presence of the 'dark core' depends on the size and magnification of the sphere. The simulated image is in close correlation with the image of a steel sphere of 6.36 mm in diameter, produced on the XCT system with the X-ray tube settings of 75 kV, 100 μ A and magnification set to 9 (figure 4.12a). Again, when the contrast of the acquired image is adjusted, the effects of off-focal radiation are clearly visible (figures 4.12b and 4.12c). The sizes of the images due to the primary source and the secondary source in both, simulated and experimental images, were calculated and are summarised in table 4.4. (Experimental images were processed in ImageJ as described in section 4.3.3)

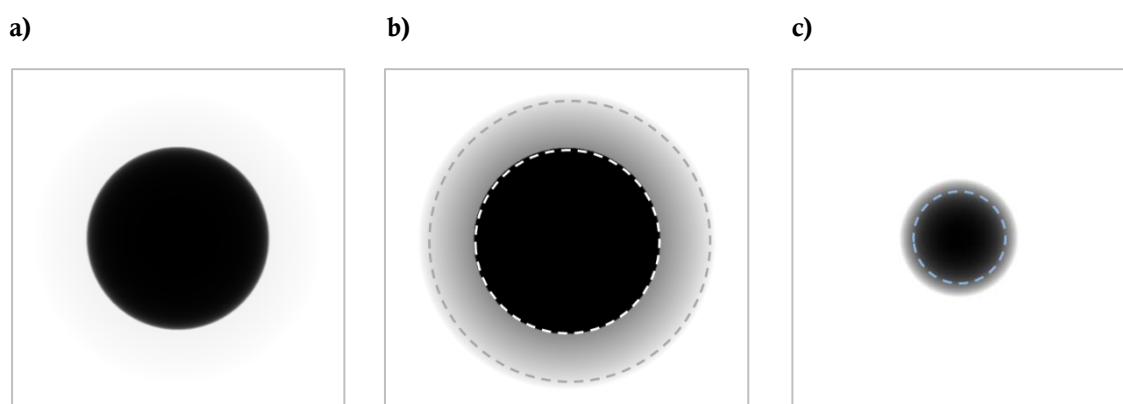


Figure 4.11 a) A simulated image of a steel sphere of 6.36 mm in diameter at magnification set to 9; b) the same image with grey values adjusted for shadow visibility, here the white dashed line shows the image due to the primary source and the grey dashed line shows the 'shadow effect' due to the secondary source; c) the same image with grey values adjusted for the 'dark core' visibility, here the blue dashed line shows the 'dark core effect' due to the to the secondary source.

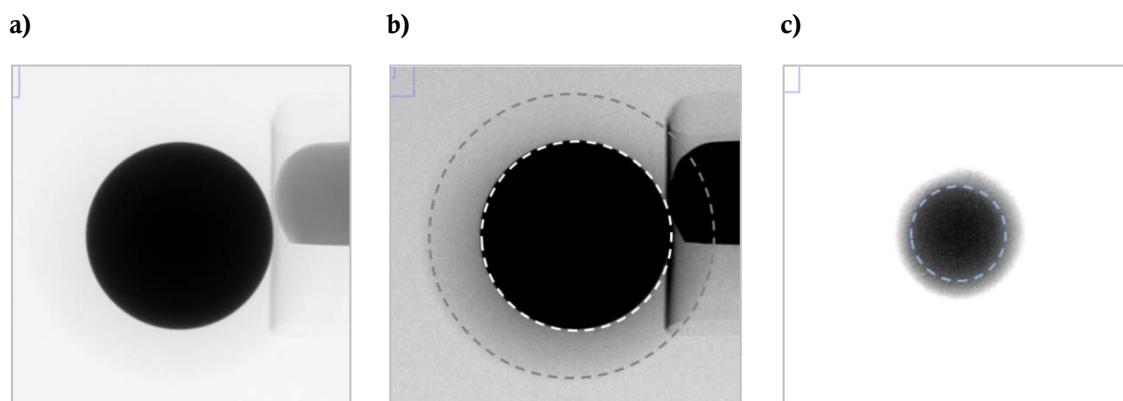


Figure 4.12 a) An image of a steel sphere of 6.36 mm in diameter, produced with the X-ray tube settings of 75 kV, 100 μ A and magnification set to 9; b) the same image with grey values adjusted for shadow visibility, here the white dashed line shows the image due to the primary source and the grey dashed line shows the 'shadow effect' due to the secondary source; c) the same image with grey values adjusted for the 'dark core' visibility, here the blue dashed line shows the 'dark core effect' due to the to the secondary source.

Table 4.4 The summary of the diameter values of images due to the primary and secondary sources in experimental and simulated images.

| | Image diameter due to the primary source/ pixels | The diameter of the shadow due to the secondary source/ pixels | The diameter of the core due to the secondary source/ pixels |
|--------------------|--|--|--|
| Experimental image | 284 | 456 | 138 |
| Simulated image | 286 | 458 | 139 |

Although some degree of approximation existed due to boundary definition in image processing, nevertheless diameter values in experimental and simulated images are in good agreement. This further confirms the initial postulate about the origin and location of the secondary source.

To summarise, the above experimental investigations in conjunction with computer simulations have confirmed the initial postulate that in the XCT system used in this study the unwanted secondary X-rays are produced by the interaction of backscattered electrons with the exiting window of the tube housing of 3.8 mm in diameter located around 6 mm in front of the primary focal spot. The investigations of the effects of secondary radiation on 2D images have shown clearly that secondary radiation can affect the background around the imaged object, the edges of the object, as well as the internal parts of the object. The exact impact on the quality of 2D images would depend on multiple factors, e.g. the size, shape and location of the secondary radiation source, the material and geometry of the scanned object, the magnification, the positioning of the object on the rotation stage and the tube power settings.

4.3.5 Analysis of 3D volumes

Experimental scan

The next stage of the study was to analyse the effects of secondary radiation on reconstructed 3D volumes of scanned objects. A steel sphere of 5 mm in diameter was scanned on the XCT system with the X-ray tube set to 100 kV and 100 μ A and the magnification set to 10. As expected, all 2D images were affected by the presence of secondary radiation (figure 4.13). The stack of 2D images was then reconstructed using Nikon CT Pro 3D software and the 3D volume was analysed in VG Studio (figure 4.14). The diameter of the sphere was calculated to be 4.993 mm with form error of 6.652 μ m.

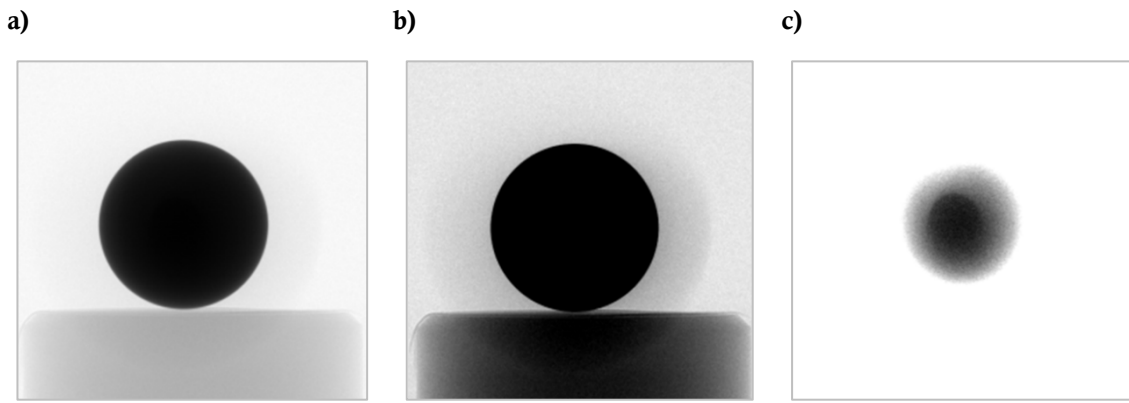


Figure 4.13 a) An image of a steel sphere of 5 mm in diameter, produced with X-ray tube settings of 100 kV, 100 μ A and magnification set to 10; b) the same image with grey values adjusted for shadow visibility; c) the same image with grey values adjusted for 'dark core' visibility.

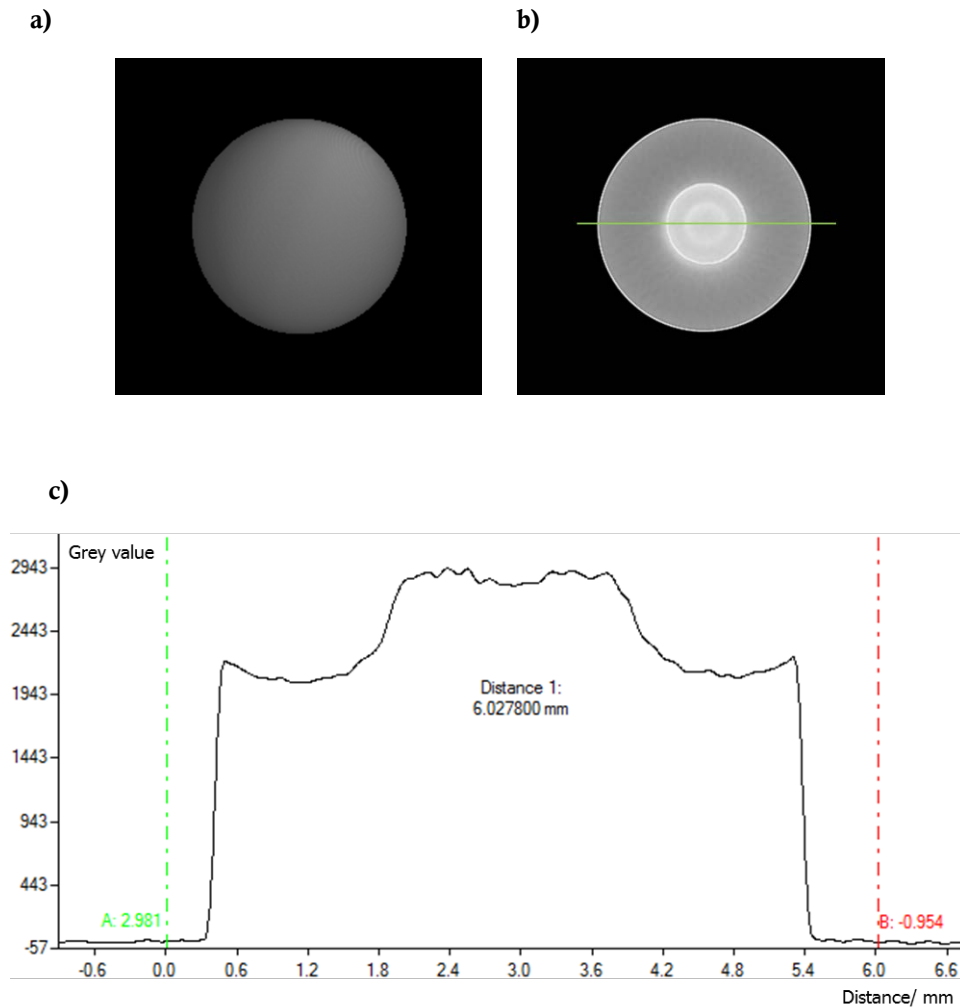


Figure 4.14 a) A 3D volume of a steel sphere of 5 mm in diameter; b) a 2D slice through the 3D volume with surfaces fitted to the outer boundary and the inner 'pseudo-boundary' inside the sphere; a profile through the centre of the 2D slice is marked in green; c) grey level values along the profile line.

The analysis of the reconstructed 3D volume of the sphere shows that the shadow effect observed in 2D images appears to have little influence on the outer boundary of the 3D volume. On the other hand, the presence of the dark core in 2D images appears to have a significant effect inside the 3D volume, as it causes an additional pseudo-surface being determined inside the reconstructed sphere (figures 4.14b and 4.14c). These observations confirm that the 2D image artefacts caused by the presence of the secondary source can have a negative effect on the reconstructed 3D models and can lead to diminished contrast-to-noise ratio as well as errors in material analysis.

Simulated two-sphere objects

In order to assess the influence of the secondary source on dimensional measurement, a number of 2D image stacks with different sphere arrangements were simulated:

- 1) the first arrangement was of two iron spheres of 2 mm in diameter each with a 2 mm distance between their centres, with magnification set to 10;
- 2) the second arrangement was of two iron spheres of 4 mm in diameter each with a 5 mm distance between their centres, with magnification set to 10;
- 3) the third arrangement was of two iron spheres of 5 mm in diameter each, with a 6 mm distance between their centres, with magnification set to 15.

Two simulated image stacks were produced for each arrangement: stack one was simulated using only the primary source and stack two was simulated using the primary and secondary sources. The measurement results are summarised in table 4.5.

As an example, figure 4.15a shows a 2D image of two iron spheres of 4 mm in diameter, with a 5 mm distance between their centres, with magnification set to 10, simulated using both the primary and secondary sources. In images simulated using both sources, the effects of off-focal radiation are clearly visible (figure 4.15b). The analysis of the 3D reconstructed volumes produced with and without the secondary source (figures 4.15c and 4.15d, respectively) shows that although the presence of off-focal radiation changes the grey level values of the background and inside the sphere (figure 4.15e), the diameter, form error and uni-directional and bi-directional distance measurements appears to be largely unaffected. The results of the diameter and form error measurements of two-sphere objects are summarised in table 4.5.

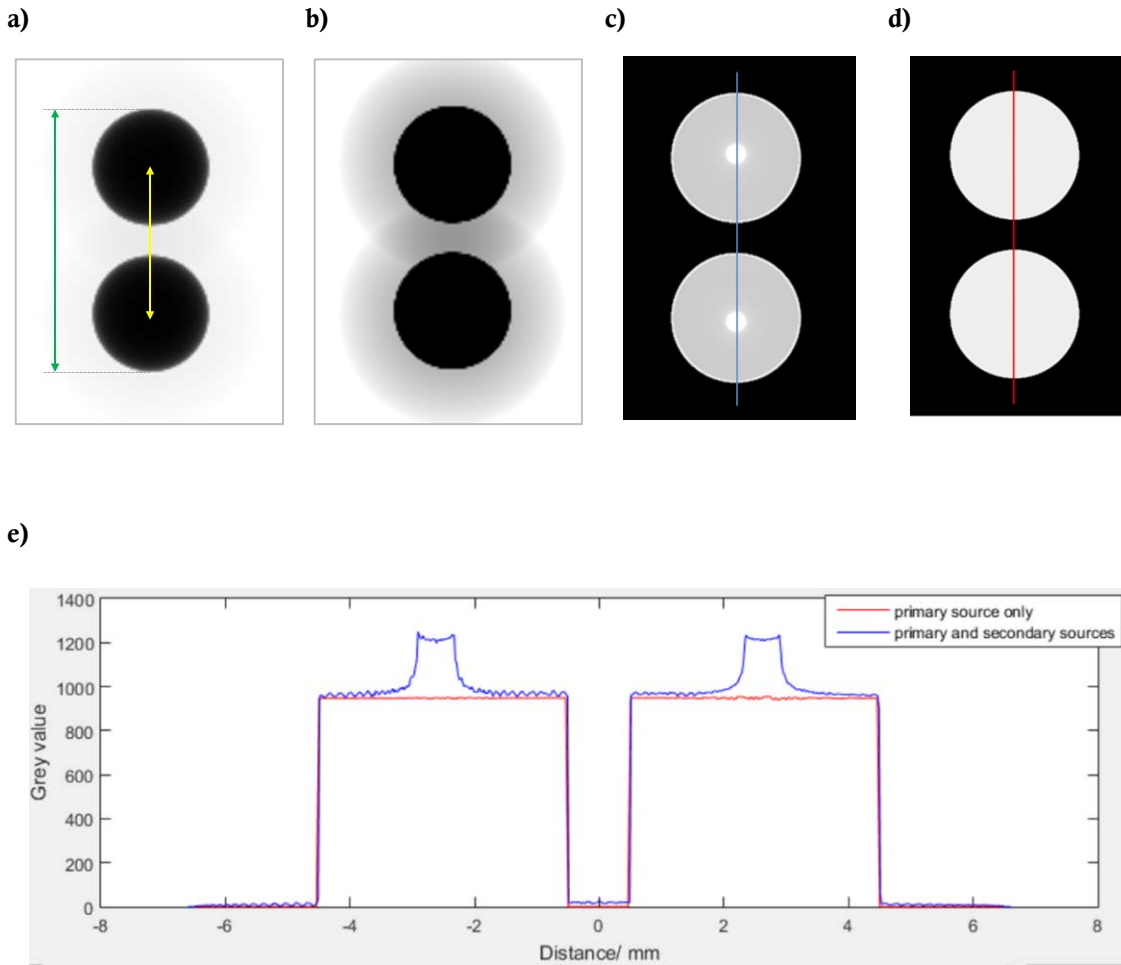


Figure 4.15 A simulation of two iron spheres of 4 mm in diameter each, with a 5 mm distance between their centres and magnification set to 10, where a) is a 2D image from the stack simulated using the primary and secondary sources (the yellow arrow shows a uni-directional distance and the green arrow shows a bi-directional distance); b) is the same image with grey values adjusted for shadow visibility; c) is a 2D slice through the 3D volume reconstructed from the 2D image stack simulated using the primary and secondary sources (the appearance of pseudo-objects inside the spheres is clearly visible), (a profile through the centre of the 2D slice is marked in blue); d) is a 2D slice through the 3D volume reconstructed from the 2D image stack simulated using the primary source only (a profile through the centre of the 2D slice is marked in red); e) grey level values along the profiles marked by the red line in d) and the blue line in c).

Table 4.5 A comparison of 3D volumes of two-sphere objects. The diameter, form error, uni-directional and bi-directional distances were measured for sphere surfaces determined using the advanced (Adv.) and automatic (ISO-50 %) surface determination techniques.

| | Simulated spheres | | | Magnifi- cation | Voxel size/ μm | Sphere 1 | | | | Sphere 2 | | | | Calculated distances/ mm | | | |
|-------------------------------|-------------------|---------------------------------|--------------------------------|--------------------|-------------------|--------------|---------|-------------------|---------|--------------|---------|----------------|---------|--------------------------|---------|----------------|---------|
| | Diameter/ mm | Uni-directional distance/ mm | Bi-directional distance/ mm | | | Diameter/ mm | | Form error/ μm | | Diameter/ mm | | Form error/ μm | | Uni-directional | | Bi-directional | |
| | | | | | | Adv. | ISO-50% | Adv. | ISO-50% | Adv. | ISO-50% | Adv. | ISO-50% | Adv. | ISO-50% | Adv. | ISO-50% |
| Primary source only | 2.000 | 2.000 | 4.000 | 10 | 20.000 | 1.998 | 2.031 | 9.246 | 12.416 | 1.998 | 2.031 | 9.250 | 15.366 | 2.000 | 2.001 | 3.998 | 3.998 |
| Primary and secondary sources | 2.000 | 2.000 | 4.000 | 10 | 20.000 | 1.998 | 1.999 | 9.493 | 9.926 | 1.998 | 1.999 | 9.483 | 9.664 | 2.000 | 2.000 | 3.998 | 3.998 |
| Primary source only | 4.000 | 5.000 | 9.000 | 10 | 20.000 | 4.001 | 4.001 | 7.189 | 7.256 | 4.001 | 4.001 | 7.174 | 7.256 | 5.001 | 5.001 | 9.002 | 9.002 |
| Primary and secondary sources | 4.000 | 5.000 | 9.000 | 10 | 20.000 | 4.001 | 4.001 | 6.947 | 6.625 | 4.001 | 4.001 | 6.525 | 6.625 | 5.001 | 5.000 | 9.001 | 9.000 |
| Primary source only | 5.000 | 6.000 | 11.000 | 15 | 13.333 | 5.001 | 5.000 | 9.308 | 9.940 | 5.001 | 5.038 | 9.167 | 14.847 | 5.999 | 5.998 | 11.018 | 11.015 |
| Primary and secondary sources | 5.000 | 6.000 | 11.000 | 15 | 13.333 | 5.001 | 5.001 | 8.626 | 9.423 | 5.001 | 5.001 | 8.593 | 9.408 | 5.999 | 5.998 | 11.012 | 11.012 |

Chapter 4

The preliminary results from the simulation of two-sphere objects suggest that although the presence of off-focal radiation degrades the quality of 2D images, the effect on the measurement of simple objects, such as spheres, is insignificant. For multi-material objects and objects with complex geometries, however, the effects of off-focal radiation can potentially contribute to errors in measurement and material analysis.

Simulated multi-material objects

In order to investigate the effects of off-focal radiation on dimensional measurement of a simple multi-material object, the following 2D image stacks were simulated and processed:

- 1) an iron sphere of 6 mm in diameter, with magnification set to 10, simulated using primary source only;
- 2) an iron sphere of 6 mm in diameter, with magnification set to 10, simulated using primary and secondary sources;
- 3) an object with an outer iron sphere of 6 mm in diameter and an inner aluminium sphere of 2.5 mm in diameter, with magnification set to 10, simulated using primary source only;
- 4) an object with an outer iron sphere of 6 mm in diameter and an inner aluminium sphere of 2.5 mm in diameter, with magnification set to 10, simulated using primary and secondary sources.

As previously, the simulations were produced using a monochromatic X-ray beam of 60 kV. The results are summarised in table 4.6.

Table 4.6 A comparison of 3D volumes of iron (Fe) and aluminium (Al) spheres. The diameter and form error of spheres were measured for surfaces determined using the advanced (Adv.) and automatic (ISO-50 %) surface determination techniques.

| | Simulated sphere diameter/ mm | Diameter/ mm | | Form error/ μm | |
|---------------------------------------|----------------------------------|--------------|---------|---------------------------|---------|
| | | Adv. | ISO-50% | Adv. | ISO-50% |
| Primary source only: | | | | | |
| -sphere material Fe | 6.000 | 6.000 | 6.000 | 14.035 | 14.268 |
| Primary and secondary sources: | | | | | |
| -sphere material Fe | 6.000 | 6.001 | 6.001 | 13.112 | 13.570 |
| -pseudo-inner sphere | | 2.726 | | 18.041 | |
| Primary source only: | | | | | |
| -outer sphere material Fe | 6.000 | 6.001 | 6.001 | 12.951 | 13.499 |
| -inner sphere material Al | 2.500 | 2.499 | | 16.061 | |
| Primary and secondary sources: | | | | | |
| -outer sphere material Fe | 6.000 | 5.999 | 5.998 | 14.181 | 14.289 |
| -inner sphere material Al | 2.500 | 2.717 | | 8.391 | |

Just as with the simulations of two-sphere objects, the measurements of the diameter and the form error of the iron sphere do not appear to be affected by the secondary source. The situation is different, however, when analysing the diameters of the inner aluminium sphere. When the object with the outer iron sphere and the inner aluminium sphere was simulated using the primary source only, the diameter of the aluminium sphere in the reconstructed 3D volume was calculated to be 2.499 mm. When this object was simulated using the primary and secondary sources, the diameter of the aluminium sphere in the reconstructed 3D volume was calculated to be 2.717 mm. The value of 2.717 mm is close to the value of 2.726 mm, which is the diameter of the pseudo-sphere identified inside the iron sphere that was simulated using the primary and secondary sources. The reason for such values becomes apparent, when analysing the profiles through the 2D slices of the three reconstructed volumes (figure 4.16): the presence of off-focal radiation distorts the real boundary between iron and aluminium materials in the object (dashed grey line), resulting in the false boundary identification (solid grey line). This finding supports the proposition that off-focal radiation can increase measurement errors for complex multi-material objects.

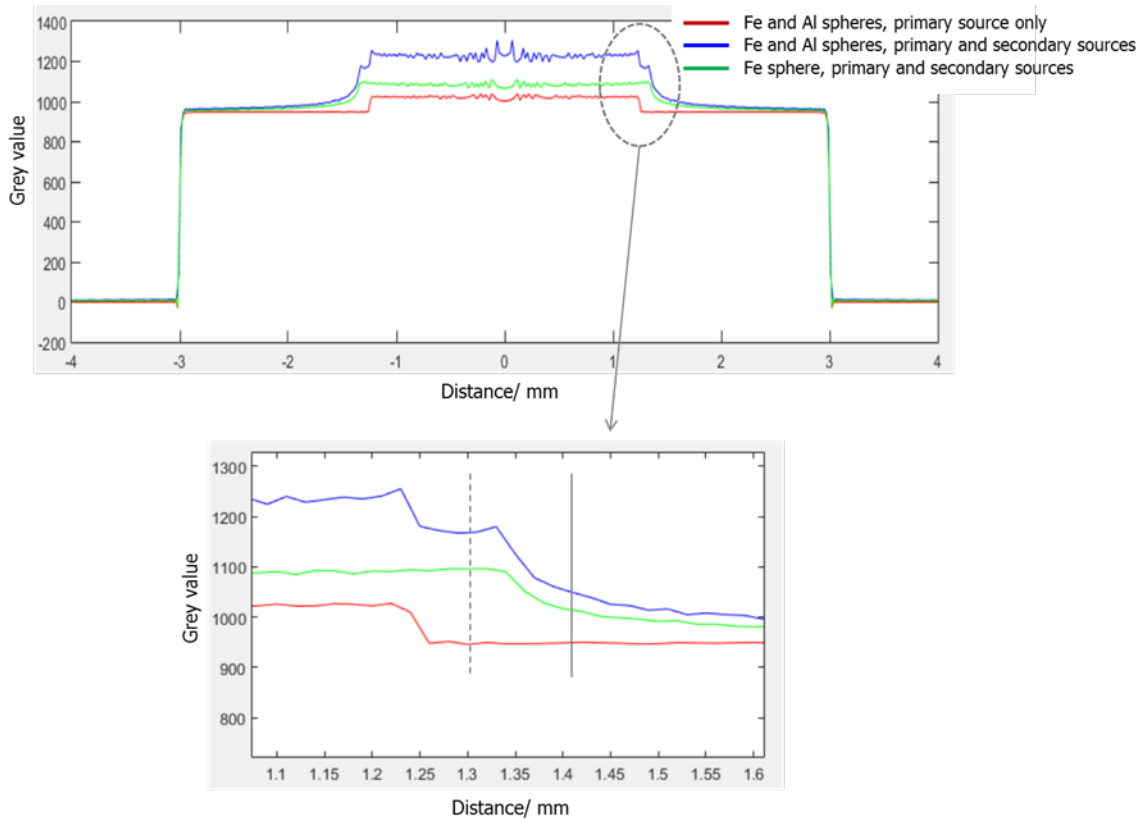


Figure 4.16 The profiles taken through the centre of the 2D slices of 3D volumes reconstructed from image stacks of: an iron sphere of 6 mm in diameter, simulated using primary and secondary sources (green profile); of an object with an outer iron sphere of 6 mm in diameter and an inner aluminium sphere of 2.5 mm in diameter, simulated using primary source only (red profile); of an object with an outer iron sphere of 6 mm in diameter and an inner aluminium sphere of 2.5 mm in diameter, simulated using primary and secondary sources (blue profile). Dashed grey line represents a position of the real iron/aluminium border and solid grey line represents a false iron/aluminium border.

4.3.6 Possible correction methods

There are a number of methods that can minimise the intensity of off-focal radiation and its effects. The first method is the hardware method in which additional (often made of lead) collimators are installed in the way of the X-ray beam, in order to stop off-focal radiation from penetrating the object. This method is particularly widespread in medical XCT, as it not only improves the image quality but most importantly reduces exposure to radiation. The presence of such collimators is often required by the health and safety standards [43].

The hardware method was applied to some of the scans produced on the XCT system at NPL. For example, figure 4.17a shows a 2D image of an object made with four crossed metal wires, scanned at X-ray tube settings of 75 kV and 100 μ A, at magnification set to 5. Figure 4.17b shows the same object scanned at the same settings but with added tungsten

aperture of 3 mm in diameter and 4 mm thickness, placed in front of the exiting window. (Such aperture was used, as it was readily available at the NPL lab). It is clear that the effects of off-focal radiation were minimised, however, the overall brightness of the image scanned with the aperture was reduced (figure 4.17c).

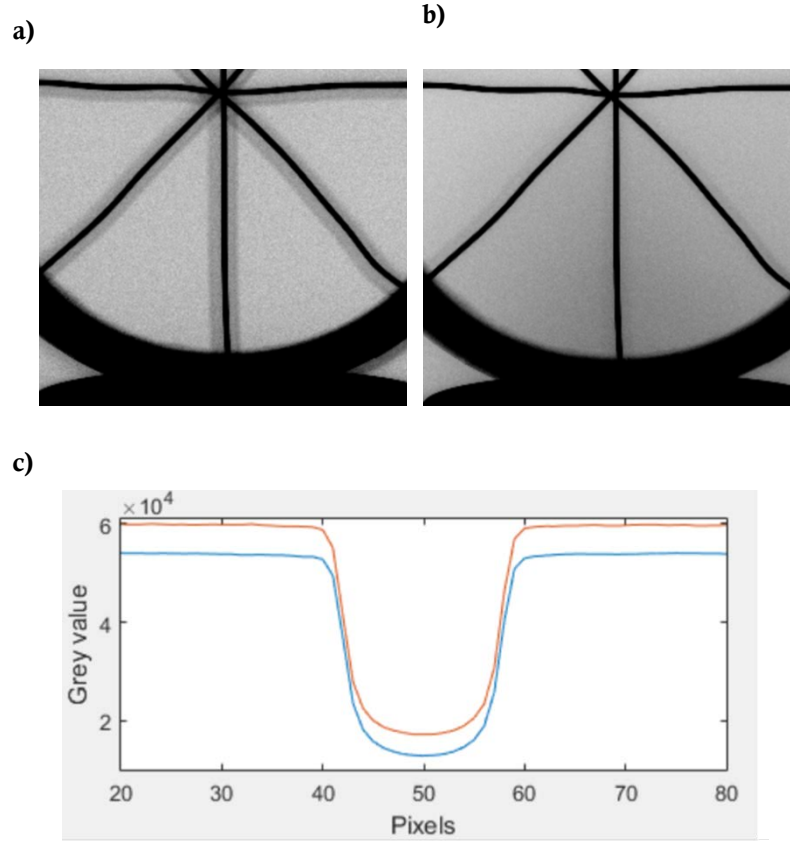


Figure 4.17 An image of the object made with four crossed metal wires, scanned at X-ray tube settings of 75 kV and 100 μ A, at magnification set to 5; b) an image of the same object with the same settings scanned using a tungsten aperture of 3 mm in diameter and 4 mm thickness and c) a comparison of the profiles taken through one of the wires in image (a) (red) and image (b) (blue).

One strong disadvantage of the hardware method for XCT systems used in dimensional metrology is the reduction of the field of view, which can negatively affect the system's scanning versatility. Therefore, it is recommended that the user, equipped with information about the system's secondary source properties, considers whether the use of additional collimating devices is beneficial for a given scanning task.

Another method of dealing with the unwanted effects of off-focal radiation is the software method. This method is based on the assumption that each 2D image is a combination of images due to the primary and secondary sources. The aim of the software method, therefore, is to eliminate the image due to the secondary source from each 2D image [111]. Although the software correction of individual 2D images can minimise the effects of off-

focal radiation (and can easily be achieved for simulated images), this method has a number of limitations. For example, in order to remove the effect completely, the exact position of the secondary source needs to be known. As shown in this study, a good estimate of the secondary source size and position can be achieved; however, some degree of approximation is always present. As stated previously, the intensity of the images due to the secondary source depends on a number of factors, such as the tube settings, object materials and geometry, magnification settings, positioning of the object on the rotation stage, the motion of the rotation stage, focal spot drift, etc. An exact knowledge of these factors is essential in order to eliminate the effects of off-focal radiation completely, but often impossible to obtain. In addition, the secondary images of structures outside the field of view, e.g. the rotation stage, object holders, etc. can interfere with the imaging of objects inside the field of view.

A third method of minimising the effect of off-focal radiation is through adjusting the design of the X-ray tube and tube housing in particular. Since the secondary radiation is generated by the interaction of backscattered electrons with the housing material, it is proposed that the inner part of the housing close to the exiting window is shielded with a soft material, such as aluminium. Aluminium is often a material of choice in beta-particle²⁵ shielding. The maximum range, R_{max} of a beta particle can be calculated using an empirical formula given by Katz and Penfold [139]

$$R_{max} = 0.412E_{\beta}^{1.265-0.0954 \ln(E_{\beta})} \text{ for } 0.01 \leq E_{\beta} \leq 2.5 \text{ MeV}, \quad (97)$$

where E_{β} is the maximum beta energy in MeV and R_{max} is in gcm^{-2} . With the maximum range known, the thickness t of the shielding can be calculated using

$$t = \frac{R_{max}}{\rho}, \quad (98)$$

where ρ is the material density in gcm^{-3} . The highest energy an electron can acquire in the XCT system at NPL is 225 keV and, therefore, can be stopped by a sheet of aluminium of 0.187 mm in thickness. In other words, if a layer of aluminium of, say, 0.2 mm is fitted inside the tube housing around the exiting window, none of the backscattered electrons will be able to reach the tungsten/alloy part of the housing to produce highly energetic X-rays. The fraction of electron energy reappearing as bremsstrahlung can be calculated using

²⁵ Beta-particles are high-energy, high-speed electrons or positrons emitted in the radioactive decay of an atomic nucleus.

$$f = 3.5 \times 10^{-4} Z E_{\beta} , \quad (99)$$

where E_{β} is the maximum electron energy in MeV. For electron energy of 225 keV impinging on an aluminium sheet with $Z = 13$, this fraction is around 0.001, which is almost six times smaller than for tungsten. The proposition of shielding the inner part of the housing close to the exiting window with soft material, such as aluminium, was presented to the manufacturer. Trials are underway to examine the possibility of changing the tube design. Since the number of backscattered electrons increases rapidly with the increased angle between the incoming electron beam and the target material, it is also possible to reduce backscatter by changing the tilt angle. Again, this suggestion was presented to the manufacturer.

4.3.7 Secondary source evaluation procedure

The results of the NPL study of off-focal radiation in micro-focus XCT systems designed for dimensional metrology suggest that this phenomenon can be present in all systems, the extent of which varies depending on the system's design. The study confirmed that the effects of off-focal radiation can degrade the image quality and cause errors in dimensional measurements and material analysis. It is therefore recommended to include the evaluation of the properties of the secondary source, e.g. location, size, shape and intensity, as a part of the overall X-ray probe qualification procedure.

The procedure can be based on the techniques developed during this study, as it was clearly demonstrated that the analysis of 2D images of objects such as a steel gauge, silicon disk and metal spheres can be successfully employed in calculating the location, size and shape of the secondary source in micro-focus XCT systems. In addition, in order to evaluate the radial non-uniformity of the intensity due to the secondary source, a novel object, named 'the wheel', was designed. This object was made with four crossed steel rods fixed inside an aluminium cylinder (figure 4.18). The diameter of the rods is 0.9 mm and the inner diameter of the cylinder is 78 mm. The benefit of the wheel is that on scanning, the user can quickly identify the pattern of intensity non-uniformity due to secondary source. For example, when the wheel was scanned on the XCT system at NPL, the non-uniformity of the image due to secondary radiation suggested that in this system, the lower part of the secondary source produces the least amount of unwanted X-rays.

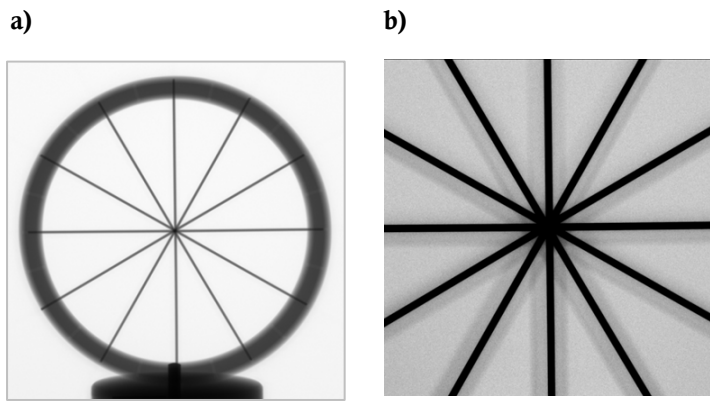


Figure 4.18 An image of the wheel scanned at X-ray tube settings of 120 kV and 80 μ A, at magnification set to 4; b) an image of the wheel, scanned at the same X-ray tube settings and magnification set to 10, with adjusted contrast for secondary image visibility.

It is also suggested that the qualification procedure should include computer simulations, as described in this study, in order to verify the secondary source properties calculated using image magnification geometry.

4.4 Conclusions and future work

The novel study of the effects of off-focal radiation on image quality and dimensional measurement in micro-focus XCT systems was conducted at NPL. Based on the study the following conclusions can be made:

- 1) The effects of off-focal radiation were evident in many 2D images, as well as in reconstructed 3D models.
- 2) The position, size and shape of the secondary source were successfully calculated using the techniques developed in this study, which include the design of a novel test object.
- 3) The evaluation of 2D simulated and experimental images showed that the presence of secondary radiation can affect the background around the imaged object, the edges of the object, as well as the internal parts of the object.
- 4) The comparison of the reconstructed 3D models of different sphere arrangements, simulated using primary source only and primary and secondary sources, has shown that the presence of off-focal radiation does not appear to affect the dimensional measurement of uni-material objects with simple geometry. On the other hand, the presence of the secondary source can cause significant errors in material analysis and dimensional measurement of multi-material objects.
- 5) A number of ways to minimise the effects of off-focal radiation were presented.
- 6) Based on the findings of this study, it is recommended that the evaluation of the properties of the secondary source, such as its location, size, shape and intensity, is included as a part of the overall qualification procedure of the X-ray probe.
- 7) Further research should include the investigation of the effects of off-focal radiation on dimensional measurement of multi-material objects of complex geometries, as well as further advancement of software correction methods.

Novelty and contribution: first of a kind study that addresses the issue of off-focal radiation in industrial micro-focus XCT systems and its relation to dimensional measurement, bringing the issue to the attention of wider scientific community. The study includes a novel analysis of the effects of off-focal radiation on image quality, dimensional measurement and material analysis. Solid evidence was acquired to support the proposition that the evaluation of the properties of the secondary source needs to be included in the overall qualification procedure of the X-ray probe.

Chapter 5: An initial computer simulation study investigating the effects of the focal spot size and shape on dimensional measurement in cone-beam micro-focus XCT systems

5.1 Background to the study

Apart from the positional stability of the focal spot and the effects of off-focal radiation (already discussed in this thesis), other characteristics associated with the X-ray probe are the size and shape of the focal spot. The knowledge of these parameters is essential as they can affect image quality and material analysis. The size of the focal spot²⁶ has a direct influence on the sharpness (or blurring) of the image due to the penumbra effect, often termed edge gradient (figure 5.1). Penumbra is defined as the region of partial illumination that surrounds the umbra or complete shadow [91].

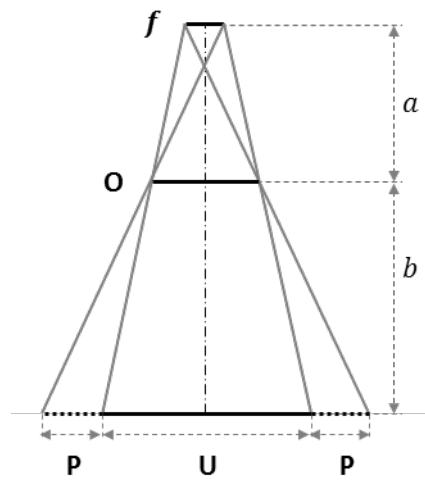


Figure 5.1 Schematic representation of the penumbra effect due to an extended focal spot. Here, O is the size of the object, f is the size of the extended source, U is the umbra, P is the penumbra, a is the source-to-object distance and b is the object-to-detector distance.

The size of the penumbra P is the function of the size of the focal spot f , the source-to-object distance a and object-to-detector distance b , where

²⁶ Here, the focal spot size is referred to the 'effective focal spot size', discussed in section 2.4.3.

$$P = f \times \frac{b}{a}. \quad (100)$$

At high magnification settings the size of the focal spot is the main parameter limiting the spatial resolution of an XCT system [40].

There are a number of standards which provide instructions on how to measure focal spot sizes in XCT systems used in the field of non-destructive testing [48]–[52], [140]. At present no such standards exist for XCT systems used in dimensional metrology, however discussion on measurement of the focal spot size in micro-focus XCT can be found in literature [61], [62], [141]. As stated in section 2.4.3, the size of the focal spot depends on a number of factors, such as geometry of the filament, the X-ray tube voltage and current settings, focusing optics and the angle between the incoming electron beam and the anode. In most medical XCT systems, the filament is a tungsten coil of a few millimetres in length, producing focal spot sizes between 0.1 mm and 7 mm of rectangular shape [89]; therefore, the standard requires to state the size of the focal spot in terms of its length and width [46]. In micro-focus XCT systems with reflection targets used in dimensional metrology, the filament is a thin tungsten wire, where electrons are emitted from its tip only; this produces focal spots of around 3 μm to 100 μm in size which are elliptical in shape [142]. The exact dimensions of the ellipse would depend on the diameter of the electron beam and the angle between the incoming electron beam and the target (a ‘line-focus principle’ discussed in section 2.4.3).

A number of studies investigated the effects of the X-ray tube voltage and current settings on the size of the focal spot, as well as the effects of the focal spot size on image quality and spatial resolution are presented in [62], [132], [143]–[146]. At present no studies specifically discussing the impact of the focal spot size and shape on dimensional measurement using XCT have been identified. An exploratory computer simulation study, with the purpose of investigating the influence of the size and shape of the focal spot on dimensional measurement, was conducted at NPL. The results of the study can be informative in evaluating whether the measurement of the focal spot size and shape need to be included in the X-ray probe characterisation procedure for metrological XCT systems.

5.2 Methodology

5.2.1 Computer simulations of different focal spot sizes

In order to assess the influence of the focal spot size on dimensional measurement, a number of 2D image stacks of an iron sphere of 1 mm in diameter were simulated using seven different focal spot sizes between 0 μm (a point source) to 96 μm , at two magnification settings of 80 and 40. This range of sizes is representative of focal spot sizes in micro-focus XCT systems [142]. Simulations of 2D images were performed in Matlab using the code described in section 3.2.3 parts 1-6 with adjusted magnification values. Focal spots were represented as 90 ‘individual point sources’ placed within a circle area of different diameters. Out of 90 points, 30 points were generated in a regular pattern around the perimeter of the circle in order to define a clear boundary of the focal spot. A further 60 points were generated inside the area. This limited number of points inside the area was due to computational and time constraints (figure 5.2). (Due to the limited number of points and the random nature of their position some non-uniformity within 2D images was expected). The stacks were reconstructed using Nikon CT Pro 3D software. The reconstructed 3D volumes of spheres were analysed using VG Studio software as described in section 4.2.3. The diameter and the form error of 3D sphere models simulated using different focal spot sizes were measured and compared.

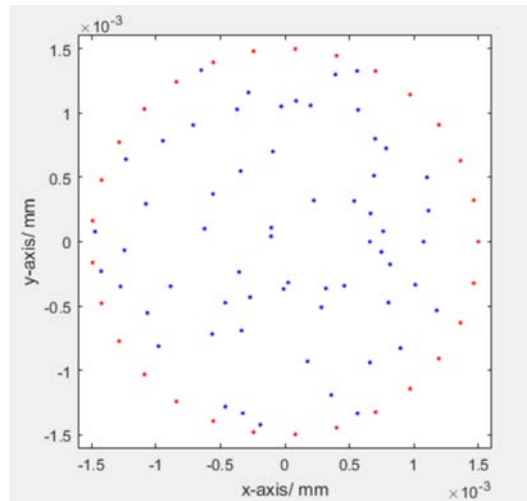


Figure 5.2 A representation of the focal spot of 3 μm in diameter. 90 ‘individual point sources’ are distributed within a circular area: with 30 points generated in a regular pattern around the perimeter and additional 60 points generated randomly within the area.

5.2.2 Computer simulations of different focal spot shapes

In order to assess the influence of the focal spot shape on dimensional measurement, a number of 2D image stacks of the iron sphere of 1 mm in diameter were simulated using rectangular and elliptical shapes of the focal spot. (These shapes are representative of focal spot shapes in real XCT systems). The rectangular focal spot was represented as 120 ‘individual point sources’ placed within a rectangle: with 60 points generated in a regular pattern around the perimeter of the rectangle and an additional 60 points generated randomly within the area of the rectangle (figure 5.3). The size of the longer side of the rectangle varied between 3 μm to 96 μm and was always twice the size of the shorter side. The rectangular focal spot was simulated first with its longer side along the x -axis and then along the y -axis. The elliptical focal spot was represented as 120 ‘individual point sources’ placed within an ellipse: with 60 points generated in a regular pattern around the perimeter of the ellipse and an additional 60 points generated randomly within the area of the ellipse (figure 5.4). The size of the major axis of the ellipse varied between 6 μm to 96 μm ; the minor axis was calculated as (major axis $\times \sin(20^\circ)$). The value of 20° was chosen as it approximates a possible angle value in a real X-ray tube. The elliptical focal spot was simulated with its major axis first along the x -axis and then along the y -axis. Magnification of 80 and 40 was used in the simulations. All stacks were then reconstructed and analysed as described in section 5.2.1. The diameter and the form error of 3D sphere models simulated using rectangular, elliptical and circular focal spots were measured and compared.

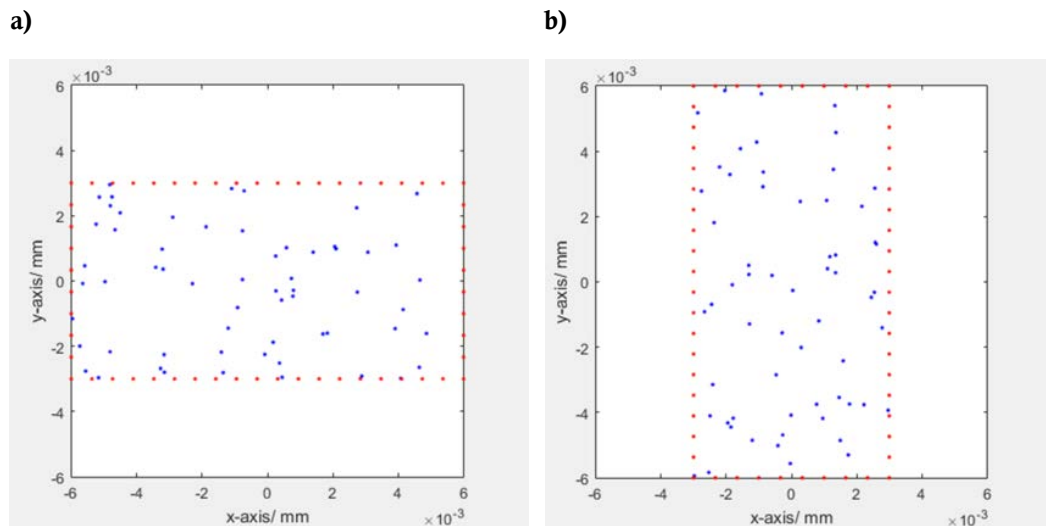


Figure 5.3 A representation of the rectangular focal spot with its longer side of 6 μm a) along the x -axis and b) along the y -axis. 120 ‘individual point sources’ are distributed within a rectangular area: with 60 points generated in a regular pattern around the perimeter and additional 60 points generated randomly within the area.

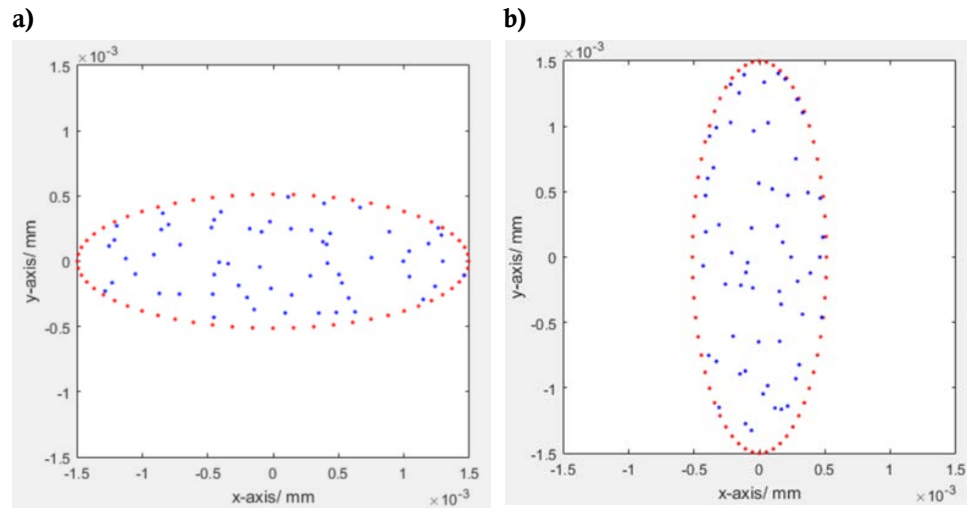


Figure 5.4 A representation of the elliptical focal spot with its major axis of $6\text{ }\mu\text{m}$ a) along the x -axis and b) along the y -axis. 120 ‘individual point sources’ are distributed within a rectangular area: with 60 points generated in a regular pattern around the perimeter and additional 60 points generated randomly within the area.

5.3 Results and discussion

5.3.1 Computer simulations of different focal spot sizes

The analysis of 2D images of spheres simulated using different focal spot sizes demonstrates that the increase of the focal spot size increases the penumbra effect, thus increasing the image blurring (figure 5.5a-b). Increased blurring in 2D images affects thresholding in 3D volumes (5.5c-d) by shifting the position of highest grey value gradient and introducing errors in measurement.

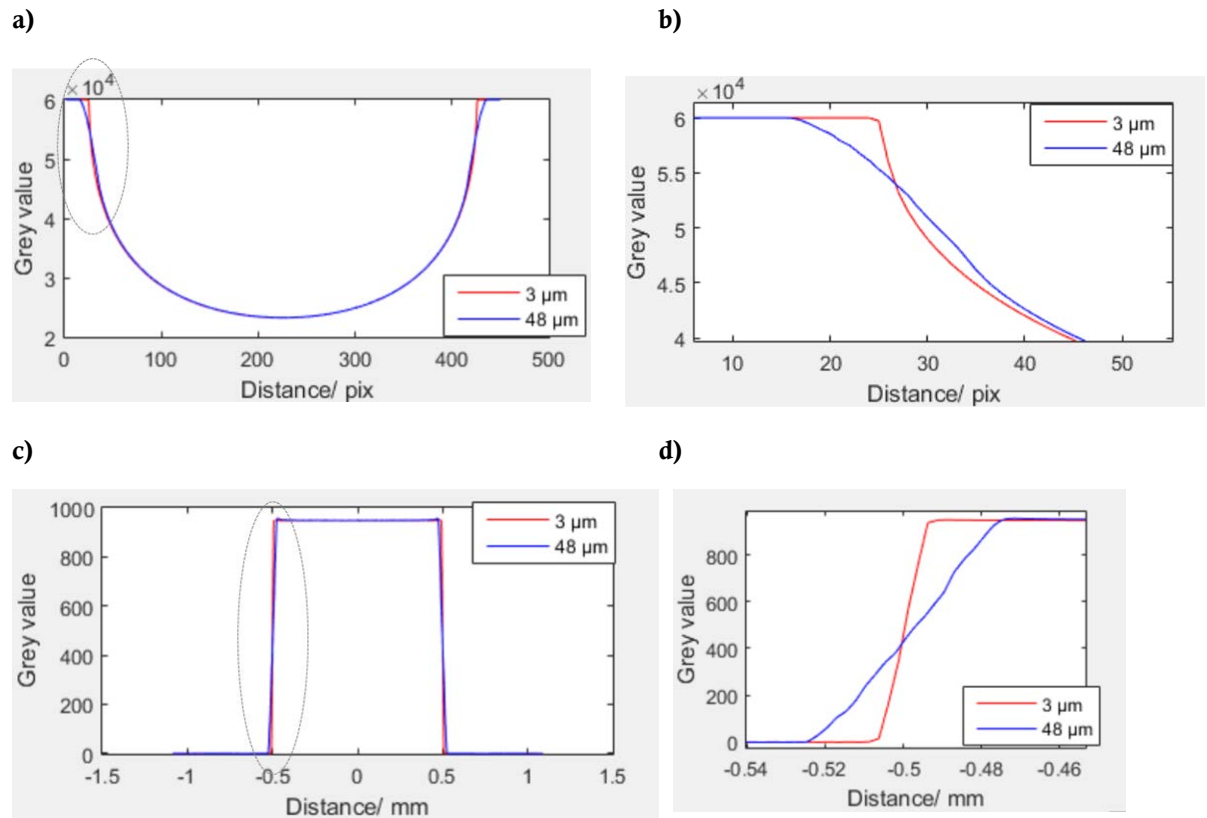


Figure 5.5 a) A profile through the central row of pixels in a 2D image of a sphere simulated using focal spot sizes of 3 μm (red) and 48 μm (blue); b) magnified view of the part of profile inside the area marked by the dotted line in a); c) A profile through the central row of pixels in a 2D slice through the 3D volume of the reconstructed sphere; d) magnified view of the part of profile inside the area marked by the dotted line in c).

The results of the diameter and the form error measurements in 3D sphere models simulated using different sizes of the focal spots with magnification set to 80 are summarised in table 5.1 and with magnification set to 40 are summarised in table 5.2. The graphic representation of the relationship between the size of the focal spot and the diameter measurements is presented in figure 5.5.

Table 5.1 The results of the diameter and the form error measurements of 3D sphere models simulated using different focal spot sizes with magnification set to 80. The voxel size is 2.5 μm .

| Focal spot size/ μm | Diameter of reconstructed sphere/ mm | | Form error of reconstructed sphere/ μm | |
|--------------------------------|--------------------------------------|---------|---|---------|
| | Adv. | ISO-50% | Adv. | ISO-50% |
| 0 | 0.9999 | 0.9999 | 1.067 | 1.062 |
| 3 | 0.9996 | 0.9996 | 0.587 | 0.545 |
| 6 | 0.9999 | 0.9999 | 0.452 | 0.436 |
| 12 | 0.9996 | 0.9996 | 0.452 | 0.669 |
| 24 | 0.9978 | 0.9988 | 1.815 | 0.786 |
| 48 | 0.9947 | 0.9961 | 3.201 | 1.390 |
| 96 | 0.9863 | 0.9873 | 7.431 | 3.286 |

Table 5.2 The results of the diameter and the form error measurements of 3D sphere models simulated using different focal spot sizes with magnification set to 40. The voxel size is 5 μm .

| Focal spot size/ μm | Diameter of reconstructed sphere/ mm | | Form error of reconstructed sphere/ μm | |
|--------------------------------|--------------------------------------|---------|---|---------|
| | Adv. | ISO-50% | Adv. | ISO-50% |
| 0 | 1.0003 | 1.0003 | 1.865 | 1.713 |
| 6 | 1.0001 | 1.0001 | 0.704 | 0.662 |
| 24 | 0.9990 | 0.9991 | 0.611 | 0.574 |
| 96 | 0.9866 | 0.9882 | 7.35 | 2.514 |

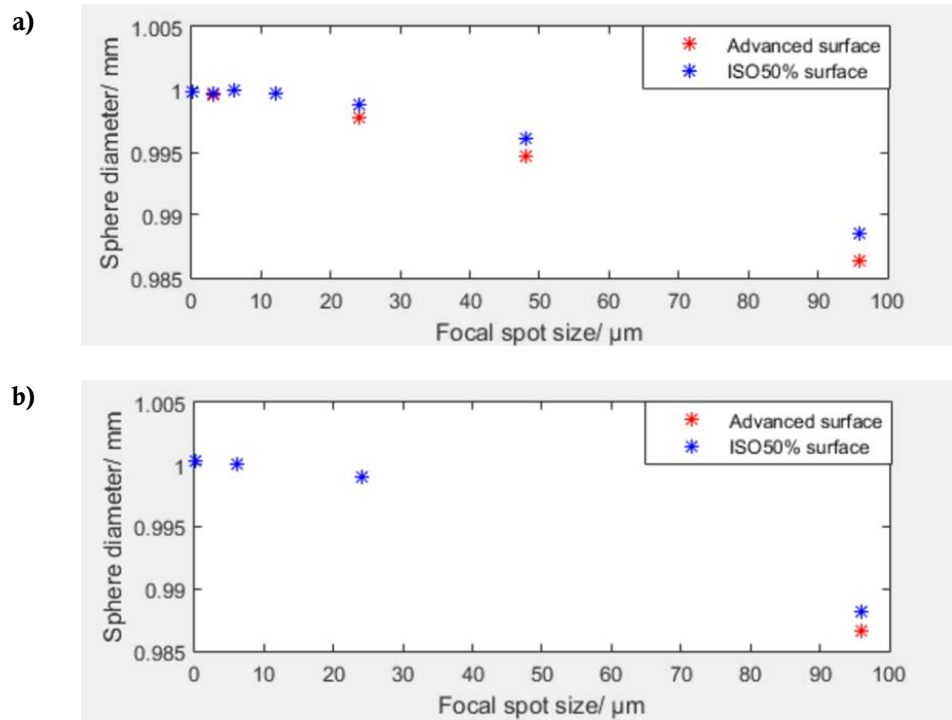


Figure 5.6 A relationship between the size of the focal spot and the diameter measurements of 3D sphere models, where sphere surfaces were determined using both the advanced method and ISO-50 %, simulated with a) magnification set to 80 and b) magnification set to 40.

The results displayed in tables 5.1 and 5.2 confirm that the size of the focal spot has a direct influence on the size and form measurement (some differences in values exist for different surface determination techniques). It can be seen that with increasing focal spot sizes the diameter of the reconstructed sphere appears to decrease (figure 5.6). For larger focal spot sizes the error in diameter measurement can exceed the size of the voxel. As expected, this tendency is more pronounced at higher magnification. The results show that compared to the sphere simulated using a point source the form error measurement initially decreases for spheres simulated using focal spot sizes between 3 μm to 24 μm before it starts to increase for focal spot sizes above 48 μm . It is possible that this pattern is due to the number of 'point sources' used to simulate each focal spot size. It is therefore recommended to conduct a sensitivity study which evaluates the relationship between the number of points used for each focal spot simulation and the resultant form error measurement.

5.3.2 Computer simulations of different focal spot shapes

The results of the diameter and the form error measurements of 3D sphere models simulated using circular, elliptical and rectangular focal spots with magnification set to 80 are summarised in table 5.3 and table 5.4, respectively. The graphic representation of the

relationship between the shape of the focal spot and the diameter measurements is presented in figure 5.7.

Table 5.3 The results of the diameter measurements of 3D sphere models simulated using circular, elliptical and rectangular focal spots with magnification set to 80. The voxel size is 2.5 μm . The advanced surface determination method was used. Here, Ellipse1 is an elliptical focal spot with its major axis along the x -axis, Ellipse2 is an elliptical focal spot with its major axis along the y -axis, Rect1 is a rectangular focal spot with its longer side along the x -axis and Rect2 is a rectangular focal spot with its longer side along the y -axis.

| Focal spot size/ μm | Diameter of reconstructed sphere/ mm | | | | |
|--------------------------------|--------------------------------------|----------|----------|--------|--------|
| | Circle | Ellipse1 | Ellipse2 | Rect1 | Rect2 |
| 0 | 0.9999 | 0.9999 | 0.9999 | 0.9999 | 0.9999 |
| 3 | 0.9996 | 1.0001 | 1.0002 | 0.9999 | 1.0002 |
| 12 | 0.9996 | 0.9997 | 0.9998 | 0.9997 | 0.9998 |
| 48 | 0.9947 | 0.9963 | 0.9968 | 0.9964 | 0.9961 |
| 96 | 0.9863 | 0.9903 | - | 0.9865 | - |

Table 5.4 The results of the form error measurements of 3D sphere models simulated using circular, elliptical and rectangular focal spots with magnification set to 80. The voxel size is 2.5 μm . The advanced surface determination method was used. Here, Ellipse1 is an elliptical focal spot with its major axis along the x -axis, Ellipse2 is an elliptical focal spot with its major axis along the y -axis, Rect1 is a rectangular focal spot with its longer side along the x -axis and Rect2 is a rectangular focal spot with its longer side along the y -axis.

| Focal spot size/ μm | Form error of reconstructed sphere/ μm | | | | |
|--------------------------------|---|----------|----------|-------|-------|
| | Circle | Ellipse1 | Ellipse2 | Rect1 | Rect2 |
| 0 | 1.067 | 1.067 | 1.067 | 1.067 | 1.067 |
| 3 | 0.587 | 0.338 | 0.613 | 0.339 | 0.645 |
| 12 | 0.452 | 0.459 | 0.457 | 0.223 | 0.334 |
| 48 | 3.201 | 1.758 | 1.545 | 2.985 | 5.773 |
| 96 | 7.431 | 2.265 | - | 6.906 | - |

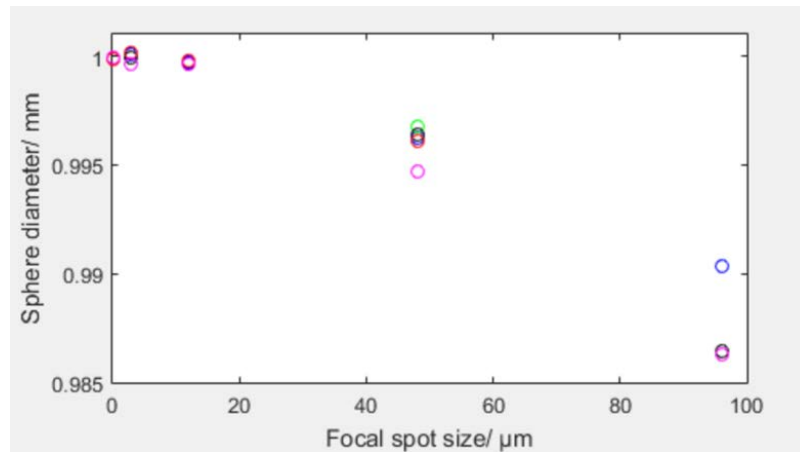


Figure 5.7 A relationship between focal spot shapes and diameter measurements of 3D sphere models. Sphere surfaces were determined using the advanced method. Colour coding is as follows: blue - elliptical focal spot with its major axis along the x -axis; green - elliptical focal spot with its major axis along the y -axis; black - rectangular focal spot with its larger side along the x -axis; red - rectangular focal spot with its larger side along the y -axis and magenta - circular focal spot.

The values displayed in tables 5.3 and 5.4 demonstrate that for a given focal spot size, changing the focal spot shape can produce different diameter and form error measurement values. As discussed in section 5.3.1, these results can be explained by the fact that different focal spot shapes cause variations in blurring effect in 2D images, thus affecting the thresholding in 3D sphere models and resulting in different measurement values. Data in table 5.3 shows that for all simulated focal spot shapes, increasing the size of the focal spot decreases the diameter of the reconstructed sphere. For larger focal spot sizes the error in diameter measurement can exceed the size of the voxel. The results also show that for all focal spot shapes the form error measurement initially decreases for spheres simulated using focal spot sizes between $3\ \mu\text{m}$ to $24\ \mu\text{m}$ before it starts to increase for focal spot sizes above $48\ \mu\text{m}$. This effect can be further studied in the previously proposed sensitivity study.

5.4 Conclusions and future work

The exploratory simulation study examining the effect of focal spot size and shape on dimensional measurement was conducted at NPL. The results clearly demonstrate that both the size and the shape of the focal spot affect the diameter and form error measurements of 3D sphere models:

- an increase in the size of the focal spot appears to lead to an decrease in diameter values and an increase in the form error values of the 3D sphere models, with measurement error reaching the value of a few voxels for larger focal spot sizes;
- for a given size of the focal spot, changing the focal spot shape can produce different diameter and form error measurement results.

It is important to mention that although this simulation study clearly shows the influence of the focal spot size and shape on dimensional measurement, the evaluation of the impact of the focal spot size and shape on dimensional measurement in real XCT scans is not a trivial matter. In order to achieve a greater confidence in the measurement results, it is suggested that the user evaluates and records how different X-ray tube settings in their XCT system affect the size and shape of the focal spot. In addition, it is proposed that real XCT measurements are accompanied by computer simulations using a virtual XCT system with properties (including the characteristics of the focal spot) that closely resemble the properties of a given XCT system.

Based on the results of the study it is recommended that the measurement of the size and shape of the focal spot should be a part of X-ray tube qualification procedures for metrological XCT systems. Building on the findings from this study, future work should include the investigations of the influence of the focal spot size and shape on multi-material objects of complex geometries.

Novelty and contribution: this is a novel simulation study, which allows direct assessment of the effects of the focal spot size and shape on dimensional measurement in XCT. Evidence was acquired to support the proposition that the measurement of the focal spot size and shape needs to be included in the X-ray probe qualification procedure.

Chapter 6: Thesis conclusions and future research

The aim of this thesis was two-fold: to identify and evaluate the parameters associated with the X-ray tube, which influence the dimensional measurement in micro-focus cone-beam XCT systems; and to propose techniques which can contribute to the development of standardised procedures for X-ray tube qualification. In order to achieve this aim, a number of clear objectives were set. Following the overview of the background to the X-ray physics, XCT technology and the concepts and requirements of dimensional metrology, it became apparent that XCT is a complex measuring technique with numerous factors which can influence the measurement result. Given the fact that XCT is a fairly new technology in its application to metrology, many of these factors are still poorly understood. At present, there are no international or national standards for performance verification and calibration of XCT. In addition, no specific guidelines for the qualification of the X-ray tubes used in metrological XCT systems currently exist.

Based on the review of current standards for medical and non-destructive testing applications of XCT and additional metrology literature, a number of parameters associated with X-ray tubes which can potentially influence dimensional measurement were identified. Subsequently, the factors associated with the X-ray tube such as the positional stability of the focal spot, the off-focal radiation, the focal spot size and shape and their influence of dimensional measurement were examined using experimental and computer simulation techniques. Based on the research presented in the thesis, the following contributions to the field of metrological application of XCT have been made:

- This is the first study which attempted to identify the parameters associated with the X-ray tube which can influence dimensional measurement, in order to contribute to the development of standardised procedures for X-ray tube qualification and performance verification of XCT systems.
- This is the first study which brought the phenomenon of off-focal radiation in micro-focus cone-beam XCT systems to the attention of the scientific community in dimensional metrology.
- The experimental and computer simulation investigations conducted in this study showed that the positional stability of the focal spot, the off-focal radiation, the focal spot size and the focal spot shape are the parameters of the X-ray tube which can directly influence the measurement performance of a micro-focus cone-beam XCT system. Therefore, it is necessary to include these parameters as part of X-ray tube qualification and the performance verification procedures of XCT systems.

- Due to the complexity of XCT systems, the study highlighted the importance of combining the experimental and computer simulation methods for effective evaluation of the positional stability of the focal spot and the properties of the secondary source due to off-focal radiation and their influence on measurement. The techniques developed during the study can be readily employed as part of X-ray tube qualification and performance verification procedures of XCT systems.

Based on the investigations discussed in this thesis, the following suggestions for future research can be made:

- To investigate the influence of the positional stability of the focal spot, the focal spot size and shape and off-focal radiation on dimensional measurement of multi-material objects and objects with complex geometries by applying the techniques presented in this thesis.
- To investigate the stability of the focal spot size, shape and off-focal radiation throughout the scan duration and their influence on dimensional measurement using the techniques presented in this thesis.
- Another parameter associated with the X-ray tube and not discussed in this thesis, is the instability of the X-ray flux. It is therefore suggested to investigate the influence of the instability of the X-ray flux on dimensional measurement in micro-focus cone-beam XCT systems using the techniques developed during this study.
- Spatial resolution is the parameter that is often used in characterising the imaging performance of an X-ray system. Since spatial resolution is influenced by the X-ray tube settings, it is recommended that future research should include the investigations of how the positional stability of the focal spot, the presence of off-focal radiation, the focal spot size, the focal spot shape and the instability of the X-ray flux affect spatial resolution of the XCT system. This research can be carried out using the techniques developed during this study.
- The results of this study clearly established the fact that the positional stability of the focal spot, off-focal radiation and of the focal spot size and shape influence the dimensional measurement. These parameters, therefore, need to be included as input quantities in the measurement model in the uncertainty evaluation process. This requires further in-depth study of the parameters and their properties, as each parameter needs to be characterised by an appropriate probability distribution.
- One of the most important characteristics of an imaging system is its ability to reproduce faithfully the relative intensity distribution of the original object in the final

image. The parameter that is widely used to describe this aspect of imaging is the optical transfer function (OTF)²⁷. Therefore, it is recommended that future research should include the investigations of how the positional stability of the focal spot, the presence of off-focal radiation, the focal spot size, the focal spot shape and the instability of the X-ray flux influence the OTF.

Overall, it can be concluded that the results of the research presented in this thesis adequately fulfilled the thesis aim and objectives.

²⁷ The OTF is defined as a measure of how the contrast and phase of a sinewave grating pattern is reproduced by the imaging system [152]. The contrast component of the OTF is called the modulation transfer function (MTF) and the phase component is called the phase transfer function (PTF). For an in-depth treatment of the subject see [152].

Appendix A

The Canny edge detection algorithm, created by John F Canny in 1986, is a multi-stage edge detection process with the following steps [147], [148]:

1. Due to the fact that the process of edge detection is easily affected by noise, the first step in the Canny algorithm is to remove the noise from the original 2D image, $\mathbf{I}_{original}$ by convolving it with a 2D Gaussian kernel, $\mathbf{H}_{i,j}$.

$$\mathbf{I}_{smooth} = \mathbf{H}_{i,j} \otimes \mathbf{I}_{original} , \quad (101)$$

where \mathbf{I}_{smooth} is the smoothed image and \otimes represents convolution.

A 2D Gaussian function is defined as

$$H[i, j] = k e^{-\frac{i^2 + j^2}{2\sigma^2}} , \quad (102)$$

where k is the normalisation constant and σ is the standard deviation, numerical value of which determines the width of the Gaussian, and, hence, the degree of smoothing. Discrete approximations to this continuous function are specified using two parameters: 1) the size of the kernel, i.e. $N \times N$ filter mask and 2) the value for the standard deviation σ . For example, a Gaussian kernel of size 7×7 and $\sigma = \sqrt{2}$ is calculated to be

| $[i, j]$ | -3 | -2 | -1 | 0 | 1 | 2 | 3 |
|----------|--------|--------|--------|--------|--------|--------|--------|
| -3 | 0.0111 | 0.0388 | 0.0821 | 0.1054 | 0.0821 | 0.0388 | 0.0111 |
| -2 | 0.0388 | 0.1353 | 0.2865 | 0.3679 | 0.2865 | 0.1353 | 0.0388 |
| -1 | 0.0821 | 0.2865 | 0.6065 | 0.7788 | 0.6065 | 0.2865 | 0.0821 |
| 0 | 0.1054 | 0.3679 | 0.7788 | 1.0000 | 0.7788 | 0.3679 | 0.1054 |
| 1 | 0.0821 | 0.2865 | 0.6065 | 0.7788 | 0.6065 | 0.2865 | 0.0821 |
| 2 | 0.0388 | 0.1353 | 0.2865 | 0.3679 | 0.2865 | 0.1353 | 0.0388 |
| 3 | 0.0111 | 0.0388 | 0.0821 | 0.1054 | 0.0821 | 0.0388 | 0.0111 |

For computational purposes, the preferred weights of the kernel are integers. This can be achieved by using equation (98) and setting one of the corner values in the above matrix to, say, 1, then

$$\frac{H[-3, -3]}{k} = e^{-\frac{(-3)^2 + (-3)^2}{4}} = 0.0111, \quad (103)$$

Appendix A

and

$$\frac{1}{k} = 0.0111, \quad k = \frac{1}{0.0111} = 90.0901. \quad (104)$$

By multiplying the rest of the weights in the kernel by this k value and rounding them to the nearest integer, the following Gaussian kernel is produced:

| $[i, j]$ | -3 | -2 | -1 | 0 | 1 | 2 | 3 |
|----------|----|----|----|----|----|----|----|
| -3 | 1 | 4 | 7 | 10 | 7 | 4 | 1 |
| -2 | 4 | 12 | 26 | 33 | 26 | 12 | 4 |
| -1 | 7 | 26 | 55 | 71 | 55 | 26 | 7 |
| 0 | 10 | 33 | 71 | 91 | 71 | 33 | 10 |
| 1 | 7 | 26 | 55 | 71 | 55 | 26 | 7 |
| 2 | 4 | 12 | 26 | 33 | 26 | 12 | 4 |
| 3 | 1 | 4 | 7 | 10 | 7 | 4 | 1 |

To normalise the Gaussian kernel, each value in the above matrix is divided by the total sum of values in the matrix. Here,

$$\sum_{i=-3}^3 \sum_{j=-3}^3 H[i, j] = 1115, \quad (105)$$

hence, the output values for the smoothed image are

$$I_{smooth}[x, y] = \frac{1}{1115} \sum_{i=i_{start}}^{i=i_{end}} \sum_{j=j_{start}}^{j=j_{end}} H[i, j] I_{original}[x - i, y - j] \quad (106)$$

2. After minimising the noise in the image, the next step is to calculate the magnitude of the gradient in the image, referred to as the edge strength. To achieve this, the image I_{smooth} is convolved with the Sobel operator, comprising two kernels K_{Gx} and K_{Gy} . The convolution produces two matrices G_x and G_y , containing the horizontal and vertical derivative approximations, respectively, i.e.

$$\begin{aligned} G_x &= K_{Gx} \otimes I_{smooth} \\ G_y &= K_{Gy} \otimes I_{smooth}, \end{aligned} \quad (107)$$

where

$$\begin{aligned}\mathbf{K}_{Gx} &= \begin{bmatrix} -1 & 0 & 1 \\ -2 & 0 & 2 \\ -1 & 0 & 1 \end{bmatrix} \\ \mathbf{K}_{Gy} &= \begin{bmatrix} 1 & 2 & 1 \\ 0 & 0 & 0 \\ -1 & -2 & -1 \end{bmatrix}\end{aligned}\quad (108)$$

The edge strength can then be calculated using

$$|\mathbf{G}| = \sqrt{\mathbf{G}_x^2 + \mathbf{G}_y^2}, \quad (109)$$

which, for computational purposes, is approximated by

$$|\mathbf{G}| = |\mathbf{G}_x| + |\mathbf{G}_y|. \quad (110)$$

3. The next step is to calculate the edge direction using

$$\Theta = \tan^{-1}\left(\frac{|\mathbf{G}_x|}{|\mathbf{G}_y|}\right). \quad (111)$$

For example, to estimate the magnitude and direction of the gradient for pixel $[x, y]$ in figure 13, using the Sobel kernels \mathbf{K}_{Gx} and \mathbf{K}_{Gy} in equation (8), the following calculations are performed:

| | | |
|-----|----------|-----|
| 150 | 150 | 150 |
| 60 | $[x, y]$ | 140 |
| 40 | 40 | 50 |

Figure A.1 Schematic representation of numerical values of pixel $[x, y]$ with its neighbouring pixels in an image.

$$G_x[x, y] = (-1) \times 150 + (-2) \times 60 + (-1) \times 40 + 1 \times 150 + 2 \times 140 + 1 \times 50 = 170$$

$$G_y[x, y] = 1 \times 150 + 2 \times 150 + 1 \times 150 + (-1) \times 40 + (-2) \times 40 + (-1) \times 50 = 430,$$

resulting in the magnitude and direction of the gradient to be

$$G[x, y] = |170| + |430| = 600,$$

$$\theta[x, y] = \tan^{-1} \left(\frac{|G_y[x, y]|}{|G_x[x, y]|} \right) = \tan^{-1} \left(\frac{|430|}{|170|} \right) = 68.43^\circ.$$

4. The next step is to digitise the values of the edge direction. In other words, in a digital image, the direction of an edge through each pixel can take only one of the four possible values: 0° , 45° , 90° and 135° ; therefore, all calculated values of θ are approximated by the four values they are the closest to. The above value of the edge direction of 68.43° is then set to 90° .
5. The next step is known as the non-maximum suppression. Here, the pixel values of each pixel are compared to the neighbourhood pixels along the direction of the edge: pixels with the maximum value are considered to be preliminary edge pixels and all other pixel values are suppressed, i.e. set to zero.

The final step is known as hysteresis. During this step the remaining preliminary edge pixels are converted into ‘real edge’ pixels using two threshold values: $T1$ and $T2$, where $T1 > T2$. Pixels with values higher than $T1$ are marked as ‘strong’; pixels with values between $T1$ and $T2$ are marked as ‘weak’; and pixels with values below $T2$ are set to zero. The ‘strong’ pixels are identified as true edges, then the ‘weak’ pixels are added to true edges if, and only if, they are connected to the ‘strong’ pixels, otherwise their values are set to zero.

List of References

- [1] Bushberg J T, Seibert J A, Leidholdt E M Jr and Boone J M 2012 *The essential physics of medical imaging* (Lippincott Williams & Wilkins)
- [2] Kalender W 2011 *Computed tomography: fundamentals, system technology, image quality, applications* (Erlangen)
- [3] Kruth J P, Bartscher M, Carmignato S, Schmitt R, De Chiffre L and Weckenmann A 2011 Computed tomography for dimensional metrology *Ann. CIRP* **60/2** 821–842
- [4] Carmignato S 2012 Accuracy of industrial computed tomography measurements: experimental results from an international comparison *Ann. CIRP* **61/1** 1–4
- [5] Sun W, Brown S B and Leach R K 2012 An overview of industrial X-ray computed tomography *NPL Report* **ENG32**
- [6] Flack D and Hannaford J 2005 *A national measurement good practice guide: Fundamental good practice in dimensional metrology* Measurement Good Practice Guide No 80. (NPL)
- [7] Bell S 2001 *A beginner's guide to uncertainty in measurement* Measurement Good Practice Guide No. 11 Issue 2 (NPL)
- [8] JCGM 200:2012 International vocabulary of metrology – Basic and general concepts and associated terms (VIM) (JCGM)
- [9] Leach R K 2009 *Fundamental principles of engineering nanometrology* (Elsevier Inc.)
- [10] The International System of Units (SI) 2006 (Bureau International des Poids et Mesures)
- [11] Resolutions of the CGPM: 17th meeting 1983 Bureau International des Poids et Mesures Website: www.bipm.org/en/CGPM/db/17/1 Accessed on 14 February 2014
- [12] Birch K 2001 *Estimating uncertainties in testing* Measurement Good Practice Guide No. 36 (BMTA)
- [13] ISO/IEC 17025 2005 General requirements for the competence of testing and calibration laboratories (International Organization for Standardization)
- [14] JCGM 100: 2008 Evaluation of measurement data - Guide to the expression of uncertainty in measurement (JCGM)
- [15] Cox M G and Harris P M 2010 Software support for metrology. Best practice guide No. 6 *NPL Report* **MS6**
- [16] JCGM 101: 2008 Evaluation of measurement data - Supplement 1 to the Guide to the expression of uncertainty in measurement - Propagation of distributions using a Monte Carlo method (JCGM)
- [17] ISO 10360-1:2001 Geometrical product specifications (GPS) - Acceptance and reverification tests for coordinate measuring machines (CMM) - Part 1: Vocabulary (International Organization for Standardization)
- [18] Bosch J 1995 *Coordinate measuring machines and systems* (Taylor & Francis)

Bibliography

- [19] The International Organization for Standardization
Website: <http://www.iso.org/iso/home/standards.htm> Accessed on 12 January 2016
- [20] Flack D 2011 *CMM verification* Measurement Good Practice Guide No. 42 Issue 2 (NPL)
- [21] PD 6461-4:2004 General metrology - Part 4: Practical guide to measurement uncertainty (BSi)
- [22] Schwenke H, Knapp W, Haitjema H, Weckenmann A, Schmitt R and Delbressine F 2008 Geometric error measurement and compensation of machines - An update *Ann. CIRP* **57/2**
- [23] Franke M, Bundesanstalt P and Britain G 2005 Error mapping of CMMs and machine tools by a single tracking interferometer *Ann. CIRP* **54** 2–5
- [24] ISO 10360-2 2009 Geometrical Product Specifications (GPS) - Acceptance and reverification tests for coordinate measuring machines (CMM) (International Organization for Standardization)
- [25] ISO 3650:1999 Geometrical Product Specifications (GPS) - Length standards - Gauge blocks (International Organization for Standardization)
- [26] ISO/TS 23165:2006 Geometrical product specifications (GPS) - Guidelines for the evaluation of coordinate measuring machine (CMM) test uncertainty (International Organization for Standardization)
- [27] ISO 14253-1:2011 Geometrical product specifications (GPS) - Inspection by measurement of workpieces and measuring equipment - Part 1: Decision rules for proving conformity or nonconformity with specifications (International Organization for Standardization)
- [28] ISO 15530-3:2011 Geometrical product specifications (GPS) - Coordinate measuring machines (CMM): Technique for determining the uncertainty of measurement - Part 3: Use of calibrated workpieces or measurement standards (International Organization for Standardization)
- [29] ISO/TS 15530-1:2013 Geometrical product specifications (GPS) - Coordinate measuring machines (CMM): Technique for determining the uncertainty of measurement (International Organization for Standardization)
- [30] ISO 14253-2:2011 Geometrical product specifications (GPS) - Inspection by measurement of workpieces and measuring equipment Part 2: Guidance for the estimation of uncertainty in GPS measurement in calibration of measuring equipment (International Organization for Standardization)
- [31] Flack D 2014 *CMM probing* Measurement Good Practice Guide No. 43 Issue 2 (NPL)
- [32] ISO 15530-4:2008 Geometrical Product Specifications (GPS) - Coordinate measuring machines (CMM): Technique for determining the uncertainty of measurement (International Organization for Standardization)
- [33] Christoph R and Neumann H J 2011 *X-ray tomography in industrial metrology* (Suddeutscher verlag onpact GmbH)
- [34] ISO 15708-1:2002 Non-destructive testing - Radiation methods - Computed tomography - Part 1: Principles (International Organization for Standardization)

- [35] ISO 15708-2:2002 Non-destructive testing - Radiation methods - Computed tomography - Part 2: Examination practices (International Organization for Standardization)
- [36] E1441 2000 Standard guide for computed tomography (CT) imaging (ASTM International)
- [37] E1570 2011 Standard practice for computed tomography (CT) examination (ASTM International)
- [38] E1672 2012 Standard guide for computed tomography (CT) system selection (ASTM International)
- [39] BS EN 16016-1:2011 Non destructive testing - Radiation methods - Computed tomography Part 1: Terminology (BSi)
- [40] BS EN 16016-2:2011 Non destructive testing - Radiation methods - Computed tomography Part 2: Principle, equipment and samples (BSi)
- [41] BS EN 16016-3:2011 Non destructive testing - Radiation methods - Computed Tomography Part 3: Operation and interpretation (BSi)
- [42] BS EN 16016-4:2011 Non destructive testing - Radiation methods - Computed tomography Part 4: Qualification (BSi)
- [43] BS EN 60601-2-44:2009 and A11:2011 Medical electrical equipment - Part 2-44: Particular requirements for basic safety and essential performance of X-ray equipment for computed tomography (BSi)
- [44] BS EN 61223-2-6:1995 Evaluation and routine testing in medical imaging departments - Part 2: Constancy test (BSi)
- [45] BS EN 61223-3-5:2004 Evaluation and routine testing in medical imaging departments - Part 3-5: Acceptance tests - Imaging performance of computed tomography X-ray equipment (BSi)
- [46] BS EN 60336:2005 Medical electrical equipment - X-ray tube assemblies for medical diagnosis - Characteristics of focal spots (BSi)
- [47] BS EN 60601-2-28:2010 Medical electrical equipment - Part 2-28: Particular requirements for the basic safety and essential performance of X-ray tube assemblies for medical diagnosis (BSi)
- [48] BS EN 12543-1:1999 Non-destructive testing - Characteristics of focal spots in industrial X-ray systems for use in non-destructive testing (BSi)
- [49] BS EN 12543-2:1999 Non-destructive testing - Characteristic of focal spots in industrial X-ray systems for use in non-destructive testing - Part 2: Pinhole camera radiographic (BSi)
- [50] BS EN 12543-3:1999 Non-destructive testing - Characteristics of focal spots in industrial X-ray systems for use in non-destructive testing - Part 3: Slit camera radiographic method (BSi)
- [51] BS EN 12543-4:1999 Non-destructive testing - Characteristics of focal spots in industrial X-ray systems for use in non-destructive testing - Part 1: Scanning method (BSi)

Bibliography

- [52] BS EN 12543-5:1999 Non-destructive testing - Characteristics of focal spots in industrial X-ray systems for use in non-destructive testing - Part 5: Measurement of the effective focal spot size of mini and micro focus (BSi)
- [53] BS EN 12544-1:1999 Non-destructive testing - Measurement and evaluation of the X-ray tube voltage - Part 1: Voltage divider method (BSi)
- [54] BS EN 12544-2:2000 Non-destructive testing. Measurement and evaluation of the X-ray tube voltage - Part 2: Constancy check by the thick filter method (BSi)
- [55] BS EN 12544-3:1999 Non-destructive testing - Measurement and evaluation of the X-ray tube voltage - Part 3: Spectrometric method (BSi)
- [56] VDI/VDE 2630 Part 1.3 2011 Computed tomography in dimensional measurement - Guidelines for the application of DIN EN ISO 10360 for coordinate measuring machines with CT-sensors (GMA, Duesseldorf)
- [57] ISO/TC 213 2012 Geometrical product Specifications (GPS) - Acceptance and reverification tests for coordinate measuring machines (CMM) - Part CT: CT (International Organization for Standardization)
- [58] VDI/VDE 2630 Part 1.1 2009 Computed tomography in dimensional measurement - Fundamentals and definitions (GMA, Duesseldorf)
- [59] VDI/VDE 2630 Part 1.2 2010 Computed tomography in dimensional measurement - Influencing variables on measurement results and recommendations for computed tomography dimensional measurements (GMA, Duesseldorf)
- [60] VDI/VDE 2630 Part 1.4 2008 Computed tomography in dimensional metrology - Measurement procedure and comparability (GMA, Dusseldorf)
- [61] Kruth J P, Bartscher M, Carmignato S, Schmitt R, De Chiffre and Weckenmann A 2005 Computed tomography for dimensional metrology *Ann. CIRP* **60** 1–24
- [62] Hiller J, Maisl M and Reindl L M 2012 Physical characterization and performance evaluation of an X-ray micro-computed tomography system for dimensional metrology applications *Meas. Sci. Technol.* **23** 085404
- [63] Samei E, Flynn M J and Reimann D 1998 A method for measuring the presampled MTF of digital radiographic systems using an edge test device *Med. Phys.* **25/1** 102–113
- [64] Müller P 2010 Use of reference objects for correction of measuring errors in X-ray computed tomography *PhD thesis* (DTU Mechanical Engineering)
- [65] Lettenbauer H, Georgi B and Weiß D 2007 Means to verify the accuracy of CT systems for metrology applications *NDT.net* **12/10**
- [66] Stolfi A and De Chiffre L 2016 3D artefact for concurrent scale calibration in Computed Tomography *Ann. CIRP* **65/1** 499–502
- [67] Neuschaefer-Rube U, Neugebauer M, Ehrig W, Bartscher M and Hilpert U 2008 Tactile and optical microsensors: test procedures and standards *Meas.Sci. Technol.* **19** 084010
- [68] Bartscher M, Hilpert U, Goebbels J and Weidemann G 2007 Enhancement and proof of accuracy of industrial computed tomography (CT) measurements *Ann. CRIP* **56/1** 495-498

- [69] Ehrig K, Staude A, Goebbels J, Bartscher M, Koch M and Neukamm M 2011 Evaluierung von Testkörpern zur Strahlaufhärtungskorrektur beim dimensionellen Messen mit Computertomographie *NDT.net* **16/6**
- [70] Heinzl C, Kastner K, Georgi B and Lettenbauer H 2007 Comparison of surface detection methods to evaluate cone beam computed tomography data for three dimensional metrology *NTD.net* **12/10**
- [71] Kiekens K, Welkenhuyzen F, Tan Y, Bleys P, Voet A, Kruth J P and Dewulf W 2011 A test object with parallel grooves for calibration and accuracy assessment of industrial computed tomography (CT) metrology *Meas. Sci. Technol.* **22/11** 115502
- [72] Bartscher M, Neukamm M, Koch M, Neuschaefer-rube U, Kuhn C, Deffner A, Zeiss C, Messtechnik I, Knoch A and Saxony F 2010 Performance assessment of geometry measurements with micro-CT using a dismountable work-piece-near reference standard *NDT.net* **15/10**
- [73] Hermanek P and Carmignato S 2016 Case Studies in Nondestructive Testing and Evaluation Reference object for evaluating the accuracy of porosity measurements by X-ray computed tomography *Case Stud. Nondestruct. Test. Eval.* **1** 1–6
- [74] JIMA Micro resolution chart for X-ray Website:
http://www.jima.jp/content/pdf/rt_ct-02cata02.pdf. Accessed on 11 August 2015
- [75] Staude A and Goebbels J 2011 Determining the spatial resolution in computed tomography – comparison of MTF and line-pair structures *NDT.net* **16/11**
- [76] Carmignato S, Pierobon A, Rampazzo P, Parisatto M and Savio E 2012 CT for Industrial Metrology – Accuracy and Structural Resolution of CT Dimensional Measurements *NDT.net* **17/12**
- [77] Hsieh J 2009 *Computed tomography: principles, design, artifacts and recent advances* (SPIE Press)
- [78] Hiller J and Reindl L M 2012 A computer simulation platform for the estimation of measurement uncertainties in dimensional X-ray computed tomography *Measurement* **45/8** 2166–2182
- [79] Hiller J and Hornberger P 2016 Measurement accuracy in X-ray computed tomography metrology: Toward a systematic analysis of interference effects in tomographic imaging *Precis. Eng.* **45** 18–32
- [80] Ferrucci M, Ametova E, Carmignato S and Dewulf W 2016 Evaluating the effects of detector angular misalignments on simulated computed tomography data *Precis. Eng.* **45** 230–241
- [81] Xue L, Suzuki H, Ohtake Y, Fujimoto H, Abe M, Sato O and Takatsuji T 2015 A method for improving measurement accuracy of cylinders in dimensional CT metrology *Comput. Des. J.* **69** 25–34
- [82] Xue L, Suzuki H, Ohtake Y, Fujimoto H, Abe M, Sato O and Takatsuji T 2015 Numerical analysis of the Feldkamp–Davis–Kress effect on industrial X-ray computed tomography for dimensional metrology *J. Comput. Inf. Sci. Eng.* **15/2** 021008
- [83] Lifton J, Malcolm A A and McBride J W 2015 On the uncertainty of surface determination in x-ray computed tomography for dimensional metrology *Meas.Sci. Technol.* **26** 035003

Bibliography

- [84] Angel J, De Chiffre L, Kruth J P, Tan Y and Dewulf W 2015 Performance evaluation of CT measurements made on step gauges using statistical methodologies *J. Manuf. Sci. Technol.* **11** 68–72
- [85] Cierniak R 2011 *X-Ray computed tomography in biomedical engineering* (Springer)
- [86] Manahan S E 2009 *Fundamentals of sustainable chemical science* (CRC Press)
- [87] Inspect-X 3.1, X-Tek X-ray and CT inspection manual (Nikon Metrology)
- [88] X-ray tube - schematic representation (Nikon Metrology) Website: <http://blog.nikonmetrology.com/blog/high-voltage-microfocus-ct-inspection-dense-complex-parts/> Accessed on 17 March 2015
- [89] Behling R 2015 *Modern diagnostic X-ray sources: technology, manufacturing, reliability* (CRC Press)
- [90] Williams D B and Carter C B 2009 *Transmission electron microscopy* (Springer)
- [91] Curry T S, Dowdey J E and Murr R E 1990 *Christensen's physics of diagnostic radiology* (Lea & Febiger, US)
- [92] Buzug T M 2010 *Computed tomography: from photon statistics to modern cone-beam CT* (Springer)
- [93] Egerton R 2005 *Physical principles of electron microscopy. An introduction to TEM, SEM, and AEM* (Springer)
- [94] Thomas J and Gemming T 2014 *Analytical transmission electron microscopy* (Springer Netherlands)
- [95] Bozzola J J 1998 *Electron microscopy: principles and techniques for biologists* (Jones & Bartlett)
- [96] Beaman D R and Isasi J A 1972 *Electron beam microanalysis* (ASTM International)
- [97] Potts P J 1987 *A handbook of silicate rock analysis* (Blackie)
- [98] Kanaya K and Okayama S 1972 Penetration and energy-loss theory of electrons in solid targets *J. Phys. D: Appl. Phys.* **5/1** 43–58
- [99] Love G and Scott V 1978 Evaluation of a new correction procedure for quantitative electron probe microanalysis *J. Phys. D: Appl. Phys.* **11**
- [100] Reimer L 1998 *Scanning electron microscopy: physics of image formation and microanalysis* (Springer)
- [101] Goldstein J et al 2003 *Scanning electron microscopy and X-ray microanalysis* (Plenum)
- [102] Turner N H 2006 Encyclopedia of analytical chemistry. X-Ray photoelectron and Auger electron spectroscopy (John Wiley & Sons Ltd)
- [103] Brahme A and Budinger T F 2014 *Comprehensive biomedical physics. Volume 1* (Elsevier B.V.)
- [104] Khan F M and Gibbons J P 2014 *The physics of radiation therapy* (Lippincott Williams and Wilkins)
- [105] Mayles P, Nahum A and Rosenwald J 2007 *Handbook of Radiotherapy Physics: Theory and Practice* (CRC Press)

- [106] Castaing R 1951 Application des Sondes Électroniques à une Méthode d'Analyse Ponctuelle Chimique et Cristallographique *PhD Thesis* (Univ. Paris)
- [107] X-Ray mass attenuation coefficients (National Institute of Standards and Technology) Website:
<http://physics.nist.gov/PhysRefData/XrayMassCoef/tab3.html> Accessed on 2 May 2016
- [108] Van Metter R L, Beutel J and Kundel H L 2000 *Handbook of medical imaging. Volume 1: Physics and psychophysics* (SPIE Press)
- [109] Dowsett D, Kenny P A and Johnston R E 2006 *The physics of diagnostic imaging* (CRC Press)
- [110] Kak A C and Slaney M 2001 *Principles of computerized tomographic imaging* (SIAM, Philadelphia)
- [111] Boone M N, Vlassenbroeck J, Peetermans S, Van Loo D, M. Dierick M Van Hoorebeke L 2012 Secondary radiation in transmission-type X-ray tubes: simulation, practical issues and solution in the context of X-ray microtomography *Nucl. Instruments Methods Phys. Res. A* **661** 7–12
- [112] Gupta A K, Chowdhury V and Khandelwal N 2013 *Diagnostic radiology: recent advances and applied physics in imaging* (JP Medical Ltd)
- [113] Leblans P 2002 New needle-crystalline detector for X-ray computed radiography *NDT.net* **7/12**
- [114] Papp J 2014 *Quality Management in the Imaging Sciences* (Elsevier Health Sciences)
- [115] Imaging components (PerkinElmer) Website:
<http://www.perkinelmer.co.uk/imaging-components/detectors/xrd-a-si/> Accessed on 14 February 2016
- [116] Shaw C C 2014 *Cone beam computed tomography* (Taylor & Francis)
- [117] Feldkamp L A, Davis L C and Kress J W 1984 Practical cone-beam algorithm *J. Opt. Soc. Am.* **1/6** 612–619
- [118] Zeng G 2010 *Medical image reconstruction: a conceptual tutorial* (Springer)
- [119] Seibert J A and Boone J M 2005 X-ray imaging physics for nuclear medicine technologists. Part 2: X-ray interactions and image formation *J. Nucl. Med. Technol.* **33/1** 3–18
- [120] Zhu L, Bennett N R and Fahrig R 2006 Scatter correction method for X-ray CT using primary modulation: theory and preliminary results *IEEE Trans. Med. Imaging* **25/12** 1573–1587
- [121] Peterzol A, Létang J M and Babot D 2008 A beam stop based correction procedure for high spatial frequency scatter in industrial cone-beam X-ray CT *Nucl. Instr. Meth. in Phys. Res. B* **266** 4042–4054
- [122] Schörner K, Goldammer M, Stephan J, Thompson D O and Chimenti D E 2011 Experimental scatter correction methods in industrial X-ray cone-beam CT *AIP Conf. Proc.* **1335** 485–492
- [123] Schulze R, Heil U, Groß D, Bruellmann D D, Dranischnikow E, Schwanecke U and Schoemer E 2011 Artefacts in CBCT: A review *Dentomaxillofacial Radiol.* **40/5** 265–273

Bibliography

- [124] Kasperl S, Hiller J and Krumm M 2008 Computed tomography metrology in industrial research & development *NDT.net* **14/9**
- [125] Ferrucci M, Leach R K, Giusca C L, Dewulf W and Carmignato S 2015 Towards geometrical calibration of X-ray computed tomography systems - A review *Meas. Sci. Technol.* **26** 92003
- [126] Carmignato S, Dreossi D, Mancini L, Marinello F, Tromba G and Savio E 2009 Testing of X-ray microtomography systems using a traceable geometrical standard *Meas. Sci. Technol.* **20** 084021
- [127] Vogeler F, Verheecke W, Voet A and Kruth J 2011 Positional stability of 2D X-ray images for computer tomography *NDT.net* **16/11**
- [128] Reisinger S, Schmitt M and Volland V 2012 Geometric adjustment methods to improve reconstruction quality on rotational cone-beam systems *NDT.net* **17/12**
- [129] Fröba R and Steffen J P 2011 Assessing the effect of focal spot movement on the accuracy of CT results by using a simulation technique *NDT.net* **16/11**
- [130] Steffen J P and Fröba R 2011 Reducing the focal spot shift of microfocus X-ray tubes to increase the accuracy of CT-based dimensional measurement *NDT.net* **16/11**
- [131] Weiss D, Deffner A and Kuhn C 2011 Einfluß der Quellbewegung auf Reproduzierbarkeit und Antastabweichung im Röntgen-Computertomographen *NDT.net* **18/6**
- [132] Uhlman N, Salamon M and Burtzlauff S 2009 Components and methods for highest resolution computed tomography *NDT.net* **14/9**
- [133] Fröba T and Steffen J P 2011 The advancement of microfocus reflection tubes for industrial applications in measurement technology *50th Annual Conf. of the British Institute of Non-Destructive Testing (Telford, UK)*
- [134] Steel: thermal expansion coefficient (Engineering toolbox) Website:
http://www.engineeringtoolbox.com/linear-expansion-coefficients-d_95.html
Accessed on 22 January 2016
- [135] Borosilicate glass (Goodfellow: Ceramic and Glass Division) Website:
<http://www.goodfellow-ceramics.com/products/glasses/borosilicate-glass/>
Accessed on 22 January 2016
- [136] Nixon M 2012 *Feature extraction & image processing for computer vision* (Academic Press)
- [137] Forbes A B 1989 Robust circle and sphere fitting by least squares *NPL Report DITC140*
- [138] Ali E S M and Rogers D W O 2008 Quantifying the effect of off-focal radiation on the output of kilovoltage x-ray systems *Med. Phys.* **35** 4149
- [139] Katz L and Penfold A S 1952 Range-energy relations for electrons and the determination of beta-ray end-point energies by absorption *Rev. Mod. Phys.* **24**
- [140] E2903 2013 Standard test method for measurement of the effective focal spot size of mini and micro focus X-ray tubes (ASTM International)
- [141] Salamon M, Hanke R, Krüger P, Sukowski F, Uhlmann N and Volland V 2008 Comparison of different methods for determining the size of a focal spot of microfocus X-ray tubes *Nucl. Instr. Meth. in Phys. Res. A* **591** 54–58

- [142] De Chiffre L, Carmignato S, Kruth J, Schmitt R and Weckenmann A 2014 Industrial applications of computed tomography *Ann. CIRP* **63** 655–677
- [143] Sterpin E, Chen Y, Lu W, Mackie T R, Olivera G H and Vynckier S 2011 On the relationships between electron spot size, focal spot size, and virtual source position in Monte Carlo simulations *Med. Phys.* **38/3** 1579–1586
- [144] Dong X, Niu T, Jia X and Zhu L 2012 Relationship between x-ray illumination field size and flat field intensity and its impacts on x-ray imaging *Med. Phys.* **39/10** 5901–5909
- [145] Rueckel J, Stockmar M, Pfeiffer F and Herzen J 2014 Spatial resolution characterization of a X-ray microCT system *Appl. Radiat. Isot.* **94** 230–234
- [146] Arabi H, Kamali Asl A R and Aghamiri S M 2010 The effect of focal spot size on the spatial resolution of variable resolution X-ray CT scanner *Iran. J. Radiat. Res.* **8** 37–43
- [147] Solomon C and Breckon T 2010 *Fundamentals of digital image processing: a practical approach with examples in Matlab* (Wiley-Blackwell)
- [148] Najarian K and Splinter R 2012 *Biomedical signal and image processing* (CRC Press)
- [149] Francis A 1979 *Advanced level statistics* (Stanley Thornes Ltd)
- [150] Poludniowski G, Landry G, DeBlois F, Evans P M and Verhaegen F 2009 SpekCalc: a program to calculate photon spectra from tungsten anode x-ray tubes *Phys. Med. Biol.* **54/19**
- [151] Beister M, Kolditz D and Kalender W 2012 Iterative reconstruction methods in X-ray CT *Phys. Med.* **28/2** 94–108
- [152] Williams T 1999 *The optical transfer function of imaging systems* (IOP Publishing Ltd)